MEANDROS
MEDICAL AND DENTAL JOURNAL

ADNAN MENDERES UNIVERSITY
1992

MEANDROS
MEDICAL AND DENTAL JOURNAL

EDITORAL BOARD

MEANDROS
MEDICAL AND DENTAL JOURNAL

CONTENT

Research Article

THIOSTREPTON MODULATES *TLR4* EXPRESSION AND INDUCES APOPTOSIS IN MDA-MB-231 CELLS: AN *IN VITRO* AND *IN SILICO* ANALYSIS

Funda DEMİRTAŞ KORKMAZ [1*], Zekeriya DÜZGÜN [1], Asuman DEVECİ ÖZKAN [2]

[1]Department of Medical Biology, Faculty of Medicine, Giresun University, Giresun, TURKIYE
[2]Department of Medical Biology, Faculty of Medicine, Sakarya University, Sakarya, TURKIYE
Correspondence: fundakorkmz@gmail.com

ABSTRACT

Objective: Toll-like receptors (TLRs) are key pattern recognition receptors involved in tumorigenesis, apoptosis, and metastasis. Triple-negative breast cancer (TNBC) is a highly aggressive malignancy, associated with an unfavorable prognosis. Although the role of TLRs in breast cancer remains underexplored, recent studies suggest targeting TLRs in TNBC could be beneficial. In this study Thiostrepton, an antibiotic and novel inhibitor of *TLR7-9* in psoriatic inflammation, was investigated for its effects on *TLR3, TLR4*, and *TLR9* expression in TNBC cells (MDA-MB-231).

Materials and Methods: The cytotoxicity of thiostrepton was assessed using the MTT assay. RT-PCR was used to measure gene expression levels of *TLR3, TLR4, TLR9, Bax, Bcl-2, Nf-κB*, and *E-cadherin*. Cell morphology changes were analyzed with Acridine Orange/Ethidium Bromide (AO/EtBr) staining. Molecular docking and dynamics simulations examined interactions between thiostrepton and the TLR4-MD-2 complex.

Results: Thiostrepton led to a concentration- and time-dependent decrease in cell viability. It significantly inhibited *TLR4, Bcl-2* gene expression and increased *TLR3, Bax*, and *Nf-κB* levels. The changes in *Bax* and *Bcl-2* gene expression, along with alterations in cell morphology, demonstrated that thiostrepton promoted apoptosis in MDA-MB-231 cells. While *TLR9* expression reduction was not significant, thiostrepton notably increased *TLR3* expression and decreased *TLR4* expression. The three independent molecular dynamics simulations demonstrated that thiostrepton binds stably to the *TLR4-MD2* domain, exhibiting a high binding affinity as indicated by the binding free energy calculations.

Conclusion: Thiostrepton effectively induces apoptosis and reduces cell viability in TNBC cells. *In silico* analysis suggest thiostrepton could modulate *TLR4*, highlighting its potential as a candidate for further research and therapeutic development.

Keywords: Thiostrepton, toll like receptors, TLR4 receptor, triple-negative breast cancer

INTRODUCTION

Triple-negative breast cancer (TNBC) is a subtype of breast cancer distinguished by the absence of hormone receptors and HER2 expression, which makes it particularly challenging to treat with conventional hormone therapies and HER2-targeted treatments (1). These characteristics contribute to the poor prognosis and difficulty in treating TNBC. Therefore, identifying new targets and therapeutic strategies for TNBC is of paramount importance.

Toll-like receptors (TLRs) are key players in the innate immune system, serving a pivotal function in protecting the body from infections. However, recent research has revealed that TLRs not only manage immune responses but also participate in tumor development, apoptosis, and metastasis (2–4). The role of these receptors, particularly in relation to aggressive breast cancer subtypes such as TNBC, is garnering increasing scientific attention (5,6). It was found that *TLR3* expression is lower in triple-negative breast cancer (TNBC) tissue compared to adjacent normal tissue, and higher *TLR3* expression in TNBC was associated with better prognosis (7). Shi et al. (2020) showed that the expression levels of *TLR4* and *TLR7* significantly affected survival outcomes, with elevated levels correlating with poorer prognosis in breast cancer patients (6). It has been reported that low *TLR9* expression decreases survival in patients with TNBC (8). These findings highlight the complex role of TLRs in breast cancer, suggesting that their expression levels can influence prognosis in different subtypes of the disease. The variation in TLR expression, such as lower *TLR3* and *TLR9* and higher *TLR4* and *TLR7* levels, underscores the need for further research to understand their mechanisms and potential as therapeutic targets.

Molecular docking and Molecular Dynamics (MD) simulations have become indispensable tools in drug discovery and development, offering valuable insights into the interactions between small molecules and their target proteins (9). Molecular docking allows for the prediction of binding modes and affinities of ligands to their receptors, while MD simulations provide a dynamic view of these interactions over time, accounting for the flexibility of both the ligand and the target (10). These computational methods have been successfully employed in various cancer research studies, including those focused on breast cancer, to identify potential drug candidates and elucidate their mechanisms of action (11,12). By combining in silico approaches with experimental data, researchers can accelerate the drug discovery process and gain a deeper understanding of the molecular basis of drug efficacy (13). In the context of TLR-targeted therapies, these computational techniques can offer valuable predictions about the binding of new compounds to TLRs, guiding further experimental investigations and potentially uncovering novel therapeutic strategies.

Thiostrepton, a thiazole antibiotic isolated from *Streptomyces azureus*, is utilized in veterinary medicine but has no clinical applications (14). Recent studies have identified thiostrepton as an inhibitor of the oncogenic transcription factor *FoxM1*, and there is also evidence suggesting that it inhibits *TLR7-9* in psoriatic inflammation (15,16). Several studies have elucidated the antiproliferative, antimetastatic, and

apoptotic effects of thiostrepton in various types of cancer cells (17–19). However, the effects of thiostrepton on TLR expression and its role in challenging cancer types like TNBC are not yet fully understood. This study aims to evaluate the potential of thiostrepton as a therapeutic agent for TNBC by examining its effects on TLRs in TNBC cells. The study combines laboratory experiments (*in vitro*) and computer simulations (*in silico*) to contribute to the identification of novel therapeutic targets and enhance the understanding of thiostrepton's anti-tumor mechanisms.

MATERIALS AND METHODS

Cell culture and treatment process

MDA-MB-231 cell line, representing triple-negative breast cancer, was utilized and sourced from ATCC (USA). Cells were grown in RPMI 1640 medium (Thermo Fisher Scientific, USA), with the addition of 10% fetal bovine serum (FBS, sourced from the US), and supplemented with 100 units/mL penicillin and 100 μg/mL streptomycin (Gibco, Thermo Fisher Scientific, USA). The cultures were kept at 37°C in a humidified incubator with 5% CO2 to promote optimal cell growth and viability. Thiostrepton, procured from Enzo Life Sciences, was dissolved in DMSO to prepare a 10 mM stock solution. DMSO (dimethyl sulfoxide) was sourced from Sigma-Aldrich (St. Louis, MO, USA).

MTT assay

To assess cell viability, cells were seeded into 96-well plates and incubated for 24 hours. After this initial incubation, the cells were treated with thiostrepton concentrations and incubated for an additional 24 or 48 hours. Following the treatment period, MTT solution (5 mg/mL) was added to each well of the plate. Subsequently, the cells were incubated with the MTT reagent for 3 to 4 hours. Following this, the medium was carefully aspirated, and each well received 100 μL of DMSO as a solvent and then plates were placed on an orbital shaker for 3-5 minutes to ensure thorough dissolution. The absorbance of the solution was measured using a spectrophotometer at a wavelength of 540 nm. The viability of the control cells (those not treated with thiostrepton) was defined as 100%, and the viability of the treated cells was calculated as a percentage relative to this control.

Real-time PCR analysis

Total RNA isolation was performed using TRIzol reagent (Invitrogen) with modifications to the method outlined by Chomczynski et al. (20). The Nanodrop spectrophotometer (Thermo Fisher Scientific, Waltham, MA, USA) was used to evaluate the purity and concentration of the isolated RNA. Complementary DNA (cDNA) was subsequently synthesized using the cDNA Reverse Transcription Kit (Thermo Fisher Scientific, Waltham, MA, USA). Real-time PCR amplification was carried out on a

LightCycler instrument (Bio-Rad) with HOT FIREPol EvaGreen qPCR Mix Plus (no ROX) (Solis BioDyne, Inc.) Primers for TLR3, TLR4, TLR9, Bax, Bcl2, Nfkb, E cadherin genes were designed using Oligo7 software. GAPDH was utilized as the endogenous reference gene. Each experiment was conducted in triplicate. Gene expression levels were normalized to GAPDH (ΔCt values), and $2^{-\Delta\Delta Ct}$ method was employed to determine the fold changes in mRNA expression.

Acridine orange/ethidium bromide (AO/EB) staining

AO/EB staining was conducted to assess cell morphology after thiostrepton treatment. Cells (5×10^5) were grown in six-well plates and subsequently exposed to 4μM thiostrepton. After 24 hours of incubation, the cell suspension were mixed with AO/EB solution, then cells were dropped on to the microscope slide. Finally, the slides were examined under a fluorescence microscopy (NIKON Eclipse Ni series, Nikon Instruments Inc., USA) at 20x magnification.

Molecular docking

The crystal structure of human TLR4 protein was obtained from the RCSB Protein Data Bank with the PDB code 3FXI (21)(rcsb.org). The thiostrepton compound was obtained from the PubChem database (PubChem CID: 16154490) (22). Molecular docking calculations were analyzed with AutoDock Vina 1.1.2 (23). The calculations were automated using the PyRx software (24). For the docking process, a 17 Å cubic grid box was used, targeting the MD2 triglyceride binding pocket. The resulting protein-compound complex from the docking process was used as the initial structure for molecular dynamics simulations.

Molecular dynamics simulation and free energy calculation

The complex obtained from molecular docking underwent minimization and equilibration phases before being subjected to a 100 ns production run. The process was repeated three times. All simulations were conducted using GROMACS 2020 software (25). The leap-frog integration algorithm was employed in all simulations with 2 fs time step. The AMBER99SB-ILDN force field was used with the TIP3P water model (26). Periodic boundary conditions were applied, and the Particle Mesh Ewald algorithm was employed to handle long-range electrostatics (27).

For the minimization phase, 50,000 steps of the steepest descent algorithm were used with a 10 kJ/mol cutoff . The equilibration phase was conducted in two stages: NVT and NPT ensembles. In the NVT stage, the LINCS algorithm was used as the constraint algorithm, with hydrogen bonds constrained (28). The Verlet cut-off scheme was employed. The Berendsen thermostat was used for temperature coupling, and the simulation length was set to 300 ps (29). In the NPT stage, the V-rescale algorithm was used for temperature coupling, and the Isotropic Berendsen algorithm for pressure coupling (29). The simulation length was set to 1 ns, with the LINCS algorithm applied as in the NVT stage (28).

For the production phase, the V-rescale algorithm was used for temperature coupling, and the Isotropic Parrinello-Rahman algorithm for pressure coupling (30). The simulation length was set to 100 ns.

Free energy calculations were performed using the MM-PBSA method with the g_mmpbsa tool (31,32). The polar and apolar components of the solvent effect on free energy were determined using the Poisson-Boltzmann (PB) equation solution and molecular surface area (SA) calculation, respectively. In the vacuum electrostatic calculations, the dielectric constant of the solute was set to 1, while the dielectric constant of the solvent was set to 80. 100 snapshots from the last 10 ns of each 100 ns trajectory were considered in the calculations.

Statistical Analysis

Statistical comparisons between the experimental groups and the control group were performed using a Student's t-test (GraphPad Prism version 10.1.2 for Windows, GraphPad Software, USA). A p-value of less than 0.05 was considered statistically significant.

RESULTS

Evaluating the cytotoxic and cellular effects of thiostrepton on MDA-MB-231 cells

Figure 1A illustrates the changes in cell viability percentages of MDA-MB-231 cells following incubation with thiostrepton for 24 and 48 hours.
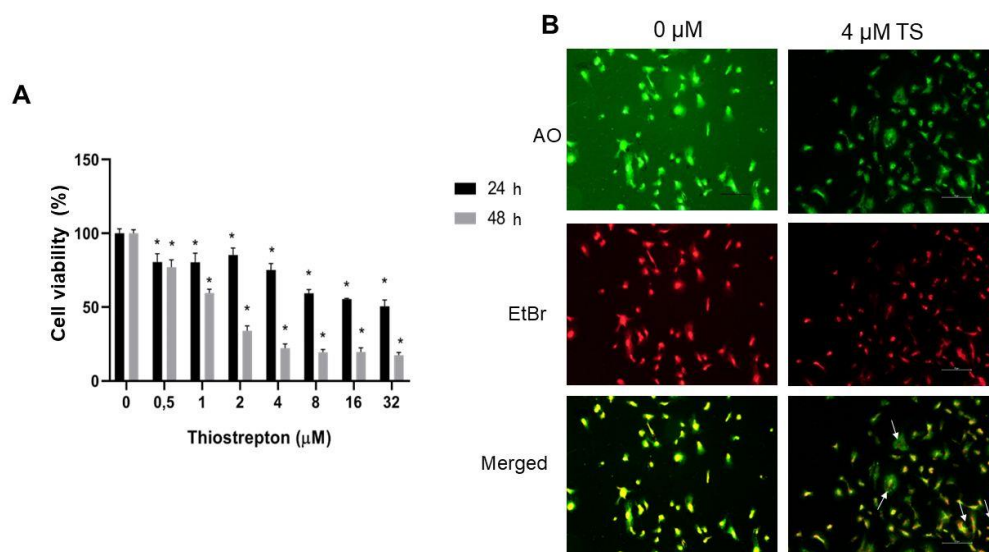
Figure 1. A) MTT assay results illustrating cell viability at different thiostrepton concentrations over 24 and 48 hours. Each value represents the mean ± SEM of four experiments (*p < 0.05). B) Morphologic examination with AO/EB staining after MDA-MB-231 cells were treated with 4 µM thiostrepton for 24 h (➚ indicates apoptotic cells).

Thiostrepton decreased cell viability, which was both dose- and time-dependent, indicating its potent cytotoxic effect on MDA-MB-231 cells. Cell viability decreased dramatically at thiostrepton concentrations of 2 μM and above, especially following 48 hours of treatment. Briefly, 16 μM and 32 μM thiostrepton treatments for 48 hours resulted in about 20% and 10% of cell growth inhibition in MDA-MB-231 cells. Additionally, it was observed that thiostrepton disrupted the membrane and nuclear integrity of the cells and altered cell morphology in an apoptotic manner (Figure 1B). These findings collectively support the potential of thiostrepton as effective agent in promoting apoptosis and inhibiting cancer cell proliferation.

Effects of thiostrepton treatment on Toll-like receptors and apoptotic genes

Thiostrepton treatment reduced the expression of *TLR4, TLR9, Bcl-2*, and *E-cadherin* by 0.29, 0.61-, 0.23-, and 0.63-fold, respectively, while it increased the expression levels of *TLR3, Bax,* and *NF-κB* by 2.19-, 3.17-, and 2.87-fold, respectively (Figure 2). Although the reduction in TLR9 expression was not statistically significant, there was a notable decrease in *TLR4* expression. In contrast, *TLR3* expression was significantly upregulated. Despite the significant increase in *NF-κB* expression, no significant change was detected in *E-cadherin* expression. The pro-apoptotic gene *Bax* was significantly upregulated, while the anti-apoptotic gene *Bcl-2* was markedly downregulated. These results indicate that thiostrepton plays a significant regulatory role in modulating apoptotic pathways and inflammatory responses.
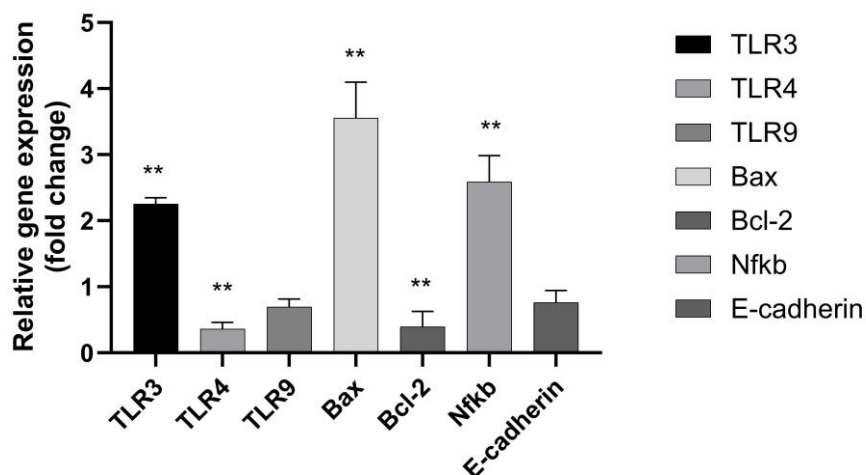
Figure 2. Relative gene expression levels of genes after treating MDA-MB-231 cells with 4 μM thiostrepton for 24 hours. Expression levels were standardized against *β-actin* mRNA levels (** $p < 0.01$).

Molecular dynamics simulation and free energy calculation on TLR4

Our molecular dynamics (MD) simulations of the *TLR4-MD2* domain in complex with thiostrepton provide valuable insights into the stability and interactions of this system. The 100 ns simulations, replicated three times, revealed several interesting features of the complex's behavior over time.

The RMSD analysis (Figure 3A), demonstrated that thiostrepton maintained remarkable stability within the binding cavity throughout the simulation. This stability suggests a strong affinity between the compound and its binding site, which could be indicative of its potential as a *TLR4-MD2* modulator. However, the protein itself showed some interesting dynamics, with a partial loss of stability observed from approximately 75 ns onwards, followed by a return to stability as the simulation approached 100 ns. This transient instability could represent a conformational shift in the protein, possibly induced by the presence of thiostrepton.

The radius of gyration analysis (Figure 3B) corroborated our RMSD findings, showing partial conformational changes in the protein structure from around 60 ns. This observation further supports the idea of thiostrepton-induced conformational shifts in the *TLR4-MD2* complex. The RMSF plot (Figure 3C) revealed that the MD2 domain exhibited greater flexibility compared to other regions of the TLR4 protein. This increased mobility of MD2 could be crucial for accommodating ligands and initiating signaling cascades.
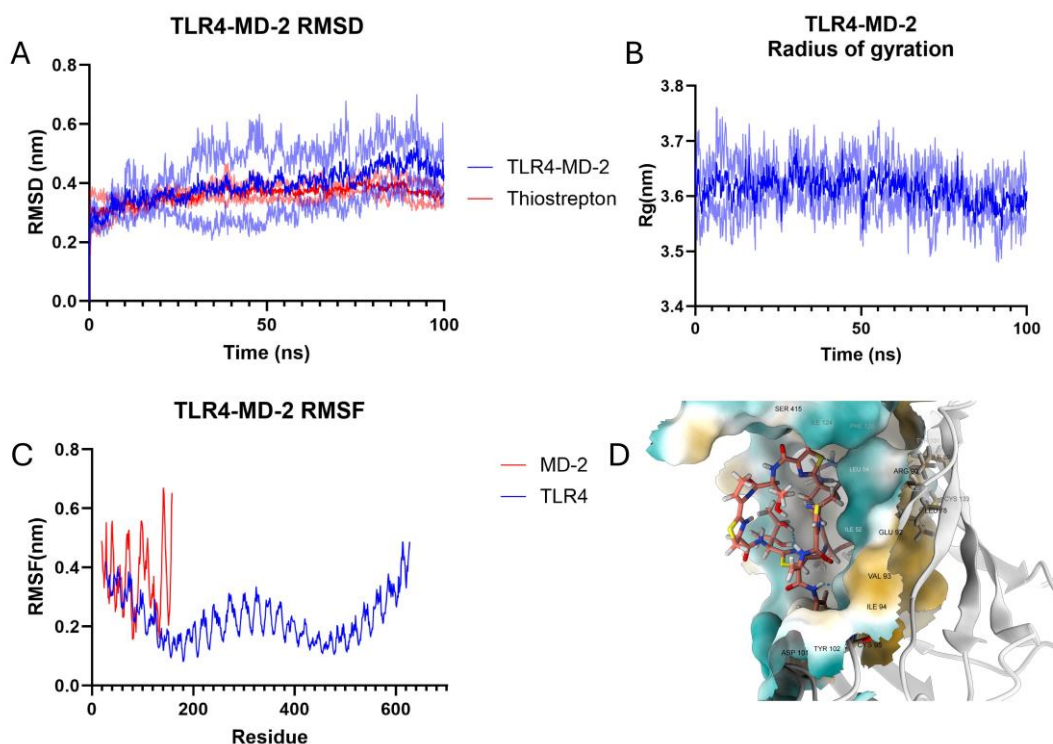
Figure 3. RMSD, Radius of gyration, and RMSF plots of Thiostrepton and TLR4-MD2 domain after 100 ns MD simulation with 3 replicates (A,B,C), and 3D representation of protein-compound interaction (D)

Detailed examination of the thiostrepton-MD2 interaction at the atomic level (Figure 3D) revealed specific residues involved in hydrogen bonding, namely Arg90, Val93, and Cys95. These interactions likely

contribute to the observed stability of thiostrepton within the binding cavity throughout the simulation. This information could be valuable for structure-based drug design efforts targeting the *TLR4-MD2* complex.

The molecular mechanics Poisson-Boltzmann surface area (MM/PBSA) calculations for the binding free energies of the TLR4-MD2 domain and thiostrepton revealed remarkably low values ranging from -319.7 to -403.09 kJ/mol (Table 1). These exceptionally favorable binding energies suggest a strong affinity between thiostrepton and the TLR4-MD2 complex, indicating potential biological significance in their interaction.

Table 1. Binding free energies and contributions between TLR4 MD2 domain and thiostrepton at the end of 100 ns according to the MM/PBSA method

	Repeat-1		Repeat-2		Repeat-3	
	Mean (kJ/mol)	Std. E (kJ/mol)	Mean (kJ/mol)	Std. E (kJ/mol)	Mean (kJ/mol)	Std. E (kJ/mol)
Van der Waals	-427.325	2.616	-245.643	1.46	-277.803	1.837
Electrostatic	-325.151	4.633	-502.786	4.304	-306.616	3.461
Polar solvation	397.704	6.477	454.738	3.831	245.969	4.352
SASA	-47.821	0.241	-26.069	0.142	-36.217	0.197
Binding energy	-403.09	3.276	-319.7	3.455	-374.687	2.618

A detailed analysis of the energetic contributions revealed that van der Waals interactions were the predominant force driving this binding, with a minimum contribution of -427 kJ/mol. This substantial van der Waals contribution underscores the importance of non-covalent interactions in stabilizing the thiostrepton-TLR4-MD2 complex. Such strong van der Waals interactions often indicate a good shape complementarity between the ligand and the binding pocket, which could be crucial for the compound's potential modulatory effects on *TLR4* signaling.

DISCUSSION

Thiostrepton, a polypeptide antibiotic, was first isolated from *Streptomyces azureus* in 1954 and was primarily recognized for its inhibition of protein synthesis (14). It was discovered that siomycin A, a thiazole antibiotic structurally similar to thiostrepton, could downregulate the oncogenic transcription factor FoxM1 in cancer cells (33). This effect was later observed with thiostrepton, leading to a reduction in anchorage-independent growth of cancer cells. Studies demonstrated that thiostrepton selectively induced cell cycle arrest and apoptosis in breast cancer cells by downregulating *FoxM1* expression (19,34,35). In the literature, thiostrepton is also recognized as an inhibitor of *TLR7-9* in psoriatic inflammation. However, the interactions between thiostrepton and these receptors are not well understood (36). Therefore, we investigated the effects of thiostrepton on *TLR3, TLR4,* and *TLR9* in MDA-MB-231 breast cancer.

Studies conducted on various breast cancer and other cancer cell lines have reported IC50 values for thiostrepton ranging from 1 to 5 μM (15,19,35). In our study, cell viability at 8 μM thiostrepton concentration

was 55% after 24 hours, while for the 48-hour treatment, cell viability dropped below 50% at concentrations above 2 μM. These findings align with the existing literature, suggesting that thiostrepton exhibits significant cytotoxicity in TNBC cells. Although thiostrepton has been recognized for its significant effects in cancer cells, its cytotoxic and genotoxic effects on non-malignant healthy cells remain largely unexplored. Therefore, it is imperative that further investigations be conducted to elucidate the cytotoxic effects of thiostrepton on healthy cells.

The significant increase in the expression of *Bax*, a pro-apoptotic gene, indicates that thiostrepton triggers apoptotic pathways, leading to cell death. The decrease in *Bcl-2*, an anti-apoptotic gene, when considered alongside the increase in *Bax*, strongly suggests that thiostrepton promotes cell death by activating apoptotic signaling pathways. Studies have shown that thiazole antibiotics such as siomycin A and thiostrepton induce apoptosis in various types of cancer cells (17,37). Liu et al. found that thiostrepton markedly decreased the proliferation of gastric cancer cells and caused both G0/G1 phase cell cycle arrest and apoptosis (38). Kuttikrishnan et al. reported that downregulation of the *FoxM1/SKP2/MTH1* pathway through thiostrepton resulted in an increased *Bax/Bcl2* ratio and the suppression of anti-apoptotic proteins (39). Along with all these findings, changes in cell morphology and *Bax/Bcl-2* gene expression in our study confirm that thiostrepton induces apoptosis.

The 2.87-fold increase in *NF-κB* expression induced by thiostrepton may indicate activation of cellular inflammatory responses and survival pathways. Peng et al. showed that after incubation with thiostrepton, *NF-κB* activation was observed in latently infected Bcl-2-transduced CD4+ T cells (40). Lai et al. also reported that thiostrepton does not suppress *NF-κB* activation induced by *TNF-α, IL-1*, or other Toll-like receptor (TLR) stimuli (41). Although it has been shown that thiostrepton increases *E-cadherin* expression in cancer cells, our study did not observe a significant change in *E-cadherin* expression (19,42).

TLR3 was shown to trigger apoptosis through the TRIF adaptor protein and type I interferon (IFN) autocrine signaling. It was also noted that *IL-1R-associated kinase-4 (IRAK-4)* and *NF-κB* play key roles in the *TLR3*-mediated apoptotic signaling, leading to the activation of extrinsic caspases (43,44). According to our findings, the increased expression of Toll-like receptor 3 (TLR3) suggests that thiostrepton treatment may activate immune responses, thereby enhancing cellular responses to apoptosis.

Some studies have reported that thiostrepton is a *TLR7-9* inhibitor (41,45). In our study, although a reduction in *TLR9* expression was observed, it was not found to be statistically significant. However, the substantial suppression of *TLR4* expression by thiostrepton is particularly noteworthy. To our knowledge, no studies have examined the effects of thiostrepton on *TLR4*. Consequently, we sought to investigate whether thiostrepton exerts an effect on TLR4 by conducting molecular dynamics and docking studies.

Interestingly, our study appears to be the first to investigate the interaction between thiostrepton and the *TLR4-MD2* complex using MD simulations. This novelty highlights the potential for new insights into *TLR4* modulation. Our findings can be contextualized within the broader literature on *TLR4-MD2*

interactions. For instance, Niu et al. (2018) conducted a similar study with ursolic acid, demonstrating its ability to bind to MD2's active pocket and alter *TLR4* conformation, ultimately reducing *TLR4-MD2* activity. The gradual loss of protein stability observed in their study aligns with our findings, suggesting that this may be a common feature in *TLR4-MD2* interactions with small molecules (46).

To contextualize our findings, it is instructive to compare them with related studies in the literature. For instance, Sun et al. conducted a comprehensive study on PCP-W1, a polysaccharide isolated from *Poria coco*s. Their research encompassed structural analysis, investigation of immunomodulatory effects in RAW 264.7 cells, and *in silico* studies including molecular docking and molecular dynamics simulations to elucidate the binding mechanism of PCP-W1 to the TLR4/MD2 complex. Their findings demonstrated that PCP-W1 induced M1-type macrophage polarization via the TLR4/MD2/NF-κB pathway. Notably, their computational analysis yielded a binding free energy of -288.23 kJ/mol for the interaction between PCP-W1 and MD2 (47).

When juxtaposed with our results, it becomes evident that thiostrepton exhibits a more favorable binding affinity to the TLR4-MD2 complex compared to PCP-W1. The lower (more negative) binding free energy we observed for thiostrepton suggests a potentially stronger interaction with the TLR4-MD2 complex. This enhanced binding affinity could translate to more potent modulation of TLR4-mediated signaling pathways.

However, it is crucial to interpret these computational findings with caution. While binding free energy calculations provide valuable insights into the thermodynamics of protein-ligand interactions, they do not always directly correlate with biological activity. Factors such as bioavailability, off-target effects, and the complex cellular milieu can significantly influence a compound's efficacy *in vivo*.

Furthermore, the structural differences between thiostrepton (a cyclic oligopeptide) and PCP-W1 (a polysaccharide) should be considered when comparing their binding energies. These distinct molecular architectures may interact with the *TLR4-MD2* complex through different mechanisms, potentially activating or inhibiting diverse downstream signaling cascades.

CONCLUSION

This study demonstrated that thiostrepton promotes apoptosis and reduces cell viability in TNBC cells. Additionally, for the first time in the literature, it showed the effects of thiostrepton on *TLR4* gene expression and its interaction with the *TLR4-MD2* complex using MD simulations. However, there are several suggestions for more detailed analysis of these results. While our simulations provide important computational insights, it is crucial to acknowledge the limitations of this approach. MD simulations, while powerful, represent a simplified model of complex biological systems. Therefore, experimental validation of these findings would be a logical next step. Extending the simulation time beyond 100 ns could potentially

reveal longer-term dynamics of the system. Moreover, to validate the biological relevance of the *in vitro* and *in silico* findings, the effects of thiostrepton on *TLR4* should be examined in different TNBC cell lines or animal models *in vivo.*

Acknowledgments

None

Authorship contributions

F.D.K; Conceptualization, Methodology, Writing—Original Draft. Z.D.; Methodology, Writing Original Draft. A.D.O;   Conceptualization, Methodology, Supervision.

Data availibity statement

The data that support the findings of this study are available from the corresponding author upon reasonable request.

Declaration of competing interest

No conflict of interest was declared by the authors

Ethics

This study does not contain any experiments with human participants or animals conducted by the authors.

Funding

This work has not received any funding support.

REFERENCES

1.   Foulkes WD, Smith IE, Reis-Filho JS. Triple-Negative Breast Cancer. N Engl J Med. 2010;363(20):1938–48.

2.   Javaid N, Choi S. Toll-like Receptors from the Perspective of Cancer Treatment. Cancers 2020;12(2):297.

3.   Rakoff-Nahoum S, Medzhitov R. Toll-like receptors and cancer. Nat Rev Cancer. 2009;9(1):57–63.

4.   Ren T, Wen ZK, Liu ZM, Liang YJ, Guo ZL, Xu L. Functional expression of TLR9 is associated to the metastatic potential of human lung cancer cell. Cancer Biol Ther. 2007;6(11):1704-1709.

5.   Butkowsky C, Aldor N, Poynter SJ. Toll-like receptor 3 ligands for breast cancer therapies (Review). Mol Clin Oncol. 2023;19(2):1-8.

6.   Shi S, Xu C, Fang X, Zhang Y, Li H, Wen W, et al. Expression profile of Toll-like receptors in human breast cancer. Mol Med Rep. 2020; 21(2):786-794.

7.   Fan L, Sui XY, Jin X, Zhang WJ, Zhou P, Shao ZM. High expression of TLR3 in triple-negative breast cancer predicts better prognosis—data from the Fudan University Shanghai Cancer Center cohort and tissue microarrays. BMC Cancer. 2023;23(1):298.

8.   Tuomela J, Sandholm J, Karihtala P, Ilvesaro J, Vuopala KS, Kauppila JH, et al. Low TLR9 expression defines an aggressive subtype of triple-negative breast cancer. Breast Cancer Res Treat. 2012;135(2):481-493.

9.   Ahmed M, Maldonado AM, Durrant JD. From byte to bench to bedside: molecular dynamics simulations and drug discovery.

BMC Biol. 2023;21(1):299.

10.   Salo-Ahen OMH, Alanko I, Bhadane R, Bonvin AMJJ, Honorato RV, Hossain S, et al. Molecular dynamics simulations in drug discovery and pharmaceutical development. Processes. 2020;9(1):71.

11.   Muhammed MT, Aki-Yalcin E. Molecular docking: principles, advances, and its applications in drug discovery. Lett Drug Des Discov. 2024;21(3):480–95.

12.   Nascimento IJ dos S, de Aquino TM, da Silva-Júnior EF. The new era of drug discovery: The power of computer-aided drug design (CADD). Lett Drug Des Discov. 2022;19(11):951–5.

13.   Ain Q ul, Batool M, Choi S. TLR4-targeting therapeutics: structural basis and computer-aided drug discovery approaches. Molecules. 2020;25(3):627.

14.   Bailly C. The bacterial thiopeptide thiostrepton. An update of its mode of action, pharmacological properties and applications. Eur J Pharmacol. 2022;914:174661.

15.   Bhat UG, Halasi M, Gartel AL. Thiazole antibiotics target FoxM1 and induce apoptosis in human cancer cells. PLoS One. 2009;4(5):e5592.

16.   Lai C-Y, Yeh D-W, Lu C-H, Liu Y-L, Huang L-R, Kao C-Y, et al. Identification of Thiostrepton as a Novel Inhibitor for Psoriasis-like Inflammation Induced by TLR7–9. J Immunol. 2015;195(8).

17.   Kwok JMM, Myatt SS, Marson CM, Coombes RC, Constantinidou D, Lam EWF. Thiostrepton selectively targets breast cancer cells through inhibition of forkhead box M1 expression. Mol Cancer Ther. 2008;7(7):2022–32.

18.   Cai X, Xiao W, Shen J, Lian H, Lu Y, Liu X, et al. Thiostrepton and miR-216b synergistically promote osteosarcoma cell cytotoxicity and apoptosis by targeting FoxM1. Oncol Lett [Internet]. 2020;20(6):1–1.

19.   Demirtas Korkmaz F, Dogan Turacli I, Esendagli G, Ekmekci A. Effects of thiostrepton alone or in combination with selumetinib on triple-negative breast cancer metastasis. Mol Biol Rep [Internet]. 2022;49(11):10387–97.

20.   Chomczynski P, Sacchi N. Single-step method of RNA isolation by acid guanidinium thiocyanate-phenol-chloroform extraction. Anal Biochem. 1987;162(1):156-159.

21.   Park BS, Song DH, Kim HM, Choi B-S, Lee H, Lee J-O. The structural basis of lipopolysaccharide recognition by the TLR4–MD-2 complex. Nature. 2009;458(7242):1191–5.

22.   Kim S, Thiessen PA, Bolton EE, Chen J, Fu G, Gindulyte A, et al. PubChem Substance and Compound databases. Nucleic Acids Res. 2016;44(D1):D1202–13.

23.   Trott O, Olson AJ. AutoDock Vina: improving the speed and accuracy of docking with a new scoring function, efficient optimization, and multithreading. J Comput Chem. 2010;31(2):455–61.

24.   Dallakyan S, Olson AJ. Small-Molecule Library Screening by Docking with PyRx. In 2015 p. 243–50.

25.   Abraham MJ, Murtola T, Schulz R, Páll S, Smith JC, Hess B, et al. GROMACS: High performance molecular simulations through multi-level parallelism from laptops to supercomputers. SoftwareX. 2015;1–2:19–25.

26.   Lindorff-Larsen K, Piana S, Palmo K, Maragakis P, Klepeis JL, Dror RO, et al. Improved side-chain torsion potentials for the Amber ff99SB protein force field. Proteins. 2010;78(8):1950–8.

27.   Essmann U, Perera L, Berkowitz ML, Darden T, Lee H, Pedersen LG. A smooth particle mesh Ewald method. J Chem Phys. 1995;103(19):8577.

28.   Hess B, Bekker H, Berendsen HJC, Fraaije JGEM. LINCS: A Linear Constraint Solver for Molecular Simulations. J Comput Chem. 1997;18:1463–72.

29.   Lemak AS, Balabaev NK. On the Berendsen thermostat. Mol Simul. 1994;13(3):177–87.

30.   Martoňák R, Laio A, Parrinello M. Predicting Crystal Structures: The Parrinello-Rahman Method Revisited. Phys Rev Lett. 2003;90(7): 075503.

31.   Wang E, Sun H, Wang J, Wang Z, Liu H, Zhang JZH, et al. End-Point Binding Free Energy Calculation with MM/PBSA and MM/GBSA: Strategies and Applications in Drug Design [Internet]. Vol. 119, Chemical Reviews. American Chemical Society.2019 p. 9478–508.

32.   Kumari R, Kumar R, Lynn A, Lynn A. g_mmpbsa—A GROMACS Tool for High-Throughput MM-PBSA Calculations. J Chem Inf Model. 2014;54(7):1951–62.

33.   Gartel AL. FoxM1 inhibitors as potential anticancer drugs. Expert Opin Ther Targets. 2008;12(6):663–5.

34.   Wongkhieo S, Numdee K, Lam EWF, Choowongkomon K, Kongsema M, Khongkow M. Liposomal Thiostrepton Formulation and Its Effect on Breast Cancer Growth Inhibition. J Pharm Sci. 2021;110(6):2508–16.

35.   Kongsema M, Wongkhieo S, Khongkow M, Lam E, Boonnoy P, Vongsangnak W, et al. Molecular mechanism of Forkhead box M1 inhibition by thiostrepton in breast cancer cells. Oncol Rep . 2019;42(3):953–62.

36.   Lai CY, Su YW, Lin KI, Hsu LC, Chuang TH. Natural Modulators of Endosomal Toll-Like Receptor-Mediated Psoriatic Skin Inflammation. Journal of Immunology Research. 2017;2017:1-15.

37.   Jiang L, Wang P, Chen L, Chen H. Down-regulation of FoxM1 by thiostrepton or small interfering RNA inhibits proliferation, transformation ability and angiogenesis, and induces apoptosis of nasopharyngeal carcinoma cells. Int J Clin Exp Pathol. 2014;7(9):5450–60.

38.   Liu SX, Zhou Y, Zhao L, Zhou LS, Sun J, Liu GJ, et al. Thiostrepton confers protection against reactive oxygen species-related apoptosis by restraining FOXM1-triggerred development of gastric cancer. Free Radic Biol Med. 2022 20;193:385–404.

39.   Kuttikrishnan S, Prabhu KS, Khan AQ, Alali FQ, Ahmad A, Uddin S. Thiostrepton inhibits growth and induces apoptosis by targeting FoxM1/SKP2/MTH1 axis in B-precursor acute lymphoblastic leukemia cells. Leuk Lymphoma. 2021;62(13):3170–80.

40.   Peng W, Hong Z, Chen X, Gao H, Dai Z, Zhao J, et al. Thiostrepton reactivates latent HIV-1 through the p-TEFb and NF-κB pathways mediated by heat shock response. Antimicrob Agents Chemother. 2020;64(5):10-1128..

41.   Lai C-Y, Yeh D-W, Lu C-H, Liu Y-L, Huang L-R, Kao C-Y, et al. Thiostrepton inhibits psoriasis-like inflammation induced by TLR7, TLR8, and TLR9. J Immunol. 2016 1;196(1_Supplement):124.41.

42.   Hsu Y Bin, Lan MC, Kuo YL, Huang CYF, Lan MY. A preclinical evaluation of thiostrepton, a natural antibiotic, in nasopharyngeal carcinoma. Invest New Drugs. 2020;38(2): 264-273.

43.   Salaun B, Coste I, Rissoan M-C, Lebecque SJ, Renno T. TLR3 Can Directly Trigger Apoptosis in Human Cancer Cells. J Immunol. 2006;176(8):4894–901.

44.   Butkowsky C, Aldor N, Poynter S. Toll-like receptor 3 ligands for breast cancer therapies (Review). Mol Clin Oncol. 2023;19(2):1-8.

45.   Esparza K, Oliveira SD, Castellon M, Minshall RD, Onyuksel H. Thiostrepton-Nanomedicine, a TLR9 Inhibitor, Attenuates Sepsis-Induced Inflammation in Mice. Yokota S, editor. Mediators Inflamm. 2023;2023:1–11.

46.   Niu X, Yu Y, Guo H, Yang Y, Wang G, Sun L, et al. Molecular modeling reveals the inhibition mechanism and binding mode of ursolic acid to TLR4-MD2. Comput Theor Chem. 2018;1123:73–8.

47.   Sun M, Yao L, Yu Q, Duan Y, Huang J, Lyu T, et al. Screening of Poria cocos polysaccharide with immunomodulatory activity and its activation effects on TLR4/MD2/NF-κB pathway. Int J Biol Macromol. 2024;273:132931.

Research Article

DECIPHERING THE IMPACT OF COLLAGENASE TREATMENT DURATION ON PRIMARY BREAST CANCER CELL PROTEOME: A COMPREHENSIVE STUDY

Merve Gülsen BAL ALBAYRAK [1], Murat KASAP [1], Gürler AKPINAR [1], Sevinç YANAR [2], Turgay ŞİMŞEK [3], Nuh Zafer CANTÜRK [3]

[1] Department of Medical Biology, Medical School, Kocaeli University, 41001 Kocaeli, TURKIYE
[2] Department of Histology and Embryology, Medical School, Sakarya University, Sakarya, TURKIYE
[3] Department of General Surgery, Medical School, Kocaeli University, 41001 Kocaeli, TURKIYE
Correspondence: mervegulsenbal@gmail.com

ABSTRACT

Objective: Primary cell isolation is essential for studying cellular behavior and disease mechanisms, with collagenase-mediated tissue dissociation playing a critical role in the process. However, the impact of collagenase treatment duration on the proteome of primary cells, particularly in breast cancer research, remains underexplored. This study aims to investigate the effects of collagenase II treatment duration on the proteomic profiles of primary breast cancer cells.

Materials and Methods: Breast cancer tissues from patients diagnosed with infiltrating ductal carcinoma were treated with collagenase II for either 1 or 3 hours. Subsequent proteomic analysis was performed using liquid chromatography-tandem mass spectrometry (LC-MS/MS). Identified proteins were subjected to bioinformatic analyses to determine the functional implications of the proteomic changes induced by the different treatment durations.

Results: Bioinformatic analyses showed that 1-hour treatment predominantly affected proteins involved in cytoskeletal organization and cell adhesion, with significant enrichment in actin cytoskeleton dynamics and structural molecule activity. In contrast, 3-hour treatment led to significant metabolic reprogramming, with enhanced regulation of pathways involved in energy production, including the TCA cycle and glycolysis.

Conclusion: This study reveals for the first time that, collagenase II treatment duration significantly alters the proteomic profile of primary breast cancer cells, with shorter durations affecting structural proteins and longer durations inducing metabolic changes. Optimizing treatment time is crucial for targeted proteomic studies.

Keywords: Primary cells, breast cancer, collagenase, treatment duration, proteomics

INTRODUCTION

Cell culture studies serve as vital tools to uncover the complexity of cellular behavior and provide crucial information for understanding disease pathology and therapeutic development (1). Central to these efforts is the isolation and cultivation of primary cells that closely mimic in vivo cellular physiology when compared to immortalized cell lines (2). Among primary cell isolation techniques, enzymatic tissue dissociation using collagenase is especially important (3).

Collagenase, an enzyme that cleaves peptide bonds within collagen fibers, plays an important role in tissue dissociation and facilitates the release of individual cells from complex tissue matrices (3). Collagen, a key component of the extracellular matrix (ECM), provides structural support to tissues and serves as a scaffold for cell adhesion and migration. Collagenase specifically degrades collagen in the ECM, allowing for the release of cells embedded within the tissue matrix (4). Collagenase exerts its enzymatic activity by cleaving specific peptide bonds within the triple helical structure of collagen molecules. Specifically, collagenase targets the peptide bonds between glycine and other amino acids in the collagen polypeptide chain, leading to the degradation of collagen fibers into smaller fragments. This enzymatic degradation softens the tissue matrix, facilitating the dissociation of cells from the surrounding ECM (5).

Several types of collagenases, derived from bacterial and mammalian sources, are used in primary cell isolation protocols. Among the most used are Collagenase I, Collagenase II, and Collagenase IV, each exhibiting distinct substrate specificities and enzymatic properties (6,7). Collagenase I (also known as Clostridium histolyticum collagenase) preferentially cleaves native collagen fibrils, making it suitable for the isolation of primary cells from tissues rich in type I collagen, such as skin and bone. Collagenase II (derived from Clostridium histolyticum) exhibits broader substrate specificity, allowing for the efficient dissociation of various tissue types, including cancer tissues abundant in both type I and type III collagens (8). Collagenase IV, sourced from Vibrio proteolyticus, demonstrates high specificity for denatured collagen, making it suitable for the isolation of cells from decellularized tissues and cell culture applications (9).

Numerous studies have explored the use of collagenases in primary cell isolation, assessing its effectiveness across different experimental conditions and tissue types (10–12). These studies used collagenase at various concentrations, incubation times, and temperatures, reflecting the different approaches researchers have taken to optimize tissue dissociation protocols. While some studies advocate long-term collagenase treatment to maximize cell yield and viability, others recommend shorter incubation periods to minimize potential changes in cellular phenotype and function (13,14). Furthermore, inconsistencies exist regarding the effect of collagenase treatment duration on downstream assays, including proteomic profiling, and conflicting reports highlight the need for further research.

Despite the wealth of literature on collagenase-mediated primary cell isolation, a notable gap exists in our understanding of the relationship between collagenase treatment duration and the resulting proteome. In breast cancer research, there is a notable lack of studies systematically investigating the effects of varying collagenase treatment durations on the proteomic composition of primary cells (15). This lack of understanding presents a major challenge for researchers working to unravel the molecular complexities of breast cancer progression and to create targeted therapeutic strategies.

In light of these considerations, the current study aimed to address this issue by comprehensively investigating how collagenase treatment duration affects the proteome of primary breast cancer cells. Through sensitive experiments and comprehensive LC-MS/MS analysis, we aimed to reveal the molecular effects of collagenase-mediated tissue dissociation and provide valuable information to optimize primary cell isolation protocols for subsequent proteomic studies. By unraveling the complex relationship between collagenase treatment duration and the primary cell proteome, our goal is to improve the reproducibility and reliability of experimental results, thereby advancing our understanding of breast cancer biology and aiding the development of innovative therapeutic approaches.

MATERIALS AND METHODS

Patient Characteristics

Breast cancer tissues were collected under ethical approval number KU GOKAEK-2019/16.04 2019/139 by Ethics Committee of Kocaeli University. Patients that were diagnosed as infiltrating ductal carcinoma (IDC) by the General Surgery Clinic of Kocaeli University School of Medicine between years 2019 and 2021 were chosen. Patients were selected among the ones that were not received any drug therapy. After removal, the tissues were washed with proteomic wash buffer (10 mM Tris buffer containing 250 mM sucrose at pH 7.4), and then immediately taken to the collagenase treatment procedure within 30 minutes.

Cell Culture and Collegenase II treatment

The tissues were diced into small pieces and washed with wash buffer to remove excess blood. After centrifugation at 10000×g, 500 μl of DMEM (Thermo Fisher Scientific, USA) medium containing 300 U/ml Collagenase II was added to the tissue pellets. Two groups were established for collagenase treatment durations of 1 hour and 3 hours. The tubes containing the tissue and medium-collagenase mixture were incubated at 37°C for either 1 hour or 3 hours, depending on the group. Following incubation, the tubes were centrifuged at 7000×g at 4°C for 10 minutes. Supernatants were removed, and EASYpack Protease Inhibitor Cocktail (cOmplete™ ULTRA Tablets, Merck, Darmstadt, Germany) was added to the pellets. Protein isolation experiments were then carried out using these samples.

Protein Isolation

Stainless steel beads (1.4 mm) were added to the tubes containing tissues treated with collagenase II. The tissues were then homogenized using a bead-beater (Bullet Blender, Next Advance, Troy, NY, USA) at speed 9 for 4 minutes, repeated five times. The homogenates were centrifuged for 10 minutes at 10,000×g at 4°C, and the supernatant was transferred into fresh tubes. These tubes were centrifuged again for 45 minutes at 18,000×g at 4°C to obtain a clear crude extract, and the supernatants were transferred into fresh tubes and labeled. Protein concentrations were measured using the Bradford assay (Bio-Rad, Hercules, CA, USA) with a NanoDrop ND-1000 spectrophotometer (Thermo Scientific, USA). The protein extracts were briefly immersed in liquid nitrogen for approximately 30 seconds to rapidly freeze them, and then transferred to storage at -80°C for further use.

Preperation of Protein Pools and In Solution Tryptic Digestion

To prevent sample-to-sample variation, protein pools were created by mixing equal amounts of protein from each patient's sample into a single tube. Before LC-MS/MS experiments, the protein pools were cleaned to remove impurities using TCA/acetone precipitation. Briefly, 200 µg of protein from each pool was diluted to 90 µl with distilled water, and 10 µl of 0.2% DOC (deoxycholate.Na) solution was added. The samples were incubated on ice for 15 minutes. Next, 10 µl of 72% TCA (trichloroacetic acid) was added, and the samples were incubated on ice for another 15 minutes. Following centrifugation at 12,000×g for 10 minutes at 4°C, the supernatants were removed, and 1 ml of ice-cold acetone was added. The tubes were mixed well with a vortex and incubated at -20°C for 30 minutes. After incubation, the tubes were centrifuged again at 12,000×g for 10 minutes at 4°C. The supernatants were removed, and the protein pellets were air-dried and dissolved in 50 mM ammonium bicarbonate. Protein concentrations of the pooled samples were determined using the Qubit Protein Assay (Thermo Fisher Scientific, USA) before further experiments.

Prior to LC-MS/MS analysis, proteins were digested into peptides using in-solution tryptic digestion and guanidination kit (Thermo Scientific, USA) as described in our previous work (16).

Liquid chromatography (LC)-tandem MS/MS analysis

The digested peptides were analyzed by nLC-MS/MS, following the method outlined by Yanar et al. (17) Data-dependent acquisition was utilized, targeting the top 10 precursor ions for MS/MS analysis, with an MS scan mass range of 400–2000 m/z. Raw data were worked using Proteome Discoverer SEQUEST (version 2.2; Thermo Fisher Scientific) according to the parameters specified in our previous work (17). Protein identification was performed against the Uniprot/Swissprot database.

Bioinformatic analysis

Protein-protein interactions, biological functions, and molecular pathways linked to identified proteins were explored using Gene Ontology (GO) and Kyoto Encyclopedia of Genes and Genomes (KEGG) pathway enrichment analyses, as previously described (17). STRING (https://string-db.org) was employed with previous parameters and interaction sources(17). Results showing significant findings with a false discovery rate (FDR) below 1e-05 were visualized and analyzed using Adobe Illustrator Version 6. Enrichment analyses included GO terms (biological processes (BP), cellular components (CC), molecular functions (MF)), KEGG pathways, Reactome (RKTM), and WikiPathways (WP) with a p-value < 0.05. Bubble plots showing the enriched results were created using SRPlot.

RESULTS

Comparative proteome analysis of primary cells

The effects of collagenase II treatment duration on cells were assessed by examining alterations in global protein expression profiles. The digested proteins from each group were analyzed using nHPLC coupled with LC-MS/MS. Proteomic analysis identified 272 proteins in cells treated with collagenase II for 1 hour, while 259 proteins were identified in cells treated for 3 hours. After filtering for proteins identified by at least two unique peptides, the number of identified proteins decreased to 127 for the 1-hour group and 118 for the 3-hour group. A comparison of the identified proteins between the two groups revealed 162 common proteins, as illustrated in the Venn diagram (Figure 1). Additionally, 110 proteins were unique to the 1-hour treatment group, and 97 proteins were unique to the 3-hours treatment group.
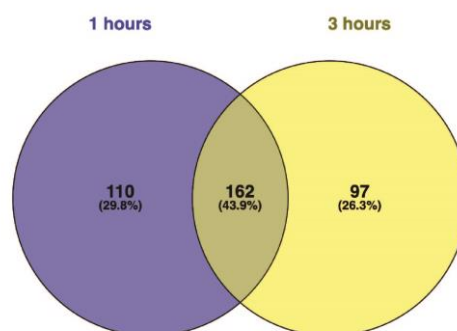
Figure 1. Venn diagram of LC-MS/MS identified proteins for the 1-hour and 3-hour collagenase treatment groups. The numbers represent the gene counts for the corresponding groups.

Bioinformatic analysis of identified proteins

To link the identified proteins with protein networks and molecular pathways, GO terms related to Biological Process (BP), Cellular Component (CC), Molecular Function (MF), along with KEGG pathways,

Reactome, and WikiPathways, were analyzed using the STRING database. The outcomes from analyses were integrated and visualized as bubble plots generated with SRPlot (Figure 2 and Figure 3).

For cells treated for 1 hour, GO analysis indicated significant regulation of 'cytoskeleton organization' (Biological Process) and 'structural molecule activity' (Molecular Function). KEGG pathway analysis identified the most enriched pathways as "Regulation of actin cytoskeleton" and "citrate cycle (TCA cycle)." WP analysis highlighted key terms, with a notable entry being "metabolic reprogramming in colon and pancreatic cancer." RKTM analysis uncovered significant pathways, including "Axon guidance" and "signaling by Rho GTPases" (see Figure 2a and b).
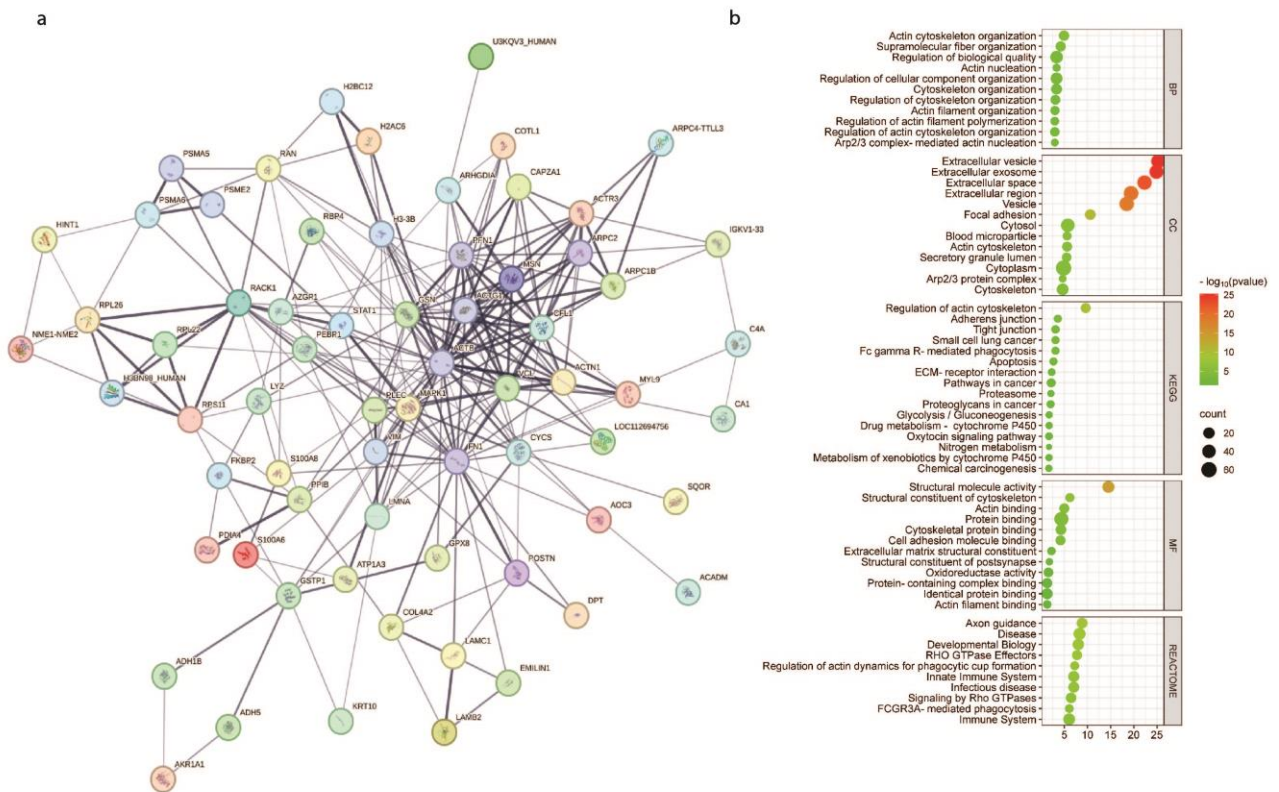
Figure 2. Pathway enrichment analyses of differentially regulated proteins identified through LC-MS/MS. a. show the STRING network analyses for the 1-hour. b. illustrate the enrichment analysis results using bubble plots for the 1-hour treatment group, based on data from Gene Ontology (GO) Biological Process (BP), Cellular Component (CC), Molecular Function (MF), Kyoto Encyclopedia of Genes and Genomes (KEGG), and Reactome (RKTM)

For cells treated for 3 hours, GO analysis identified important terms, with notable regulations in "Generation of precursor metabolites and energy" and "aerobic respiration" (biological process category) and "RNA binding" (molecular function category). KEGG pathway analysis revealed the enriched pathway "carbon metabolism." WP analysis highlighted significant mechanisms including "TCA cycle" and "Metabolic reprogramming." RKTM analysis showed crucial regulated pathways, such as "Citric acid cycle" and "metabolism" (see Figure 3a and b). Overall, bioinformatic analyses revealed that in cells treated for 1 hour,

the key regulatory trends were associated with actin cytoskeleton dynamics, structural organization, cell adhesion, and related signaling pathways. Conversely, in cells treated for 3 hours, the main regulatory activities were linked to metabolic processes, including energy generation, ATP metabolism, carbon metabolism, and the TCA cycle. Further analysis showed variations in expression levels among the proteins common to both treatment durations. This indicates that while some core proteins remain consistent across different treatment times, their functional roles and interactions may be modulated by the extent of collagenase exposure.
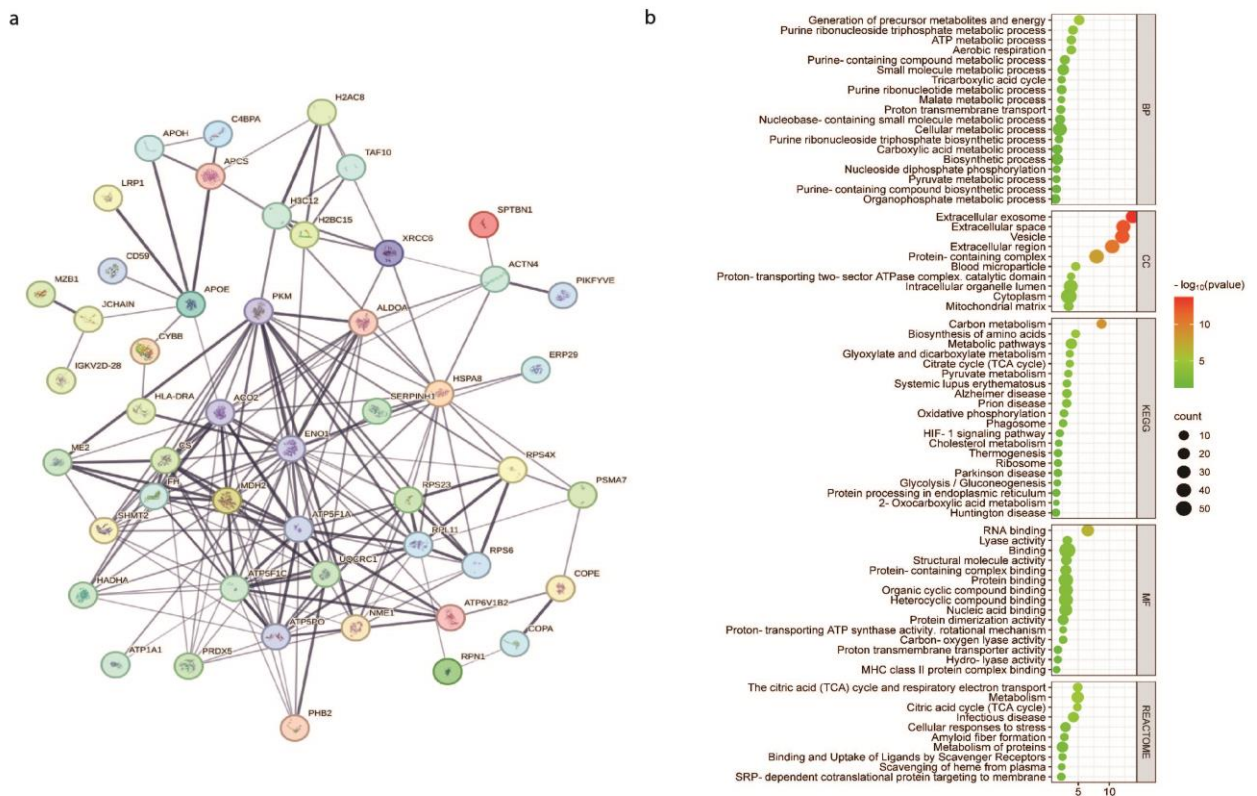
Figure 3. Pathway enrichment analyses of differentially expressed proteins, identified via LC-MS/MS, a. demonstrate STRING network analyses corresponding to the 3-hour treatment group. b. Enrichment analysis outcomes are visualized through a bubble plot for the 3-hour treatment, utilizing datasets derived from Gene Ontology (GO) terms across Biological Processes (BP), Cellular Components (CC), Molecular Functions (MF), along with the Kyoto Encyclopedia of Genes and Genomes (KEGG), and Reactome (RKTM) databases.

DISCUSSION

The study aimed to investigate the impact of different collagenase II treatment durations on the proteome of primary breast cancer cells. Bioinformatic analyses were conducted to explore the functional implications of the identified proteins. Our findings reveal significant insights into the influence of enzyme treatment duration on cellular protein expression and subsequent biological processes.

Collagenase is widely used for the isolation of primary cells from various tissues due to its ability to degrade collagen in the extracellular matrix (ECM). This enzymatic activity facilitates the release of cells from tissues, which can then be cultured and analyzed. Different types of collagenases (e.g., types I, II, and IV) are used depending on the tissue type and the specific requirements of the study (3,4). Collagenase II, in particular, is frequently used for tissues rich in collagen type II, such as cartilage and some tumors. The effectiveness of the enzyme and the viability of the cells can be affected by factors such as enzyme concentration and incubation time (18,19).

Our study revealed distinct protein expression profiles between the two treatment periods. Bioinformatic analysis of the regulated proteins identified in 1-hour treated cells revealed significant regulatory patterns related to cytoskeletal organization, structural molecule activity, and cell adhesion. Proteins involved in these pathways include actin, myosin, and various actin-binding proteins such as filamin and profilin. These proteins work together to remodel the cytoskeleton in response to external signals, allowing cells to adapt their structure and function (20). Structural molecule activity is crucial for maintaining the integrity and functionality of cellular components. Proteins such as tubulins and intermediate filaments are essential for forming the structural framework of the cell, providing mechanical support, and participating in various cellular processes, including mitosis and intracellular transport.

Cell adhesion molecules (CAMs) like cadherins and integrins play a vital role in mediating cell-cell and cell-ECM interactions, crucial for tissue formation, maintenance, and repair, and participate in signal transduction pathways that regulate cell proliferation, differentiation, and migration (21). Specifically, the regulation of actin cytoskeleton and focal adhesion pathways was prominent according to our results, indicating that shorter collagenase treatment may influence cell adhesion and cancer cell migration processes. This is consistent with the fact that shorter collagenase treatment durations tend to preserve more of the structural and signaling proteins involved in cytoskeletal integrity and cell-matrix interactions. Collagenase, by breaking down extracellular matrix (ECM) components, facilitates the release of cells while maintaining key functional proteins critical for cell attachment and movement. This aligns with studies that have used collagenase for primary cell isolation where the emphasis was on minimizing enzyme exposure to retain cellular functions linked to the cytoskeleton and adhesion properties (13,14). The differential expression of proteins involved in actin cytoskeleton regulation in the 1-hour treated cells suggests a transient response aimed at remodeling the cytoskeleton to facilitate cell detachment and survival. Proteins such as Rho GTPases, which are known to regulate actin dynamics, were significantly enriched. This aligns with the findings of other studies that have reported the role of Rho GTPases in mediating cellular responses to mechanical and enzymatic stress (22).

In comparison, cells treated for 3 hours showed a different proteomic landscape, with a significant emphasis on metabolic processes, including energy generation, ATP metabolism, and the TCA cycle. The

enriched pathways suggest that extended collagenase treatment induces a metabolic shift, likely as an adaptive response to prolonged enzymatic exposure. This metabolic reprogramming is consistent with findings that describe how cells reprogram their metabolism to adapt to various stress conditions, including enzymatic treatment (23). The TCA cycle (Krebs cycle) and oxidative phosphorylation are central to cellular energy production. Key enzymes such as citrate synthase, isocitrate dehydrogenase, and succinate dehydrogenase are involved in these pathways, facilitating the conversion of glucose and other nutrients into ATP, the cell's primary energy currency (24). Cancer cells often undergo metabolic reprogramming to support rapid growth and survival under adverse conditions, involving increased glycolysis (Warburg effect), enhanced glutaminolysis, and altered lipid metabolism (23,24). The enhanced metabolic activity observed in the 3-hour treated group reflects significant metabolic reprogramming, possibly as a mechanism to cope with the stress induced by prolonged enzymatic exposure. This metabolic shift suggests that extended collagenase treatment prompts cells to reallocate resources towards maintaining energy balance and supporting survival under adverse conditions.

The common proteins observed in both treatment groups, despite differences in their expression levels, indicate that certain core proteins are consistently present across varying treatment durations. However, their functional roles and interactions may be influenced by the degree of collagenase exposure. This variable response to enzymatic treatment reveals the intricate balance between preserving cellular structure and adapting to metabolic changes, highlighting the necessity for customized enzymatic dissociation protocols. Overall, in terms of specific proteins and pathways, the regulation of the actin cytoskeleton pathway in the 1-hour treatment group suggests that these cells maintain better structural integrity and are potentially more suited for studies involving cell motility and morphology. The actin cytoskeleton plays a crucial role in cell shape, division, and intracellular transport, and its regulation is vital for understanding cancer cell metastasis (20). For the 3-hour treatment group, the upregulation of metabolic pathways, such as the TCA cycle and glycolysis, underscores the cells' metabolic flexibility and adaptability under prolonged enzymatic stress. These findings are significant as they suggest that extended collagenase treatment primes the cells for higher metabolic activity, which might be beneficial in studies focusing on cancer cell metabolism and drug response.

CONCLUSION

In conclusion, our study shows that varying collagenase II treatment durations significantly affect the proteomic structure of primary breast cancer cells. Shorter treatment durations primarily affect proteins involved in cytoskeletal organization and cell adhesion, highlighting the critical roles of these proteins in maintaining cellular integrity and functionality during initial enzymatic exposure. Conversely, extended collagenase treatment triggers significant metabolic reprogramming, underscoring the adaptation of cells to

prolonged stress through increased energy production pathways. These differential protein expression patterns highlight the need to optimize collagenase treatment conditions based on the specific biological processes being investigated.

Acknowledgments

Not applicable

Authorship contributions

Study conception and experimental design were performed by MGBA, M.K. and G.A. Tissue collection with surgeries and storage were performed by T.S. and N.Z.C. Sample preparation and protein isolation were performed by M.G.B.A. and M.K. LC-MS/MS analysis were performed by M.G.B.A, M.K, and G.A. Bioinformatic analysis were performed by M.G.B.A and S.Y. The first draft of the manuscript was written by M.G.B.A. and S.Y. Writing, review, and editing the draft were performed by G.A. and M.K. All authors commented on previous versions of the manuscript. All authors read and approved the final manuscript.

Data availibity statement

The datasets produced during this study can be obtained from the corresponding author upon reasonable request.

Declaration of competing interest

The authors report no conflicts of interest.

Ethics

This study has been approved by the Ethics Committee of Kocaeli University with approval number; KU GOKAEK-2019/16.04 2019/139.

Funding

Not applicable

REFERENCES

1 . Hudu SA, Alshrari AS, Syahida A, Sekawi Z. Cell Culture, Technology: Enhancing the Culture of Diagnosing Human Diseases. J Clin Diagn Res : JCDR. 2015;10(3):DE01-5.

2. Miserocchi G, Mercatali L, Liverani C, Vita AD, Spadazzi C, Pieri F, et al. Management and potentialities of primary cancer cultures in preclinical and translational studies. J Transl Med. 2017;15(1):229.

3. Tanaka K, Okitsu T, Teramura N, Iijima K, Hayashida O, Teramae H, et al. Recombinant collagenase from Grimontia hollisae as a tissue dissociation enzyme for isolating primary cells. Sci Rep. 2020;10(1):3927.

4. Jabłońska-Trypuć A, Matejczyk M, Rosochacki S. Matrix metalloproteinases (MMPs), the main extracellular matrix (ECM) enzymes in collagen degradation, as a target for anticancer drugs. J Enzym Inhib Med Chem. 2016;31(sup1):177–83.

5. Manka SW, Carafoli F, Visse R, Bihan D, Raynal N, Farndale RW, et al. Structural insights into triple-helical collagen cleavage by matrix metalloproteinase 1. Proc Natl Acad Sci. 2012;109(31):12461–6.

6. Deng SJ, Bickett DM, Mitchell JL, Lambert MH, Blackburn RK, Carter HL, et al. Substrate Specificity of Human Collagenase 3 Assessed Using a Phage-displayed Peptide Library*. J Biol Chem. 2000;275(40):31422–7.

7. Alipour H, Raz A, Zakeri S, Djadid ND. Therapeutic applications of collagenase (metalloproteases): A review. Asian Pac J Trop Biomed. 2016;6(11):975–81.

8. Breite AG, McCarthy RC, Dwulet FE. Characterization and Functional Assessment of Clostridium Histolyticum Class I (C1) Collagenases and the Synergistic Degradation of Native Collagen in Enzyme Mixtures Containing Class II (C2) Collagenase. Transplant Proc. 2011;43(9):3171–5.

9. Tryggvason K, Huhtala P, Tuuttila A, Chow L, Keski-Oja J, Lohi J. Structure and expression of type IV collagenase genes. Cell Differ Dev. 1990;32(3):307–12.

10. Lee SML, Schelcher C, Demmel M, Hauner M, Thasler WE. Isolation of Human Hepatocytes by a Two-step Collagenase Perfusion Procedure. J Vis Exp. 2013;(79).

11. LeCluyse EL, Alexandre E, Hamilton GA, Viollon-Abadie C, Coon DJ, Jolley S, et al. Isolation and culture of primary human hepatocytes. Methods Mol Biol (Clifton, NJ). 2004;290:207–29.

12. Gramignoli R, Green ML, Tahan V, Dorko K, Skvorak KJ, Marongiu F, et al. Development and Application of Purified Tissue Dissociation Enzyme Mixtures for Human Hepatocyte Isolation. Cell Transplant. 2012;21(6):1245–60.

13. Sreejit P, Kumar S, Verma RS. An improved protocol for primary culture of cardiomyocyte from neonatal mice. Vitr Cell Dev Biol - Anim. 2008;44(3):45–50.

14. Santos FAA dos, Carvalho CL, Almeida I, Fagulha T, Rammos F, Barros SC, et al. Simple Method for Establishing Primary Leporidae Skin Fibroblast Cultures. Cells. 2021;10(8):2100.

15. Minafra L, Norata R, Bravatà V, Viola M, Lupo C, Gelfi C, et al. Unmasking epithelial-mesenchymal transition in a breast cancer primary culture: a study report. BMC Res Notes. 2012;5(1):343.

16. Albayrak MGB, Simsek T, Kasap M, Akpinar G, Canturk NZ, Guler SA. Tissue proteome analysis revealed an association between cancer, immune system response, and the idiopathic granulomatous mastitis. Méd Oncol. 2022;39(12):238.

17. Yanar S, Sarihan M, Kasap M, Akpinar G, Teke K, Bayrak BY. GFP Transfection Alters Protein Expression Patterns in Prostate Cancer Cells: A Proteomic Study. J Fluoresc. 2024;1–13.

18. Oseni AO, Butler PE, Seifalian AM. Optimization of chondrocyte isolation and characterization for large-scale cartilage tissue engineering. J Surg Res. 2013;181(1):41–8.

19. Quatromoni JG, Singhal S, Bhojnagarwala P, Hancock WW, Albelda SM, Eruslanov E. An optimized disaggregation method for human lung tumors that preserves the phenotype and function of the immune cells. J Leucoc Biol. 2014;97(1):201–9.

20. Kristó I, Bajusz I, Bajusz C, Borkúti P, Vilmos P. Actin, actin-binding proteins, and actin-related proteins in the nucleus. Histochem Cell Biol. 2016;145(4):373–88.

21. Geiger B, Yamada KM. Molecular Architecture and Function of Matrix Adhesions. Cold Spring Harb Perspect Biol. 2011;3(5):a005033.

22. Hoon JL, Tan MH, Koh CG. The Regulation of Cellular Responses to Mechanical Cues by Rho GTPases. Cells. 2016;5(2):17.

23. Jia D, Lu M, Jung KH, Park JH, Yu L, Onuchic JN, et al. Elucidating cancer metabolic plasticity by coupling gene regulation with metabolic pathways. Proc Natl Acad Sci. 2019;116(9):3909–18.

24. Cardaci S, Ciriolo MR. TCA Cycle Defects and Cancer: When Metabolism Tunes Redox State. Int J Cell Biol. 2012;2012:161837.

Research Article

CHANGES IN SECONDARY STRUCTURE OF PROTEIN IN SKELETAL MUSCLE DUE TO HIGH-CARBOHYDRATE OR HIGH-FAT DIETS

Nazlı EZER ÖZER [1], Ayça DOĞAN MOLLAOĞLU [2*]

[1] Istanbul Medipol University, International School of Medicine, Department of Biophysics, Istanbul, TURKIYE
[2] Altinbas University, Faculty of Medicine, Department of Physiology, Istanbul, TURKIYE
Correspondence: ayca.mollaoglu@altinbas.edu.tr

ABSTRACT

Objective: Obesity, which arises from changes in lifestyle and feeding habits, poses a threat to human health. One essential contributor to the increase in obesity rates is the popularity of high-calorie diets. This study aims to investigate high-fat (HFD) and high-carbohydrate (HCD) diet-induced molecular changes in protein secondary structure in longissimus dorsi skeletal muscle tissues of female inbred C57BL/6J mice by utilizing Attenuated Total Reflectance-Fourier Transform Infrared (ATR-FTIR) spectroscopy.

Materials and Methods: Mice were fed a control diet, HCD, or HFD for 24 weeks. Their skeletal muscle tissues were collected, and their spectra were recorded using a Bruker Invenio S ATR-FTIR spectrometer in the 4000-400 cm^{-1} region.

Results: The protein secondary structure profiles of the HCD group demonstrated a significant rise in antiparallel β-sheet and β-turn and a decline in parallel β-sheets, together with the insignificant increase in aggregated β-sheets and a decrease in α-helix. The impact of an HFD on protein conformation is less pronounced than HCD. The HFD diet led to an increase in antiparallel β-sheets and a decrease in parallel β-sheets. Although insignificant, an increase was observed in β-turn and α-helix.

Conclusion: These results propose the appearance of protein aggregation and/or formation of protein-protein intermolecular interaction in skeletal muscle tissues of female inbred C57BL/6J mice. Collectively, these data suggest that both high-calorie diets impair secondary structures of protein in skeletal muscle that may affect its metabolic function.

Keywords: Obesity, High-carbohydrate diet, High-fat diet, Protein secondary structure, FTIR, Spectroscopy

INTRODUCTION

High-calorie diet consumption results in metabolic complications involving obesity, insulin resistance, type-2 diabetes, and metabolic syndrome that are associated with disruptions in lipid, protein, and carbohydrate metabolism (1). Skeletal muscles are profoundly involved in the modulation of this metabolism and undergo a range of structural and functional alterations in response to impaired insulin function due to ectopic lipid infiltration. This lipid accumulation in skeletal muscles and their intracellular localization is linked to alterations in tissue composition, structure, and remodeling (2). Changes in skeletal muscle macromolecular composition associated with obesity may thus provide insight into the mechanisms behind insulin-related diseases (3). Skeletal muscle not only aids in physical activity by producing mechanical work, but it also helps maintain health by utilizing and storing macronutrients. It uses a large proportion of the amino acids discharged into the circulating system from diets to construct novel functional proteins and is thus the key determinant of glucose and lipid uptake. Furthermore, alterations in the contribution of skeletal muscle to basal and/or subsequent macronutrient metabolism may have a substantial impact on disease threat. Myofibrillar proteins are especially vulnerable to anabolic resistance, and emerging evidence suggests that obesity can also unfavorably influence muscle protein turnover or the breakdown and restoration of functional proteins (3-5). Changes in protein structures and thus functions do not depend solely on modifications to the expression of genes or the production of proteins. To comprehend the functional abnormalities that manifest in various disease states and create new therapeutic strategies, it is crucial to ascertain the structural alterations of proteins and lipids (6). The ability of proteins to perform their duties fully depends on their three-dimensional structure in their natural state (7). Any mistakes that could happen during the folding step cause proteins to reach various secondary, tertiary, or quaternary structures, which results in the related proteins losing their functions or having different activities (8). Therefore, this study aims to elucidate for the first time how high-calorie diets affect the protein secondary structure profile of longissimus dorsi skeletal muscle tissue of inbred C57BL/6J mice using FTIR spectroscopy.

FTIR spectroscopy is a particularly useful method for studying the conformational changes and the secondary structure of proteins (9,10). It is a technique used to analyse the vibrations of functional groups in molecules by exposure to electromagnetic radiation at infrared wavelengths (11). Changes in the vibration of chemical bonds in the infrared region and their absorption properties lead to the formation of spectral peaks. Each of the functional groups has its own frequency of vibration, and each infrared spectrum is specific (12). The many benefits of FTIR include its ability to examine samples at the molecular level without damaging biological systems, straightforward sample preparation procedures, and simultaneously obtain information about all macromolecules in the system (10,13). Since pathological conditions create structural and functional modifications in the biological systems' molecules, these alterations result in changes in vibrational energy levels that can be monitored using FTIR spectroscopy (14). This study will give us an idea of whether high-

calorie diets cause structural changes in protein at the molecular level or not. Hence, it will serve as a guide for researchers conducting current and future human research investigations, as well as contribute to the literature for the diagnosis and treatment of obesity.

MATERIALS AND METHODS

Animals and diets

Four-week-old female inbred C57BL/6J mice were obtained from the Medipol University Mouse House (Istanbul, Turkey) and bred in the facility of Mouse House at Uskudar University for 24 weeks. All animal experiments were confirmed by the Uskudar University Animal Research Local Ethics Committee (approval no. 2017/02). Mice were hosted in groups of five in cages at room temperature ($22 \pm 2°C$) with a 12:12 hour light and dark cycle. During the experiment, the animals had ad libitum access to water and diets. They were divided randomly into three groups, namely the low-fat and low-carbohydrate diet group (control, n = 9), the high-carbohydrate and low-fat diet group (HCD, n = 9), and the high-fat and low-carbohydrate diet group of mice (HFD, n = 5). After weaning at the age of four weeks, all of the mice were given a control diet for a week. After that, high-fat and high-carbohydrate-containing diets were implemented, and this treatment was continued for six months. The control group was fed a low-fat and carbohydrate diet with 25% fat, 20% protein, and 55% carbohydrate (≈ 9% fat by weight) of total calories (S9101-E010, Ssniff Spezialdiäten GmbH, Soest, Germany). The HFD group of mice was given a diet consisting of 45% fat, 20% protein, and 35% carbohydrates (≈ 23% fat by weight) of total calories (S9101-E012, Ssniff Spezialdiäten GmbH, Soest, Germany). Mice in the HCD group were given a diet including 10% of total calories from fat, 20% from protein, and 70% from carbohydrates (≈ 5% fat by weight) (S9101-E014, Ssniff Spezialdiäten GmbH, Soest, Germany). All diets comprise corn starch, maltodextrin, and sucrose as carbohydrates and soybean oil, coconut oil, and tallow as fat. Furthermore, the mineral and vitamin ingredients of the diets were adjusted to meet the requirements of the mice and did not vary between the groups. Animals were weighed every week starting from 4 weeks of age, taking into account their day of birth. All mice were decapitated under anesthesia at the end of 24 weeks, and their skeletal muscle tissues were collected and stored at -80 ºC until further examinations.

Sampling for ATR-FTIR spectroscopy and data analysis

The ATR-FTIR spectra of skeletal muscle tissues were obtained using a Bruker Invenio S ATR-FTIR spectrometer (Germany). The background spectrum was obtained by recording the spectrum of air and automatically subtracted using the Opus 8.5 software program. The muscle samples' spectra were collected at room temperature within the range of 4000-400 cm⁻¹ mid-infrared region with 64 scans at 4 cm⁻¹ resolution. Under the same circumstances, each tissue was scanned three times from randomly chosen fractions, all of which produced identical spectra. The data and statistical analysis were conducted using the average spectra

of these three replicates. The gathering and manipulation of spectral data were obtained by the same software program (Opus 8.5).

Amide I band was taken into consideration to investigate high-calorie diet-induced alterations in the protein secondary structure of muscle tissues. Firstly, the second derivatives of all spectra were collected using a nine-point Savitzky-Golay smoothing filter to eliminate noise, followed by vector normalization in the 1800-1000 cm^{-1} range. The peak minimums of the second derivative spectra, which are equal to the maximums of the original absorption spectra, were used to calculate peak intensities.

Statical analysis

The results of our study were presented as means ∓SEM. The Kruskal-Wallis one-way ANOVA test was applied using GraphPad Prism 8.02 (GraphPad Software, Inc.) to analyze the experimental data. A p-value less than or equal to 0.05 was considered statistically significant, and *p<0.05, **p<0.01, and ***p<0.001 denoted the level of significance.

RESULTS
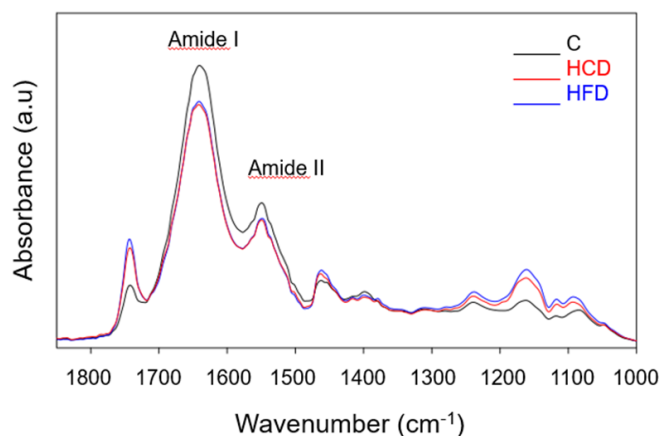
Figure 1. The representative FTIR spectra of skeletal muscles of the HCD, HFD, and control groups in the 1800-1000 cm^{-1} fingerprint region. Baseline offset transforms were performed over the entire spectral range (4000-400 cm^{-1}).

Figure 1 displays the absorbance of skeletal muscle tissues of the control, HCD, and HFD groups in the 1800-1000 cm^{-1} fingerprint region. The bands at 1640 cm^{-1} and 1550 cm^{-1} are assigned to amide I and amide II, which are characteristic vibrations of structural proteins, respectively. The amide I band results from mainly C=O stretching (80%) and C–N stretching vibrations of the protein backbone, and amide II originates from N–H bending (60%) and C–N stretching (40%) vibrations of the proteins, respectively (10). Therefore, the changes in area and/or intensity of these bands refer to changes in the protein structures of samples (12). As seen in Figure 2A, there was a marked decrease in the area ratio of the amide I / amide II bands in the HCD (p<0.05)

and HFD ($p < 0.05$) groups compared to control groups, indicating an alteration in protein structure. In addition, a remarkable decrease in the protein concentration is found only in the HFD ($p<0.05$) groups compared to the control by monitoring the area ratio of the amide I / amide I + amide II bands (Figure 2B).
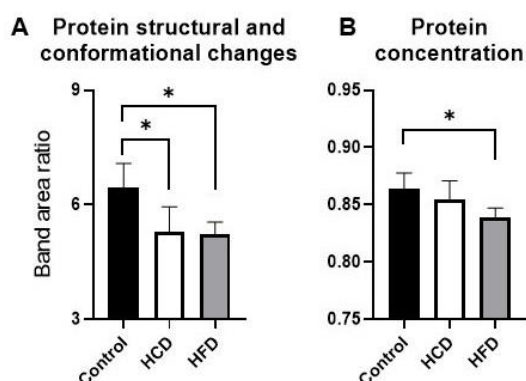
Figure 2. Changes in the band area ratio of (A) protein structural and conformational changes (amide I / amide II), (B) protein content (amide I / amide I + amide II) from the skeletal muscle spectra of the HCD, HFD, and control groups.

Comprehensive information regarding a protein's secondary structure can be determined by analyzing the amide I band (1700-1600 cm^{-1}) using second derivative spectra. Because these spectra reveal sub-bands, which are absent in the original absorbance spectrum (9). Sub-bands in the skeletal muscle tissues' second derivative spectra are observed at 1694, 1680, 1662, 1648, and 1630 cm^{-1}, respectively.
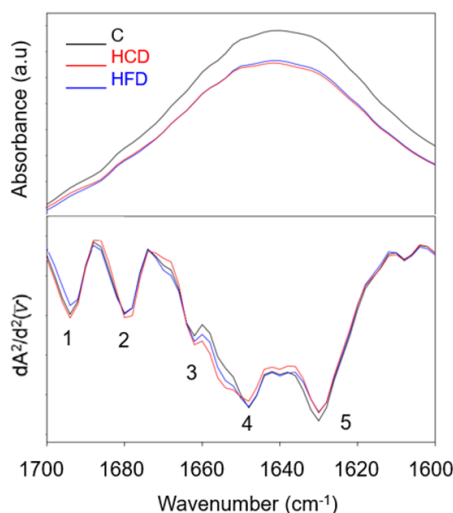
Figure 3. (A) FTIR absorbance spectra and (B) Amide I band second derivative spectra for skeletal muscles of control, HCD, and HFD in the 1700-1600 cm^{-1} region. The second derivative + vector normalization was carried out in the 1700-1600 cm^{-1} range.

Figure 3 displays the average absorbance spectrum (A) and the vector normalized second derivative spectrum (B) containing the sub-bands of the amide I band. The peak located at 1694 cm^{-1} can be attributed to the presence of an antiparallel β-sheet structure [15,16]. The sub-bands at 1680 cm^{-1}, 1662 cm^{-1}, and 1648 cm^{-1} arise from aggregated β-sheet structure [9], β-turn [16,17], and α-helix [16-18]. The band at 1630 cm^{-1} often gives information about parallel β-sheet structure [15].
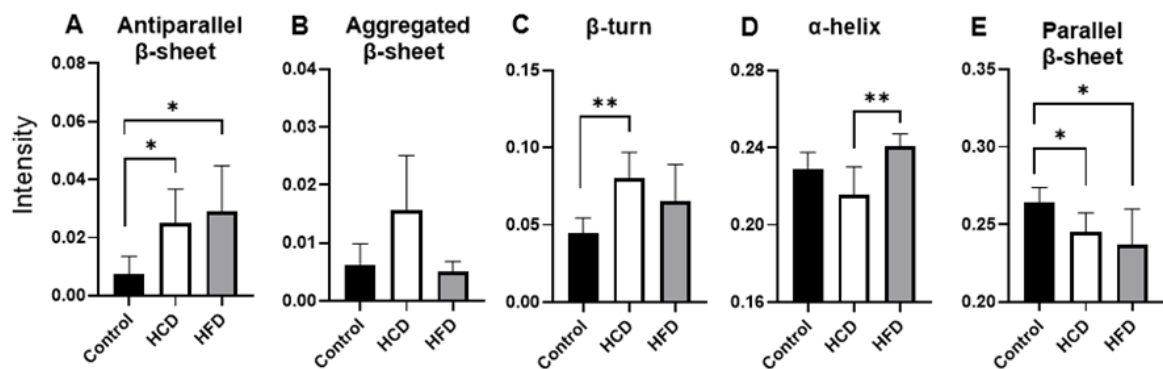
Figure 4. Comparison of the intensities of the main protein secondary structures for (A) antiparallel β-sheet (1694 cm^{-1}), (B) aggregated β-sheet (1680 cm^{-1}), (C) β-turn (1662 cm^{-1}), (D) α-helix (1648 cm^{-1}), and (E) parallel β-sheet (1630 cm^{-1}), for control, HCD, and HFD groups. The level of significance was denoted as *p≤0.05; **p≤0.01.

As depicted in Figure 4, the intensity of the antiparallel β-sheet band (1694 cm^{-1}) increased significantly in the HCD ($p<0.05$) and HFD ($p<0.05$) groups in comparison to the control group. While not statistically significant, the HCD group showed an increased intensity in aggregated β-sheets (1680 cm^{-1}) content. However, in the HFD group, no alteration is found in this content. The intensity of β-turn structure (1662 cm^{-1}) is increased markedly in the HCD group ($p<0.01$), whereas the HFD group demonstrated an insignificant increase in this content compared to the control group. A considerable increase is found in α-helix structure (1648 cm^{-1}) in the HFD group regarding the HCD group. This content insignificantly decreased in the HCD group and slightly increased in the HFD group in contrast with the control group. In addition, β-sheet structure (1632 cm^{-1}) is found to be decreased in both diet groups compared to the control group.

DISCUSSION

The preservation of skeletal muscle mass relies on a fine balance between protein synthesis and breakdown [1] and is affected by diet [19]. Therefore, in the current study, we concentrated on the impact of a high-fat and/or high-carbohydrate diet specifically on the protein secondary structure of skeletal muscle tissue. The area ratio of the main protein bands, amide I / amide I + amide II bands, decreased in HFD groups, indicating that there was a decrease in the protein content of the skeletal muscle. A reduction in protein content may indicate a decrease in protein synthesis. This finding is compatible with the results of previous studies in the literature. Deldicque et al. [20] investigated how endoplasmic reticulum stress caused by a high-fat diet

affects the activity of mTORC1 and protein synthesis in muscle cells. They discovered that a high-fat diet causes the protein unfolding response to be triggered in mouse skeletal muscle while also reducing protein synthesis and mTORC1 activity. Anderson et al. (21) used C57BL/6J mice to test the idea that obesity slows down the activation of tissue-specific protein production following food intake. They showed that a high-fat diet did not change the basal rates of protein synthesis in skeletal muscle, but it did slow down protein synthesis activation and change the way tissue-specific protein metabolism works. It has also been reported that the later stage of obesity development in rats fed with a high-fat, high-sucrose diet is characterized by a decrease in protein synthesis rate and an increase in lipid accumulation in glycolytic muscles (22). Although alterations in protein synthesis are crucial to the diagnosis and therapy of disease, there is insufficient knowledge regarding the links between functional qualities such as the structure and dynamics of lipids and proteins in tissues. Variations in gene expression or protein synthesis are not the sole determinants of structural and functional modifications to proteins. Variations in the secondary structures of proteins that occur without an alteration in their expression can also result in protein malfunction (23). Determining the structural changes in proteins and lipids is essential for better understanding the functional anomalies that arise in different disease states and to facilitate the development of new therapeutics (24).

FTIR spectroscopy is one of the most effective experimental methods for determining protein secondary structure. By taking the second derivative of the FTIR spectra, sub-bands of biomolecules can be visualized. The main bands that represent protein structural and conformational changes are amide I and amide II (9). The amide I absorption band, as opposed to the amide II absorption, is more helpful for determining the protein's secondary structure. This is likely because the amide I band effectively arises from just C=O functional groups of the peptide linkages (16). The α-helix and the β-sheet are two folds that are extremely common in protein secondary structures. From the outside, α-helixes and β-sheets look the same, with the exception that carbonyl oxygens are located on one side of a strand while NH groups are located on the other. This gives α-helixes and β-sheets different physical properties. Both mutations in the primary structure of amino acids that comprise a protein and extraordinary circumstances that cause the proteins to denature can disrupt the protein's secondary structure (25). The results of this study discovered that the muscle protein secondary structure profiles of both HCD and HFD groups are impaired. The HCD feeding significantly increased antiparallel β-sheets and β-turn contents and decreased parallel β-sheets content. Moreover, insignificant increases in aggregated β-sheets and a decrease in α-helix content are observed in this group. It is known that the alpha-helix decreases and the beta-sheet increases in the early phases of diseases like diabetes and neurodegenerative diseases (26). We observed similar facts in the HCD group as described above. However, antiparallel β-sheet structure increased markedly, and parallel β-sheets decreased notably, together with insignificantly increased α-helix and β-turn in the HFD group. These modifications may arise from the expression of novel types of proteins with an alpha-helix structure, or they may result from structural reorganizations of pre-existing proteins. Proteins with β-turns are often associated with highly ordered protein

structures, while those with β-sheets and random coils are characteristic of flexible and open structures (27). The increased β-sheet region is linked to an increase in protein-protein interactions among exposed hydrophobic parts, resulting in intermolecular β-sheet structures (28). Therefore, in the HCD group, increased contents of antiparallel β-sheet and aggregated β-sheet may indicate the formation of cross-β-sheet structure. Furthermore, taking into consideration these results together with the decreased α-helix content, it seems that protein aggregation and/or protein-protein intermolecular interaction may be occurring (29). In the HFD group, the structural alteration is less pronounced since the contents of antiparallel β-sheets, β-turn, and α-helix increased and the content of parallel β-sheets decreased. These findings may imply protein rearrangement and/or the formation of intermolecular β-sheet structures. No alteration is observed in aggregated β-sheet content. An increased α-helix and β-turn together revealed a more ordered protein structure in the intact structure of the myofibril. Because the α-helix is a highly prevalent structural motif within the myosin head (>48%) (30), which is responsible for assembling myosin filaments (31). Furthermore, α-helices frequently participate in molecular recognition and protein interactions with other proteins and nucleic acids (32). Thus, stable α-helical structures are important for the maintenance of protein function. Gurbanov et al. (33) also observed an increase in α-helix structures in the brush border membranes of diabetic kidneys. They proposed that this was a result of an increase in the lipid order of the membrane, particularly elevated levels of trans conformers. These trans conformers lead to an expansion in the rigidity and the width of lipid bilayers, consequently amplifying the α-helix transmembrane protein structure. In another study, type I and IV collagens in the bovine Flexor carpi radialis muscle were examined using FT-IR spectroscopy by Petibois et al. (34). They discovered that the relevant quantity of α-helix and triple helix in type I collagen increases while the amount of β-sheets decreases. Most previous studies were generally conducted on high-calorie diet-induced alterations in metabolism and function of muscle tissue (21,35,36). However, there are few studies in the literature examining the secondary structure of skeletal muscle protein using FTIR spectroscopy, but no studies investigating the effects of different diets have been found. Bozkurt et al. (10) revealed that diabetes causes substantial alterations in protein secondary structures in skeletal muscles due to increased aggregated β-sheet structures. Simsek Ozek et al. (37) also reported that low-dose simvastatin causes alterations in the composition, structure, and dynamics of muscle tissue from the extensor digitorum longus of a rat's skeleton. There is a considerable increase in random coil, antiparallel, and aggregated β-sheet structures as well as a considerable decrease in β-sheet structure, which is a sign of protein denaturation. In simvastatin-treated healthy rat liver tissue, Garip et al. (38) reported a significant decrease in α-helix and a rise in random coil, whereas native β-sheet goes down and aggregated β-sheet goes up, indicating simvastatin-induced protein denaturation. Bozkurt et al. (26) examined rat liver proteins' structural changes caused by streptozotocin-induced diabetes and found substantial variations in proteins' secondary structure, including a decrease in the proportion of α-helixes and an increase in the amount of β-sheets, which resulted in protein denaturation and aggregation in the liver of diabetics.

CONCLUSION

As far as we know, this is the first study demonstrating the HCD and HFD effects on the secondary structure of skeletal muscle protein using ATR-FTIR spectroscopy. The findings of the present investigation revealed that protein conformations were affected differently depending on the type of diet. The HCD diet was found to be more detrimental. Elaborated secondary structure analysis of the amide I band revealed the occurrence of intermolecular β-sheet structures and/or protein aggregation in the HCD group, while the HFD group showed structural reorganizations of proteins and/or the formation of intermolecular β-sheet structures. These kinds of structural alterations are critical because any change in protein structure results in alterations in the protein function. In the current study, ATR-FTIR spectroscopy was provided to be a very suitable technique for detecting the secondary structure profile of proteins in muscle tissue.

Authorship contributions
Concept: A.D, Design: A.D, Data Collection and Processing: N.E.O, Analysis or Interpretation: N.E.O, A.D, Literature Search: N.E.O, A.D, Writing: N.E.O, A.D

Data availibity statement
The datasets utilized and/or examined during the present investigation can be obtained from the corresponding author upon a reasonable request.

Declaration of competing interest
The authors have no conflicts of interest to declare.

Ethics
The experimental protocol of this study was approved by the Uskudar University Animal Research Local Ethics Committee (Approval No: 2017/02).

REFERENCES

1. Sartori R, Romanello V, Sandri M. Mechanisms of muscle atrophy and hypertrophy: implications in health and disease. Nat Commun 2021; 12(1): 330.

2. Bergman BC, Goodpaster BH. Exercise and Muscle Lipid Content, Composition, and Localization: Influence on Muscle Insulin Sensitivity. Diabetes 2020; 69(5): 848-58.

3. Sen I, Bozkurt O, Aras E, Heise S, Brockmann GA, Severcan F. Lipid Profiles of Adipose and Muscle Tissues in Mouse Models of Juvenile Onset of Obesity without High Fat Diet Induction: A Fourier Transform Infrared (FT-IR) Spectroscopic Study. Appl Spectrosc 2015; 69(6): 679-88.

4. Beals JW, Burd NA, Moore DR, Van Vliet S. Obesity alters the muscle protein synthetic response to nutrition and exercise. Front Nutr 2019; 6: 87.

5. Dideriksen K, Reitelseder S, Holm L. Influence of amino acids, dietary protein, and physical activity on muscle mass development in humans. Nutrients 2013; 5(3): 852-76.

6. Marinko JT, Huang H, Penn WD, Capra JA, Schlebach JP, Sanders CR. Folding and Misfolding of Human Membrane Proteins in Health and Disease: From Single Molecules to Cellular Proteostasis. Chem Rev 2019; 119(9): 5537-606.

7. Anfinsen CB. Principles that govern the folding of protein chains. Science 1973; 181(4096): 223-30.

8. Stollar EJ, Smith DP. Uncovering protein structure. Essays Biochem 2020; 64(4): 649-80. Erratum in: Essays Biochem 2021; 65(2): 407.

9. Severcan F, Haris PI. Fourier transform infrared spectroscopy suggests unfolding of loop structures precedes complete unfolding of pig citrate synthase. Biopolymers 2003; 69(4): 440-47.

10. Bozkurt O, Severcan M, Severcan F. Diabetes induces compositional, structural and functional alterations on rat skeletal soleus muscle revealed by FTIR spectroscopy: a comparative study with EDL muscle. The Analyst 2010; 135(12): 3110.

11. Garip S, Gozen AC, Severcan F. Use of Fourier transform infrared spectroscopy for rapid comparative analysis of Bacillus and Micrococcus isolates. Food Chem 2009; 113(4):1301-07.

12. Cakmak G, Togan I, Severcan F. 17β-Estradiol induced compositional, structural and functional changes in rainbow trout liver, revealed by FT-IR spectroscopy: A comparative study with nonylphenol. Aquat Toxicol 2006; 77(1): 53-63.

13. Ezer N, Sahin I, Kazanci N. Alliin interacts with DMPC model membranes to modify the membrane dynamics: FTIR and DSC Studies. Vib Spectrosc 2017; 89: 1-8.

14. Mollaoğlu AD, Gurbanov R, Severcan M, Severcan F. CoronaVac (Sinovac) COVID-19 vaccine-induced molecular changes in healthy human serum by infrared spectroscopy coupled with chemometrics. Turk J Biol 2021; 45(7): 569-77.

15. Miller LM, Bourassa MW, Smith RJ. FTIR spectroscopic imaging of protein aggregation in living cells. Biochim Biophys Acta 2013; 1828(10): 2339-46.

16. Barth A. Infrared spectroscopy of proteins. Biochim Biophys Acta 2007; 1767(9): 1073-101.

17. Krimm S, Bandekar J. Vibrational spectroscopy and conformation of peptides, polypeptides, and proteins. Adv Protein Chem 1986; 38: 181-364.

18. Toyran N, Zorlu F, Severcan F. Effect of stereotactic radiosurgery on lipids and proteins of normal and hypoperfused rat brain homogenates: a Fourier transform infrared spectroscopy study. Int J Radiat Biol 2005; 81(12): 911-18.

19. Mithal A, Bonjour J-P, Boonen S, Burckhardt P, Degens H, El Hajj Fuleihan G, et al. Impact of nutrition on muscle mass, strength, and performance in older adults [published correction appears in Osteoporos Int 2013; 24(4): 1527-8]. Osteoporos Int 2013; 24(5): 1555-66.

20. Deldicque L, Cani PD, Philp A, Raymackers J-M, Meakin PJ, Ashford MLJ, et al. The unfolded protein response is activated in skeletal muscle by high-fat feeding: potential role in the downregulation of protein synthesis. Am J Physiol-Endocrinol Metab 2010; 299(5): 695-705.

21. Anderson SR, Gilge DA, Steiber AL, Previs SF. Diet-induced obesity alters protein synthesis: tissue-specific effects in fasted versus fed mice. Metabolism 2008; 57(3): 347-54.

22. Masgrau A, Mishellany-Dutour A, Murakami H, Beaufrère A-M, Walrand S, Giraudet C, et al. Time-course changes of muscle protein synthesis associated with obesity-induced lipotoxicity. J Physiol 2012; 590(20): 5199-210.

23. Vihinen, M. Functional effects of protein variants. Biochimie 2021; 180: 104-20.

24. Collin F, Cerlati O, Couderc F, Lonetti B, Marty J-D, Mingotaud A-F. Multidisciplinary analysis of protein-lipid interactions and implications in neurodegenerative disorders. Trends Anal Chem 2020; 132: 116059.

25. Shea D, Hsu CC, Bi TM, Paranjapye N, Childers MC, Cochran J, et al. α-Sheet secondary structure in amyloid β-peptide drives aggregation and toxicity in Alzheimer's disease. Proc Natl Acad Sci USA 2019; 116(18): 8895-900.

26. Bozkurt O, Haman Bayari S, Severcan M, Krafft C, Popp J, Severcan F. Structural alterations in rat liver proteins due to streptozotocin-induced diabetes and the recovery effect of selenium: Fourier transform infrared microspectroscopy and neural network study. J Biomed Opt 2012; 17(7): 0760231.

27. Siddique MAB, Maresca P, Pataro G, Ferrari G. Effect of pulsed light treatment on structural and functional properties of whey protein isolate. Food Res Int 2016; 87:189-96.

28. Harnkarnsujarit N, Kawai K, Suzuki T. Effects of Freezing Temperature and Water Activity on Microstructure, Color, and Protein Conformation of Freeze-Dried Bluefin Tuna (*Thunnus orientalis*). Food Bioprocess Technol. 2015; 8: 916-25.

29. Wachirattanapongmetee K, Katekaew S, Weerapreeyakul N, Thawornchinsombut S. Differentiation of protein types extracted from tilapia byproducts by FTIR spectroscopy combined with chemometric analysis and their antioxidant protein hydrolysates. Food Chem 2024; 437(2): 137862.

30. Xiong YL. Structure function relationships of muscle proteins. In: Damodaran S, Paraf A, editors. Food Proteins and Their Applications. Marcel Dekker Inc, 1997: 341-92.

31. Rayment I, Rypniewski WR, Schmidt-Bäse K, Smith R, Tomchick D, Benning M, et al. Three-dimensional structure of myosin subfragment-1: a molecular motor. Science 1993; 261(5117): 50-8.

32. Mahon AB, Arora PS. End-Capped α-Helices as Modulators of Protein Function. Drug Discov Today Technol 2012; 9(1):57-62.

33. Gurbanov R, Bilgin M, Severcan F. Restoring effect of selenium on the molecular content, structure and fluidity of diabetic rat kidney brush border cell membrane. Biochim Biophys Acta-Biomembr 2016; 1858(4): 845-54.

34. Petibois C, Gouspillou G, Wehbe K, Delage J-P, Déléris G. Analysis of type I and IV collagens by FT-IR spectroscopy and imaging for a molecular investigation of skeletal muscle connective tissue. Anal Bioanal Chem 2006; 386: 1961-66.

35. Sitnick M, Bodine SC, Rutledge JC. Chronic high fat feeding attenuates load-induced hypertrophy in mice. J Physiol 2009; 587(23): 5753-65.

36. Antunes MM, Godoy G, de Almeida-Souza CB, da Rocha BA, da Silva-Santi LG, Masi LN, et al. A high-carbohydrate diet induces greater inflammation than a high-fat diet in mouse skeletal muscle. Braz J Med Biol Res 2020; 53(3): 9039.

37. Simsek Ozek N, Sara Y, Onur R, Severcan F. Low dose simvastatin induces compositional, structural and dynamic changes in rat skeletal extensor digitorum longus muscle tissue. Biosci Rep 2009; 30(1): 41-50.

38. Garip S, Bayari SH, Severcan M, Abbas S, Lednev IK, Severcan F. Structural effects of simvastatin on rat liver tissue: Fourier transform infrared and Raman microspectroscopic studies. J Biomed Opt 2016; 21(2): 025008.

SYSTEMIC IMMUNE INFLAMMATION INDEX AND PAN-IMMUNE INFLAMMATION VALUE IN PREDICTING HUMAN LEUKOCYTE ANTIGEN-B27 POSITIVITY: A STUDY ON ANKYLOSING SPONDYLITIS PATIENTS

Adem KESKİN [1, *]**, Taner KARAKAYA** [2]**, Recai ACI** [3]**, Özlem SEZER** [4]**, Samet SEMİZ** [2]**, Ferhat ŞİRİNYILDIZ** [6]**, İpek OKUTAN** [7]

[1] Department of Biochemistry, Institute of Health Sciences, Aydın Adnan Menderes University, Aydin, TURKIYE
[2] Department of Medical Genetics, Samsun Education and Research Hospital, Samsun, TURKIYE
[3] Department of Medical Services and Techniques, Söke Health Services Vocational School, Aydın Adnan Menderes University, Aydin, TURKIYE
[4] Department of Medical Genetics, Faculty of Medicine, Samsun University, Samsun, TURKIYE
[5] Department of Physiology, Faculty of Medicine, Aydin Adnan Menderes University, Aydin, TURKIYE
[6] Department of Physical Medicine and Rehabilitation, Faculty of Medicine, Samsun University, Samsun, TURKIYE
Correspondence: adem.keskin@adu.edu.tr

ABSTRACT

Objective: Ankylosing spondylitis (AS) is defined as both an auto-immune and autoinflammatory illness. Human leukocyte antigen B27 (HLA-B27), which is extensively employed in the diagnosis of chronic inflammatory diseases, is the basic laboratory parameter of axial spondylarthritis including AS. Systemic immune-inflammation index (SII) and pan-immune-inflammation value (PIV), obtained by formulating complete blood count parameters, are promising biomarkers that reflect systemic inflammation and local immune response and predict prognosis in diseases. The aim of this study was to investigate the sensitivity and specificity of SII and PIV biomarkers in predicting HLA-B27 positivity in AS patients.

Materials and Methods: The research included 68 individuals with HLA-B27 tests (+) (AS group) and 102 patients with HLA-B27 tests (-) (control group).

Results: In the AS group, lymphocyte and mean platelet volume values were determined to be lower than in the control group, while other complete blood count parameters, erythrocyte sedimentation rate (ESR) and C-reactive protein (CRP) were found to be higher. While the SII and PIV values of the AS group determined a positive relation with CRP and ESR levels, they did not show a correlation in the control group. While the sensitivity for PIV in predicting HLA-B27 positivity was found to be 83.80% and the specificity was found to be 84.30%, for SII the sensitivity was found to be 83.80% and the specificity was found to be 86.30%.

Conclusion: Easily and rapidly accessible biomarkers SII and PIV can potentially be used to predict HLA-B27 positivity in AS patients.

Keywords: PIV, Ankylosing Spondylitis, SII, Human leukocyte antigen-b27

INTRODUCTION

Ankylosing Spondylitis (AS) is a chronic inflammation autoimmune illness of unknown pathophysiology that principally influences the spine, peripheral joints, and sacroiliac joints. The etiology of AS is thought to be influenced by several factors including immunity, environment, infection and genetics (1). On the one hand, immune pathways such as inflammasome activation, autophagy and ubiquitination play a role in both adaptive and innate immunity in AS, while on the other hand, the presence of an autoimmune response in AS and the accompanying production of specific autoantibodies is an increasingly common concept. Thus, both autoimmune and autoinflammatory factors are involved in the pathogenesis of AS on a continuum (2). Knowing the molecular and cellular processes that underlie the pathophysiology of AS, an inflammation arthritis that influences the spine and is related with both skeletal and immune system disorders, will provide a foundation for investigating potential new treatments for AS (3).

Human leukocyte antigen B27 (HLA-B27), which is related with prolonged inflammation illness, is largely used for diagnosis reasons in these illnesses (4). HLA-B27 prevalence, which is also the basic laboratory parameter of axial spondylarthritis, an inflammatory and immune-mediated disease, varies by geographic region and ethnicity and generally reflects the prevalence of axial spondylarthritis. HLA-B27, which has a significant impact in the pathophysiology of axial spondylarthritis and many referral strategies, is associated with a spondylarthritis phenotype with consistent positive associations with family histories, earlier illness onset, hip involvement, acute anterior uveitis, and shorter diagnosis delay (5). HLA-B27 is a genetic biomarker strongly related with all axial spondylarthritis, from non-radiographic axial spondylarthritis to AS, also known as radiographic axial spondylarthritis, and its absence causes diagnostic delay. The pathophysiology of the condition is poorly understood in HLA-B27 (-) patients, and signs and symptoms are frequently overlooked or misdiagnosed, delaying diagnosis and treatment (6).

The pan-immune-inflammation value (PIV), obtained by formulating complete blood count data, is a promising biomarker for predicting course of illness in pediatric diseases related with immune anomalies and various types of tumors. It also serves as a valuable biomarker to differentiate patients from healthy individuals and to distinguish between remission and active periods in rheumatoid arthritis, a persistent auto-immune illness that causes systemic inflammation (7). Furthermore, a study analyzing 20 years of data reported that PIV is a value to evaluate inflammation and immunity, that inflammation and immunity affect the prognosis of hypertensive people, and that high PIV is corelated with cardiovascular mortality and increased all-cause mortality in hypertensive people (8). On the other hand, the systemic immune-inflammation index (SII), based on platelet, lymphocyte and neutrophil counts, is considered a good value reflecting the systemic inflammation and local immune response (9). Furthermore, a study examining data from a cohort of 40,937 individuals reported that SII is one of the newer measures used to quantify an

individual's systemic inflammatory activity and that there is a significant relation between SII, and the prevalence and mortality of chronic kidney disease linked by immunity and inflammation (10).

The aim of this research was to appraise whether PIV and SII index could predict HLA-B27 positivity in AS people, especially in case of HLA-B27 positivity. Also, to investigate the sensitivity, specificity and cut-off point of these two immune-inflammatory markers in HLA-B27 positivity in AS people.

MATERIALS AND METHODS

Study design

The ethics committee decision for the research was taken at the Samsun University Non-Interventional Clinical Ethics Committee meeting held on February 28, 2024. (Protocol code: GOKAEK 2024/5/5). The principles outlined in the Helsinki Declaration, revised in 2013, were followed throughout the study. Patients who applied to Samsun University Faculty of Medicine Samsun Research and Training Hospital Medical Genetics Polyclinic for HLA-B27 testing between January 01, 2023, and December 31, 2023, and were pre-diagnosed with AS were scanned from the hospital information management system (HIMS). Patients with comorbidities such as cancer, diabetes, chronic kidney diseases and other autoimmune diseases were excluded from the research. In addition to the HLA-B27 test, those who underwent complete blood count, erythrocyte sedimentation rate (ESR) and C-reactive protein (CRP) analysis were included in the research. Complete blood count data (lymphocyte, neutrophil, monocyte, platelet, WBC (white blood cell), MCV (mean corpuscular volume), RDW (red blood cell distribution width) and MPV (mean platelet volume)), ESR and CRP results of the individuals included in the research were obtained from HIMS. Additionally, the PLR (platelet/lymphocyte ratio), MLR (monocyte/lymphocyte ratio) and NLR (neutrophil/lymphocyte ratio) values of these individuals were calculated and included in the research. Additionally, the SII indexes of the individuals were calculated using the formula neutrophil count×platelet count/lymphocyte count (11). PIV indices of the patients were calculated using the formula monocyte count×platelet count×neutrophil count/lymphocyte count (12).

Laboratory analyses

Whole blood parameters were studied using Sysmex XN 1000 (Sysmex Turkey Diagnostic Systems Limited Company, Sarıyer, Istanbul, Turkey), CRP analysis was performed using Beckman Coulter AU5800 Biochemistry autoanalyzer (Beckman Coulter Life Sciences, Indiana, USA) and ESR analysis was performed using ALS-100 PLUS (Alaris Medical and Laboratory Products Industry and Trade Limited Company, Bornova, Izmir, Turkey). HLA B27 test was performed using HLA B27 REAL TIME PCR KIT WITH DNA ISOLATION (SNP Biotechnology, Çankaya, Ankara, Turkey) (Catalog No: 501R-10-02) on a Bio-Rad CFX96 device (Bio Rad Laboratories, Dubai, United Arab Emirates).

Statistical analyses

IBM SPSS Statistics 22.0 program was used for statistical data analyses. The normal distribution properties of age and laboratory findings were evaluated using the Shapiro-Wilk test and skewness and kurtosis statistics. Since the findings did not show a normal distribution, they were shown as median and interquartile range (25th and 75th percentiles). In addition, comparisons between groups and subgroups were compared using a nonparametric test (Mann Whitney U test). P values less than 0.05 were found to be statistically important. Spearman correlation analysis was performed between SII and PIV parameters and CRP and ESR parameters. In addition, Receiver Operating Characteristics (ROC) analysis was performed to see the specificity and sensitivity of SII and PIV parameters in HLA-B27 positivity.

RESULTS

HLA-B27 testing was performed on 588 patients between 01/01/2023 and 12/31/2023. Of these patients whose HLA-B27 test was analyzed, 68 (11.56%) were found to have positive HLA-B27 test results. Patients with positive HLA-B27 tests were defined as the AS group. To ensure that the study was not influenced by age and gender factors, the selection criteria for the control group included an average age and gender ratio similar to the AS group. Considering the average age and gender ratio of the AS group, a group of 102 patients randomly selected from among patients with negative HLA-B27 test and preliminary diagnosis of AS was defined as the control group.

Table 1. Laboratory findings of ankylosing spondylitis and control groups

Parameter	Control n=102	AS n=68	p
WBC (*10⁹/L)	7.16 (5.14-8.03)	8.52 (7.06-10.08	<0.001
Neutrophil (*10⁹/L)	3.78 (3.01-4.41)	7.42 (5.71-9.04)	<0.001
Lymphocyte (*10⁹/L)	2.20 (1.76-2.61)	1.32 (1.06-1.77)	<0.001
Monocyte (*10⁹/L)	0.50 (0.36-0.56)	0.77 (0.54-0.99)	<0.001
Platelet (*10⁹/L)	248.00 (228.75-294.00)	320.00 (252.50-355.00)	<0.001
NLR	1.66 (1.46-2.02)	5.72 (3.24-8.53)	<0.001
MLR	0.22 (0.18-0.27)	0.58 (0.31-0.93)	<0.001
PLR	124.67 (89.09-165.65)	243.39 (143.06-334.91)	<0.001
MCV	85.20 (81.40-89.10)	86.10 (79.93-89.58)	>0.05
MPV	10.30 (9.60-10.90)	9.69 (8.62-10.50)	<0.001
RDV	12.50 (12.00-13.50)	13.60 (13.03-15.10)	<0.001
ESR (mm/h)	9.00 (6.00-11.00)	31.50 (26.25-38.75)	<0.001
CRP (mg/L)	2.56 (1.25-3.40)	15.10 (10.78-22.25)	<0.001
SII	467.95 (347.17-529.68)	1834.33 (816.93-3025.88)	<0.001
PIV	215.81 (144.47-267.87)	1412.44 (443.22-2980.56)	<0.001

Abbreviations: WBC: White blood cell, NLR: neutrophil/lymphocyte ratio, MLR: monocyte/lymphocyte ratio, PLR: Platelet/lymphocyte ratio, MCV: Mean corpuscular volüme, MPV: Mean platelet volume, RDW: Red cell distribution width, CRP: C-reactive protein, ESR: Erythrocyte sedimentation ratio, SII: Systemic Immune Inflammation Index, PIV: Pan-immune-inflammation value

The median age of the individuals in the AS group was 31.00 (26.00-37.25) years, while the median age of the individuals in the control group was 32.50 (27.00-39.75) years. Of the individuals in the AS group, 31 (45.59%) were female and 37 (54.41%) were male. Of the individuals in the control group, 46 (45.09%) were female and 56 (54.90%) were male. There was no important difference in median age and gender ratio between the two groups. The laboratory results of the two groups are presented in Table 1.

In the AS group, WBC, neutrophil, monocyte, platelet, NLR, MLR, PLR, RDV, ESR, CRP, SII and PIV values were determined to be higher than in the control group. Lymphocyte and MPV values were determined to be lower in the AS group than in the control group (Table 1). Correlation analysis was carried out to see the relation between SII and PIV parameters and CRP and ESR parameters. SII values of AS group showed positive correlation with CRP (Correlation coefficient (Cc): 0.990 $p<0.001$) and ESR (Cc: 0.790, $p<0.001$) levels, while they did not show correlation in the control group.
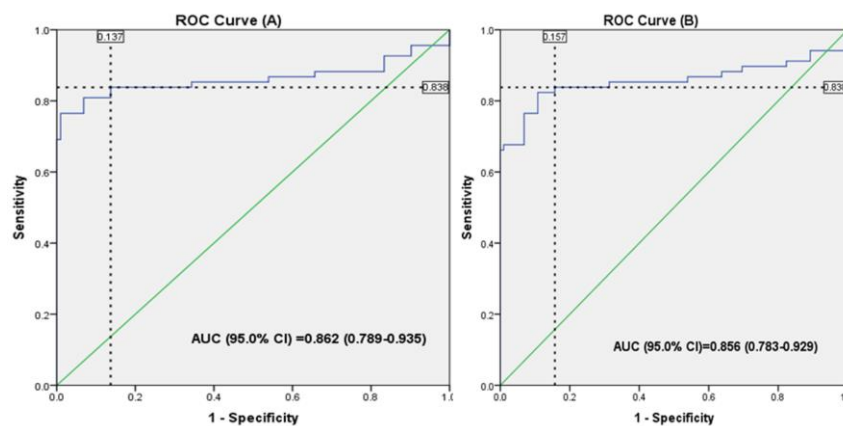
Figure 1. ROC curve graph of SII and PIV

Similarly, PIV values of AS group showed positive correlation with CRP (Cc: 0.990, $p<0.001$) and ESR (Cc: 0.791, $p<0.001$) levels, while they did not show correlation in the control group. ROC analysis was performed to see the specificity and sensitivity of PIV and SII values in HLA-B27 positivity. The results of the analysis are shown in Table 2 and Figure 1. For the prediction of HLA-B27 positivity/negativity, sensitivity for PIV was 83.80% and specificity was 84.30%, while sensitivity for SII was 83.80% and specificity was 86.30% (Table 2 and Figure 1).

Table 2. Results of ROC curve analysis of PIV and SII index in predicting active period of ankylosing spondylitis and HLA-B27 positivity

	Index	AUC (95.0% CI)	p	Cutoff
HLA-B27 positivity	PIV	0.856 (0.783-0.929)	<0.001	282.98
	SII	0.862 (0.789-0.935)	<0.001	561.78

HLA-B27: Human Leukocyte Antigen-B27, AUC: Area under the curve, CI: Confidence interval, SII: Systemic Immune Inflammation Index, PIV: Pan-immune-inflammation value

DISCUSSION

The association between HLA-B27 positivity, which is seen in approximately 8% of the Central European population, and AS was discovered 50 years ago. Approximately 60-90% of individuals with axial spondylarthritis, including AS, worldwide are HLA B27 (+) individuals. The illness prevalence is related to the HLA-B27 frequency in the public. HLA-B27 is also a significant player in the diagnosis, classification and severity of axial spondylarthritis. In an effort to understand the pathophysiology of AS, the arthritogenic peptide hypothesis postulates a strong relationship between HLA-B27 positive and AS etiology (13). The generally accepted function of HLA-B27 is to initiate adaptive immunological responses by presenting antigenic peptides to CD8 cells. According to this theory, HLA-B27 exposes CD8 cells to peptides originating from exogenous sources, such bacteria. These lymphocytes subsequently react with antigens at the site of disease inflammation, resulting in inflammation (14). In a recent research conducted in southeastern of Turkey, the HLA-B27 prevalence was determined to be 20.16% and it was reported that this high prevalence may be related to consanguineous marriage and that HLA-B27 has a predictive role in the diagnosis and prognosis of AS (15).

In this study conducted in the north of Turkey, the HLA-B27 prevalence was determined as 11.56%. It was also found that the immune-inflammatory markers of HLA-B27 (+) individuals were higher than the values of HLA-B27 (-) individuals. In a recent study of 446 AS patients, it was reported that CRP and ESR levels were detected at high levels. It was also reported that ankylosing spondylitis illness activity score was positively correlated with CRP and ESR levels (16). Another recent study reported that those with an AS disease activity score above 4 had higher ESR and CRP levels than those below 4 (17). A study conducted with AS individuals with long-term illness reported that radiographic progression during cure was importantly related with higher time-averaged CRP values (18). Similarly, ESR levels of AS patients were found to be strongly associated with AS Quality of Life, Bath AS Illness Activity Index (BASDAI), AS Illness Activity Score (ASDAS) and Bath AS Functional Index, night pain, morning stiffness, total pain intensity and fatigue (19).

In this study, both CRP and ESR were higher in HLA-B27 (+) individuals than in HLA-B27 (-) individuals. In addition, ESR and CRP levels were associated with PIV and SII values in HLA-B27 (+) individuals, but no association was found in HLA-B27 (-) individuals.

In the recent Spondylo Arthritis International Society (ASAS)-EULAR study, which includes recommendations for AS patients, the ASDAS emerged as the most appropriate tool to assess disease activity and has been recommended for the follow-up of AS patients. Calculated preferably using CRP, ASDAS is a well-balanced score in contrast to the historically more widely used BASDAI. In addition to including CRP as a quantitative indicator of inflammation, it has been validated with the rapid quantitative CRP test, further increasing its applicability for routine clinical work. Specific cut-off values for ASDAS have been validated to define illness activity states and criteria for enhancement and deterioration (20). The cut-off values currently used by rheumatologists to escalate treatment are ASDAS ≥ 2.1 compared to BASDAI ≥ 4 for axial spondylarthritis (21). In this study, HLA-B27 positivity was determined as 282.98 for PIV value and 561.78 for SII index.

Since this study is a retrospective study, the fact that it does not include clinical findings of the patients other than CRP and ESR can be considered as a limitation of the study. On the other hand, this study is a reference for future studies in which clinical findings and organ involvements will be evaluated by establishing one-to-one communication with the patients. In addition, although it is known that HLA-B27 is an important laboratory parameter in AS patients, it is not applicable in every health institution and clinic and it has practical difficulties such as obtaining results late compared to other tests. On the other hand, providing easy and fast access to SII and PIV parameters obtained from routine tests such as complete blood count is an important factor that increases the value of this study in clinical practice. Evaluating the ability of parameters such as SII and PIV to predict HLA-B27 positivity may improve early decision-making processes in AS patients.

CONCLUSION

The values of immune-inflammatory parameters such as SII and PIV were higher in HLA-B27 (+) individuals compared to HLA-B27 (-) individuals. SII and PIV levels were related with ESR and CRP levels in HLA-B27 (+) individuals, but not in HLA-B27 (-) individuals. The cut-off value for SII in HLA-B27 positivity was 561.78 and for PIV was 282.98. In conclusion, immune-inflammatory markers such as SII and PIV can be evaluated in the prediction of HLA-B27 positivity in AS.

Authorship contributions

AK, TK, RA and FS formed the study concept and design, TK, RA, SS and ÖS contributed to the acquisition of the data, AK, ÖS and SS performed analysis and interpretation of the data, AK, FS, RA and SS contributed to the drafting of the manuscript, critical revision of the manuscript for important intellectual content, AK and FS provided statistical expertise.

Data availibity statement

Data supporting the findings of this study are available from the corresponding author upon reasonable request.

Declaration of competing interest

All authors declare that they have no conflict of interest.

Ethics

The ethics committee decision for the research was taken at the Samsun University Non-Interventional Clinical Ethics Committee meeting held on February 28, 2024. (Protocol code: GOKAEK 2024/5/5).

REFERENCES

1. Yang H, Chen Y, Xu W, Shao M, Deng J, Xu S, et al. Epigenetics of ankylosing spondylitis: Recent developments. Int J Rheum Dis. 2021 Apr;24(4):487-493.

2. Mauro D, Thomas R, Guggino G, Lories R, Brown MA, Ciccia F. Ankylosing spondylitis: an autoimmune or autoinflammatory disease? Nat Rev Rheumatol. 2021 Jul;17(7):387-404.

3. Liu L, Yuan Y, Zhang S, Xu J, Zou J. Osteoimmunological insights into the pathogenesis of ankylosing spondylitis. J Cell Physiol. 2021 Sep;236(9):6090-6100.

4. Waeckel L, Kennel A, Berger AE, Lambert C. Human leukocyte antigen-B27 typing by flow cytometry: Comparison of three CE-IVD methods. Cytometry B Clin Cytom. 2023 Nov;104(6):460-467.

5. Fahed H, Mauro D, Ciccia F, Ziade NR. What Does Human Leukocyte Antigen B27 Have to Do with Spondyloarthritis? Rheum Dis Clin North Am. 2020 May;46(2):225-239.

6. Deodhar A, Gill T, Magrey M. Human Leukocyte Antigen B27-Negative Axial Spondyloarthritis: What Do We Know? ACR Open Rheumatol. 2023 Jul;5(7):333-344.

7. Tutan D, Doğan AG. Pan-Immune-Inflammation Index as a Biomarker for Rheumatoid Arthritis Progression and Diagnosis. Cureus. 2023 Oct 6;15(10):e46609.

8. Wu B, Zhang C, Lin S, Zhang Y, Ding S, Song W. The relationship between the pan-immune-inflammation value and long-term prognoses in patients with hypertension: National Health and Nutrition Examination Study, 1999-2018. Front Cardiovasc Med. 2023 Mar 2;10:1099427.

9. Huang H, Liu Q, Zhu L, Zhang Y, Lu X, Wu Y, Liu L. Prognostic Value of Preoperative Systemic Immune-Inflammation Index in Patients with Cervical Cancer. Sci Rep. 2019 Mar 1;9(1):3284.

10. Huang P, Mai Y, Zhao J, Yi Y, Wen Y. Association of systemic immune-inflammation index and systemic inflammation response index with chronic kidney disease: observational study of 40,937 adults. Inflamm Res. 2024 Apr;73(4):655-667.

11. Li G, Yu J, Jiang S, Wu K, Xu Y, Lu X, et al. Systemic Immune-Inflammation Index Was Significantly Associated with All-Cause and Cardiovascular-Specific Mortalities in Patients Receiving Peritoneal Dialysis. J Inflamm Res. 2023 Aug 31;16:3871-3878.

12. Lin F, Zhang LP, Xie SY, Huang HY, Chen XY, Jiang TC, Guo L, Lin HX. Pan-Immune-Inflammation Value: A New Prognostic Index in Operative Breast Cancer. Front Oncol. 2022 Apr 13;12:830138.

13. Braun J, Sieper J. Fifty years after the discovery of the association of HLA B27 with ankylosing spondylitis. RMD Open. 2023 Aug;9(3):e003102.

14. Garrido-Mesa J, Brown MA. T cell Repertoire Profiling and the Mechanism by which HLA-B27 Causes Ankylosing Spondylitis. Curr Rheumatol Rep. 2022 Dec;24(12):398-410.

15. Oral D, Erdal GG, Tekeş S, Yücel I, Em S. Prevalence of HLA B27 in Patients Diagnosed with Ankylosing Spondylitis (AS) in Diyarbakır, Southeastern Region of Turkey. Niger J Clin Pract. 2024 Jan 1;27(1):29-34. doi: 10.4103/njcp.njcp_258_23. Epub 2024 Feb 5. PMID: 38317032.

16. Cui R, Wang YL, Tao YL, Tong Q, Chen Z, Dai SM. Platelet to albumin ratio is an independent indicator for disease activity in ankylosing spondylitis. Clin Rheumatol. 2023 Feb;42(2):407-413.

17. Uzeli Şen U, Başaran PO. Pan-immune inflammation value as a biomarker in ankylosing spondilitis and associated with disease activity. Anatolian Curr Med J. 2024;6(1):48-54

18. Konsta M, Sakellariou GT, Rusman T, Sfikakis PP, Iliopoulos A, van der Horst-Bruinsma IE. Long-term effect of TNF inhibitors on radiographic progression in ankylosing spondylitis is associated with time-averaged CRP levels. Joint Bone Spine. 2021 May;88(3):105111.

19. Yılmaz O, Tutoğlu A, Garip Y, Ozcan E, Bodur H. Health-related quality of life in Turkish patients with ankylosing spondylitis: impact of peripheral involvement on quality of life in terms of disease activity, functional status, severity of pain, and social and emotional functioning. Rheumatol Int. 2013 May;33(5):1159-63.

20. Ramiro S, Nikiphorou E, Sepriano A, Ortolan A, Webers C, Baraliakos X, et al. ASAS-EULAR recommendations for the management of axial spondyloarthritis: 2022 update. Ann Rheum Dis. 2023 Jan;82(1):19-34.

21. Chen YH, Huang WN, Chen YM, Lai KL, Hsieh TY, Hung WT, Lin CT, Tseng CW, Tang KT, Chou YY, Wu YD, Huang CY, Hsieh CW, Chen YJ, Liao YW, Chen HH. The BASDAI Cut-Off for Disease Activity Corresponding to the ASDAS Scores in a Taiwanese Cohort of Ankylosing Spondylitis. Front Med (Lausanne). 2022 May 16;9:856654.

MOLECULAR APPROACH TO PREMATURE EJACULATION: A PILOT STUDY ON S1P SERUM LEVELS AND S1PR1, S1PR2, S1PR3 POLYMORPHISMS

Didem TURGUT COŞAN [1], Gülcan GÜLEÇ [2], İbrahim Uğur ÇALIŞ [3,*], Melis DANIŞMAN SONKURT [2], İyimser ÜRE [4], Fezan MUTLU [5]

[1]Eskisehir Osmangazi University, Medical Faculty, Department of Medical Biology, Eskisehir, TURKIYE
[2]Eskisehir Osmangazi University, Medical Faculty, Department of Psychiatry, Eskisehir, TURKIYE
[3]Mugla Sitki Kocman University, Medical Faculty, Department of Medical Biology, Mugla, TURKIYE
[4]Eskisehir Osmangazi University, Medical Faculty, Department of Urology, Eskisehir, TURKIYE
[5]Eskisehir Osmangazi University, Medical Faculty, Department of Biostatistics, Eskisehir, TURKIYE
Correspondence: ugurcalis@mu.edu.tr

ABSTRACT

Objective: Sphingosine-1-phosphate (S1P) and its receptors are involved in various sexual functions, particularly in smooth muscle regulation and vascular responses. However, the role of S1P and its receptors in premature ejaculation (PE) remains unclear. This study investigates the relationship between single nucleotide polymorphisms (SNPs) in the S1PR1, S1PR2, and S1PR3 genes and plasma S1P levels in individuals with PE.

Materials and Methods: The study included 100 individuals with PE and 100 healthy controls recruited from urology and psychiatry clinics. DNA was isolated from blood samples, and PCR was used to identify SNPs in the S1PR1 (rs2038366), S1PR2 (rs56357614), and S1PR3 (rs7022797) genes. Plasma S1P levels were measured using ELISA.

Results: A significant association was observed between the heterozygous GT genotype of the S1PR1 gene and an increased risk of PE (OR 2.25, 95% CI 1.215–4.168, p = 0.0099). No significant associations were found between S1PR2 or S1PR3 polymorphisms and PE. Plasma S1P levels were significantly lower in the PE group (median 253.25 ng/L) compared to the control group (median 430.82 ng/L) (p < 0.001).

Conclusion: S1PR1 gene polymorphism and reduced plasma S1P levels may be linked to the pathophysiology of PE. In contrast, S1PR2 and S1PR3 do not appear to be associated. Further research with larger samples is needed to confirm these findings.

Keywords: Premature Ejaculation, S1P, S1P receptors, Gene polymorphism

INTRODUCTION

Premature ejaculation (PE) is a common sexual issue among men, with prevalence rates ranging from 10% to 40% (1). It is characterized by ejaculation that consistently occurs before or within one minute of vaginal penetration, along with the inability to delay ejaculation, resulting in distress and negative personal consequences (2, 3). Although multiple factors, including genetic predisposition, contribute to PE, its exact pathophysiology remains unclear (4). PE is persistent, typically lasting more than six months with the same partner, leading to significant emotional and relational issues (2). Sphingosine-1-phosphate (S1P) is a signaling lipid involved in numerous biological processes. It plays a critical role in maintaining cellular homeostasis, cell movement, and angiogenesis (5, 6). Synthesized by sphingosine kinases (SphK), S1P regulates functions such as cell growth and endothelial migration (7, 8). S1P's role in vascular regulation has made it an area of interest in sexual health, particularly in conditions like erectile dysfunction (ED) (3, 6). However, the relationship between PE and S1P has yet to be explored. This study aims to investigate the relationship between single nucleotide polymorphisms (SNPs) in S1PR1 (rs2038366), S1PR2 (rs56357614), and S1PR3 (rs7022797) and plasma S1P levels. This is the first study to evaluate S1P and its receptor polymorphisms in the context of PE.

MATERIALS AND METHODS

Study design

The study group included men between the ages of 18-65 who had premature ejaculation and had sexual partners for at least 6 months. These people do not have a psychiatric first axis disorder, mental retardation, previous head trauma, or any neurological disorders and urological diseases. Also, attention was paid to the fact that these individuals did not use alcohol, substances, and antidepressants and volunteered to participate in the study. The control group included individuals without any complaints of premature ejaculation, no serious chronic physical disease, no previous psychiatric disorder or mental retardation, and no link to the study group. The study group was composed of patients who applied to ESOGU Medical Faculty Hospital Urology and Psychiatry outpatient clinic with premature ejaculation. The control group was composed of men who applied to the Urology outpatient clinic of ESOGU Medical Faculty for infertility and the psychiatry outpatient unit for sexual dysfunction. However, these individuals were not diagnosed with any sexual dysfunction, and attention was paid to volunteering. All participants provided informed consent in compliance with the study protocol. The study was approved by the Eskisehir Osmangazi University's Ethics Committee (approval no: 2018-31). The selected SNPs in S1PR1 (rs2038366), S1PR2 (rs56357614), and S1PR3 (rs7022797) were chosen for their potential impact on vascular function and smooth muscle regulation, both of which are key in the pathophysiology of premature ejaculation (PE). **S1PR1** (rs2038366) is located in the promoter region and may affect gene expression. **S1PR2** (rs56357614) is a coding variant that leads to an amino

acid substitution, possibly altering receptor function. **S1PR3** (rs7022797) is a non-coding intronic variant that may influence splicing or regulatory mechanisms. Due to this association, we selected these SNPs for our study.

Blood sample collection and S1p level determination

Venous blood samples of 10 cc from the participants were taken into tubes containing EDTA (ethylenediaminetetraacetic acid). First, blood plasma was obtained by applying centrifugation at 3000 rpm for 10 minutes. S1P levels were determined spectrophotometrically (Multiscan GO, ThermoFisher, USA) at 450 nm by ELISA kit (YL Biont, Shanghai, CHINA) procedure from blood plasma.

DNA isolation

DNA isolation was performed from the blood samples of the participants (Thermo Scientific GeneJET Genomic DNA Purification, USA) in accordance with the kit procedure. The DNAs obtained were kept at -20°C until use.

PCR amplification and snp genotyping

The S1PR1 receptor gene (Assay ID rs2038366), S1PR2 receptor gene (Assay ID rs56357614), and S1PR3 receptor gene (Assay ID rs7022797) were amplified using PCR. The PCR Amplification Mix consisted of 10 μl of Master Mix TaqProb 2x (Abmgood, Canada), 1 μl of probe (Applied Biosystems, Thermo Fisher Scientific, USA), 5 μl of distilled water (dH$_2$O), and 4 μl of DNA sample, bringing the total volume to 20 μl. The amplification was conducted using a Step One Plus PCR machine (Applied Biosystems, Thermo Fisher Scientific, USA) with the following thermal cycling conditions: an initial denaturation at 95°C for 10 minutes, followed by 40 cycles of 95°C for 3 seconds (denaturation) and 60°C for 30 seconds (annealing), and a final hold at 25°C for 30 seconds. After PCR amplification, the temperature was gradually increased to generate a melting curve for each sample. Single nucleotide polymorphisms (SNPs) were identified by differentiating between the typical sequence and the sequence containing polymorphisms during this process.

Statistical analysis

Continuous variables were evaluated for normality using the Shapiro-Wilk test. Mann-Whitney U tests were used to compare groups for variables that deviated from normality. Continuous data are presented as median values with interquartile ranges (25th to 75th percentiles), while categorical data are reported as frequencies and percentages. Binary logistic regression analysis was conducted to assess the risk of PE. Statistical analyses were performed using IBM SPSS Statistics version 21.0 (IBM Corp., Armonk, NY). A power analysis was conducted with a 5% alpha level and an effect size (W) of 0.23. The analysis indicated that a

sample size of 148 would be sufficient to detect significant differences with 80% power. A chi-square test yielded a chi-square value of 7.8623 with 1 degree of freedom. In this study, the allocation ratio was 1:1, with 100 participants in the patient group and 100 in the control group (G-Power Version 3.1.9.4, Frans Faul, Germany). A statistical significance level of p<0.05 was considered statistically significant. Individuals from the PE and control groups whose genotypes could not be determined during the analysis were excluded from the study (For **S1PR1**, 6 individuals from the control group and 5 from the PE group were excluded. For **S1PR2**, 6 individuals were excluded from both groups. For **S1PR3**, 9 from the control group and 12 from the PE group were excluded).

RESULTS

Genotypic distribution of S1PR1, S1PR2, and S1PR3 genes

The genotypic distribution of the S1PR1, S1PR2, and S1PR3 receptor genes in the control group and individuals with premature ejaculation (PE) was analyzed, with the results presented in **Table 1**. Analysis of the S1PR1 gene revealed a significantly higher frequency of the GT genotype in individuals with PE (63.13%) compared to the control group (42.31%). This suggests a potential association between the GT genotype and an increased risk of PE (p < 0.05). while the **S1PR2** and **S1PR3 genes** did not show any statistically significant differences between the control and PE groups.

Table 1. Distribution of Genotypes for S1PR1, S1PR2, and S1PR3 Receptor Genes in Control and Premature Ejaculation Groups

Gene	Group	GG (n, %)	GT (n, %)	TT (n, %)	P-value
S1PR1	Control	45 (60.8)	40 (40.8)	9 (52.9)	0.033
	PE	29 (39.2)	58 (59.2)	8 (47.1)	
S1PR2	Control	17 (63)	76 (48.7)	1 (20)	0.163
	PE	10 (17)	80 (51.3)	4 (80)	
	Control	17 (39.5)	45 (54.9)	29 (53.7)	0.233
S1PR3	PE	26 (60.5)	37 (45.1)	25 (46.3)	

Genotype comparison of S1PR1, S1PR2 and S1PR3 genes

We examined the association between specific genotypes of the S1PR1, S1PR2, and S1PR3 receptor genes and disease risk, using odds ratios (OR) and confidence intervals (CI). The analysis for the **S1PR1 gene,** comparing the **TT** and **GG** genotypes did not reveal a statistically significant difference in disease risk (odds ratio (OR) 1.379, confidence interval 0.477–3.983, p = 0.552). Similarly, no significant association was observed when comparing the **TT** and **GT** genotypes (OR 0.613, confidence interval 0.218–1.724, p = 0.354). However, a significant association was detected in the comparison between the **GT** and **GG** genotypes. Individuals with the **GT genotype** were found to have a **2.250-fold increased risk** of developing the disease compared to those with the **GG genotype**, and this difference was statistically significant (OR 2.250, confidence interval 1.214–4.168, p <0.001).

Table 2. Comparative Analysis of Genotype Frequencies for S1PR1, S1PR2, and S1PR3 Receptor Genes in Control and Premature Ejaculation Groups

Receptor genes	Odds ratio	95% confidence intervals	P-value
S1PR1 receptor gene rs2038366			
TT vs GG	1.379	0.477-3.983	0.552
TT vs GT	0.613	0.218-1.724	0.354
GT vs GG	2.250	1.214-4.168	<0.001
S1PR2 receptor gene rs56357614			
TT vs GG	6.80	0.664-69.638	0,106
TT vs GT	3.80	0.451-34.76	0,237
GT vs GG	1.789	0.771-4.152	0,175
S1PR3 receptor gene rs7022797			
GG vs TT	1.774	0.784-3.997	0.166
GT vs TT	0.954	0.4787-1.901	0.893
GG vs GT	1.860	0.8784-3.938	0.105

The risk of disease was **2.250 times higher** and significant. (**Table 2**). Individuals carrying the heterozygous **GT** genotype in the S1PR1 receptor gene have an increased risk of disease compared to individuals carrying the homozygous **GG** genotype. The analysis of the S1PR2 gene showed that the risk of disease was higher when comparing the TT genotype to the GG genotype. (odds ratio 6.80, confidence interval 0.664–69.638, p=0.106), but this difference was not statistically significant. No significant difference was observed when comparing the TT genotype to the GT genotype (odds ratio 3.80, confidence interval 0.451–34.76, p=0.237). Similarly, no significant difference in risk was found when comparing the GT genotype to the GG genotype (odds ratio 1.789, confidence interval 0.771–4.152, p=0.175) (**Table 2**).The analysis of the **S1PR3**

gene showed no significant difference in disease risk when comparing the **GG genotype** to the **TT genotype** (odds ratio 1.774, confidence interval 0.784–3.997, p=0.166). Likewise, no significant difference was found between the GT and TT genotypes (odds ratio 0.954, confidence interval 0.4787–1.901, p=0.893). A potential increase in risk was observed when comparing the GG genotype to the GT genotype (odds ratio 1.860, confidence interval 0.8784–3.938, p=0.105), but this difference was not statistically significant (**Table 2**). There is no significant relationship between the S1PR2 and S1PR3 genotypes and disease risk.

Plasma S1P levels

Plasma S1P levels were significantly lower in patients with premature ejaculation (median 253.25 ng/L (146.13–525.13) compared to the control group (median 430.82 ng/L (332.87–738.25) (p < 0.001).

DISCUSSION

Our study adds valuable insights to the expanding research on the role of sphingosine-1-phosphate (S1P) in sexual health. S1P, a lysophospholipid, plays an essential role in cellular homeostasis, regulating key cellular processes such as endothelial permeability, cytokine release, and vascular tone (11). Notably, lower serum/plasma levels of S1P have been observed in various pathological conditions, including erectile dysfunction (ED) (24, 25). Several studies have established the connection between S1P and its receptors, particularly in the context of sexual functions (23). In this study, we found a significant difference in plasma S1P levels between individuals with premature ejaculation (PE) and the control group, suggesting a possible relationship between reduced S1P levels and PE. Beyond ED, where elevated S1P levels are often observed, our findings indicate that plasma S1P levels were significantly lower in PE patients. This may point to a different pathological mechanism involving S1P, highlighting the need for further research into the specific roles of S1P and its receptors in PE. S1P exerts its effects through five G protein-coupled receptors (S1PR1–S1PR5), which are widely expressed in various tissues, including the vasculature and smooth muscle (12, 13). These receptors mediate critical vascular responses, such as smooth muscle relaxation and vasoconstriction. In the human corpus cavernosum, S1PR1, S1PR2, and S1PR3 have been detected and are known to regulate vascular responses through G protein-mediated signaling pathways, including PI3K-Akt and phospholipase C (7, 14). These mechanisms, known to play significant roles in erectile function, may similarly contribute to the pathophysiology of PE. In our analysis of SNPs in S1P receptor genes, we identified a significant association between the heterozygous GT genotype of the S1PR1 gene and an increased risk of PE compared to the homozygous GG genotype. This suggests a potential role for S1PR1 polymorphisms in the development of PE. The biological mechanisms of S1PR1 include the activation of endothelial nitric oxide synthase (eNOS), which induces smooth muscle relaxation and promotes vascular health (14). This mechanism, validated in other studies of ED, may extend to PE, warranting further investigation. Conversely, S1PR2 and S1PR3

polymorphisms did not show a significant association with PE in our study. These receptors are involved in both Gi-linked pathways and other G protein signaling pathways, such as phospholipase C and RhoA/ROK, which regulate vasoconstriction (17). While S1PR2 and S1PR3 play roles in vascular function, their lack of association with PE in our study suggests that S1PR1 may be the primary receptor involved in this condition. Given these findings, future research should focus on the specific signaling pathways mediated by S1PR1 in PE, particularly those involving nitric oxide production and smooth muscle regulation. Larger studies are needed to confirm these results and to explore whether similar associations are found in other populations.

CONCLUSION

In conclusion, our study suggests that both plasma S1P levels and S1PR1 receptor gene polymorphisms may be involved in the pathophysiology of PE. This study is the first to establish a connection between S1P receptor gene polymorphisms and PE, paving the way for further investigation in this promising field.

Authorship contributions

Authorship Contributions All authors have contributed equally to the work

Data availibity statement

The authors state that the data supporting the study's results can be found in the article. Additionally, the raw data can be obtained from the corresponding author upon a reasonable request.

Declaration of competing interest

The Authors declare no conflict of interest pertaining to the current work

Ethics

The study was approved by the Eskisehir Osmangazi University's Ethics Committee (approval no: 2018-31)

REFERENCES

1. Canat L, Değirmentepe RB, Atalay HA, Alkan İ, Özbir S, Çulha MG, Ötünçtemur A. The relationship between female sexual function index domains and premature ejaculation. International urology and nephrology. 2018;50(4):633-7.

2. Steggall MJ. Premature ejaculation: definition, assessment and management. Trends in Urology, Gynaecology & Sexual Health. 2010;15(3):39-43.

3. McMahon CG, Althof S, Waldinger MD, Porst H, Dean J, Sharlip I, et al. An evidence-based definition of lifelong premature ejaculation: Report of the International Society for Sexual Medicine Ad Hoc Committee for the Definition of Premature Ejaculation. BJU international. 2008;102(3):338-50.

4. Cinar O, Durmus N, Aslan G, Demir O, Evcim A, Gidener S, Esen A. Effects of the dopamine D3 receptor agonist 7-hydroxy-2-(di-N-propylamino) tetralin in hyperthyroidism-induced premature ejaculation rat model. Andrologia. 2018;50(4):e12956.

5. Watterson KR, Ratz PH, Spiegel S. The role of sphingosine-1-phosphate in smooth muscle contraction. Cellular signalling. 2005;17(3):289-98.

6. Ling B, Chen L, Alcorn J, Ma B, Yang J. Sphingosine-1-phosphate: a potential therapeutic agent against human breast cancer. Investigational new drugs. 2011;29(2):396-9.

7. Yin J, Guo Ym, Chen P, Xiao H, Wang Xh, DiSanto ME, Zhang Xh. Testosterone regulates the expression and functional activity of sphingosine-1-phosphate receptors in the rat corpus cavernosum. Journal of cellular and molecular medicine. 2018;22(3):1507-16.

8. Kim RH, Takabe K, Milstien S, Spiegel S. Export and functions of sphingosine-1-phosphate. Biochimica et Biophysica Acta (BBA)-Molecular and Cell Biology of Lipids. 2009;1791(7):692-6.

9. Sarkar S, Maceyka M, Hait NC, Paugh SW, Sankala H, Milstien S, Spiegel S. Sphingosine kinase 1 is required for migration, proliferation and survival of MCF-7 human breast cancer cells. FEBS letters. 2005;579(24):5313-7.

10. Michel MC, Mulders AC, Jongsma M, Alewijnse AE, Peters SL. Vascular effects of sphingolipids. Acta Paediatrica. 2007;96:44-8.

11. Geho DH, Bandle RW, Clair T, Liotta LA. Physiological mechanisms of tumor-cell invasion and migration. Physiology. 2005;20(3):194-200.

12. Im D-S, Clemens J, Macdonald TL, Lynch KR. Characterization of the Human and Mouse Sphingosine 1-Phosphate Receptor, S1P5 (Edg-8): Structure– Activity Relationship of Sphingosine1-Phosphate Receptors. Biochemistry. 2001;40(46):14053-60.

13. Im D-S, Heise CE, Ancellin N, O'Dowd BF, Shei G-j, Heavens RP, et al. Characterization of a novel sphingosine 1-phosphate receptor, Edg-8. Journal of Biological Chemistry. 2000;275(19):14281-6.

14. Igarashi J, Michel T. Sphingosine-1-phosphate and modulation of vascular tone. Cardiovascular research. 2009;82(2):212-20.

15. Schuchardt M, Tölle M, Prüfer J, van der Giet M. Pharmacological relevance and potential of sphingosine 1-phosphate in the vascular system. British journal of pharmacology. 2011;163(6):1140-62.

16. Takuwa N, Du W, Kaneko E, Okamoto Y, Yoshioka K, Takuwa Y. Tumor-suppressive sphingosine-1-phosphate receptor-2 counteracting tumor-promoting sphingosine-1-phosphate receptor-1 and sphingosine kinase 1—Jekyll Hidden behind Hyde. American journal of cancer research. 2011;1(4):460.

17. Takuwa Y, Okamoto Y, Yoshioka K, Takuwa N. Sphingosine-1-phosphate signaling and biological activities in the cardiovascular system. Biochimica et Biophysica Acta (BBA)-Molecular and Cell Biology of Lipids. 2008;1781(9):483-8.

18. Aydin M, Downing K, Villegas G, Zhang X, Chua R, Melman A, DiSanto ME. The sphingosine-1-phosphate pathway is upregulated in response to partial urethral obstruction in male rats and activates RhoA/Rho-kinase signalling. BJU international. 2010;106(4):562-71.

19. Chiba Y, Suzuki K, Uechi M, Kurihara E, Goto K, Sakai H, Misawa M. Downregulation of sphingosine-1-phosphate receptors in bronchial smooth muscle of mouse experimental asthma. Pharmacological research. 2010;62(4):357-63.

20. Zhang Xh, Melman A, DiSanto ME. Update on corpus cavernosum smooth muscle contractile pathways in erectile function: a role for testosterone? The journal of sexual medicine. 2011;8(7):1865-79.

21. Coşan DT, Çalış İU, Güleç GK. Membran Fosfolipidlerinden Sfingozin-1-Fosfat ve Reseptörlerinin Erektil Disfonksiyondaki Rolü. Tıp Fakültesi Klinikleri Dergisi.1(3):17-

22. di Villa Bianca RdE, Sorrentino R, Sorrentino R, Imbimbo C, Palmieri A, Fusco F, et al. Sphingosine 1-phosphate induces endothelial nitric-oxide synthase activation through phosphorylation in human corpus cavernosum. Journal of Pharmacology and Experimental Therapeutics. 2006;316(2):703-8.

23. Nazlıkul Hs. Erektil Disfonksiyon. Bilimsel Tamamlayıcı Tıp Regülasyon ve Nöral Terapi Dergisi.10(2):1-7.

24. Soltau I, Mudersbach E, Geissen M, Schwedhelm E, Winkler MS, Geffken M, et al. Serum-sphingosine-1-phosphate concentrations are inversely associated with atherosclerotic diseases in humans. PLoS One. 2016;11(12).

25. Winkler MS, Nierhaus A, Holzmann M, Mudersbach E, Bauer A, Robbe L, et al. Decreased serum concentrations of sphingosine-1-phosphate in sepsis. Critical Care. 2015;19(1):372.

26. Cho MC, Song WH, Paick J-S. Suppression of cavernosal fibrosis in a rat model. Sexual medicine reviews. 2018;6(4):572-82.

27. Sassoli C, Pierucci F, Zecchi-Orlandini S, Meacci E. Sphingosine 1-phosphate (S1P)/S1P receptor signaling and mechanotransduction: implications for intrinsic tissue repair/regeneration. International journal of molecular sciences. 2019;20(22):5545.

28. Guo L, Ou X, Li H, Han Z. Roles of sphingosine-1-phosphate in reproduction. Reproductive Sciences. 2014;21(5):550-4.

Research Article

THE EFFECT OF DIFFERENT STAINING SOLUTIONS ON THE COLOR STABILITY OF PERMANENT INDIRECT COMPOSITE RESINS PRODUCED BY ADDITIVE AND SUBTRACTIVE TECHNIQUES

Nazire Esra ÖZER [1]*, Zeynep ŞAHİN [1], Cansu YIKICI ÇÖL [2], Özlem ARIK [3], Mehmet Ali KILIÇARSLAN [4]

[1] Department of Prosthodontics, Faculty of Dentistry, Lokman Hekim University, Çankaya, Ankara, TURKIYE
[2] Panorama Ankara Oral and Dental Health Clinic, Çankaya, Ankara, TURKIYE
[3] Kutahya Health Sciences University, Central Campus, Kutahya, TURKIYE
[4] Department of Prosthodontics, Faculty of Dentistry, Ankara University, Yenimahalle, Ankara, TURKIYE

*Correspondence: esra.ozer@lokmanhekim.edu.tr

ABSTRACT

Objective: To investigate the effects of various beverages on the color stability of permanent composite resins produced by additive (AM) or subtractive manufacturing (SM) techniques comparatively.

Materials and Methods: Six composite resin materials produced by SM (Vita Enamic-VE, Cerasmart-CE, Lava Ultimate-LU) and AM (VarseoSmile Crown plus-VSC, Saremco print CROWNTECH-SPC, Formlabs 3B Permanent Crown-FPC) techniques were selected and soaked in different solutions (artificial saliva, black tea, coffee) for different times (1 and 7 days). L*, a*, b* values of the samples were recorded using a spectrophotometer. The color changes of the samples were determined using the CIELAB formula. In determining the color differences between the test materials, ANOVA was used for parametric data and Kruskal-Wallis analysis for non-parametric data.

Results: Group VE was the least stained group on the 1st and 7th day of artificial saliva solution and the 7th day of coffee solution, while Group CE was the least stained group on the 1st day of coffee solution. In the tea solution, on the 1st and 7th days, there wasn't difference in the materials' color change (p>0.05). Tea and coffee solutions caused statistically significantly more color change in all test materials than artificial saliva (except Group CE on the 7th day, Group VSC and FPC on the 1st day) (p<0.05).

Conclusion: 3D permanent composite resins generally showed more staining than CAD/CAM milled composite resins. Tea and coffee staining solutions changed the color of the materials compared to artificial saliva. As the storage time increased, more color changes were observed.

Keywords: Composite Resins, 3D printing, CAD/CAM milling, Color stability

INTRODUCTION

Recent advancements in the digital workflow have significantly impacted research fields in dentistry today (1). Particularly, with the advancement of computer-aided design and computer-aided manufacturing (CAD/CAM), dental treatments can be performed more effectively, easily and quickly (2). Focusing on a digital workflow, CAD/CAM systems have significantly surpassed traditional prosthesis manufacturing procedures (1). Following data collection, the digital workflow uses CAD software to process the data before digitally designing the restorations. During the fabrication process, additive manufacturing (AM) or subtractive manufacturing (SM) techniques may be preferred (3).

The SM technique, causes more material to be consumed than the material to be obtained because it performs production by milling from a block of material (1,3). As such, the cost is relatively high. The AM method, which is based on layering layers on top of each other, was developed following the need to reduce costs (4). The term AM is the process of creating a three-dimensional (3D) object designed in a virtual environment with 3D printers that perform the printing process (5). It is predicted that 3D printers used in AM technology will become the main method for digital production in dentistry in the future by finding wide usage areas in many fields, especially in prosthodontics, due to their advantages such as fast and detailed production, freedom and ease of design, material and workforce saving (1, 3, 4). Stereolithography (SLA) and digital light processing (DLP) are the two AM methods most popularly utilized in resin-based dental restorations. The foundation of both technologies is the polymerization of liquid resin with a UV and/or laser source (3).

Dental material development related to AM technology has significantly increased in recent years (6, 7). A variety of printable resins have entered the market recently and are being used for producing both permanent and temporary fixed prosthetic restorations. The use of composite resin materials for permanent restorations, particularly single crowns, inlays, onlays, and veneers, has emerged as a suitable solution for restorative and prosthetic rehabilitation (8, 9). However, their use is still limited by their questionable mechanical and physical properties (10, 11), biocompatibility (12, 13), antimicrobial properties (14), and optical properties due to the presence of residual monomers formed during post-processing (15-17).

Color harmony and color stability are essential in composite materials because they are used as materials that mimic the appearance of natural teeth. One of the most important indications for the replacement of composite restorations after intraoral use is color change (18). Discoloration of restorative materials is an undesirable effect of aesthetic dental resin composites, although inevitable in the oral environment (19).

It is known that the various stain types to which the material is subjected, the surface roughness and composition, exposure frequency, and duration all have an impact on the color stability of restorative

materials (17). The color stability of conventional resin restorative materials has been shown to be considerably impacted by frequent exposure to coloring beverages like coffee and tea (19). In addition to material composition, finishing and polishing techniques can also have an impact on the quality of the composite surface and may therefore be associated with early discoloration (21). The manufacturing method used can also have an impact on the color stability of the restorative material (17). In particular, the "stair-step phenomenon" commonly observed in 3D printing technology may be important when considering the aesthetic properties of composite resin restorations and hence color stability (17, 22). Additionally, the AM technique's post-polymerization step influences the material's ultimate structure based on the quantity of residual monomer, which could directly affect the printed material's color stability (23).

Thresholds for visual color differences can be applied as a quality control measure and as a reference for choosing aesthetic materials (24). Visual assessment and digital color measurement devices are used in the evaluation of color change. In visual assessment, many factors such as light source, gingival color, distance of the colored object to the eye, environmental factors, and experience affect the color assessment of dentists (24). Therefore, digital colorimeters such as colorimeters and spectrophotometers, which can make reproducible measurements with sensitive, quantitative techniques, are preferred to obtain more precise and reliable results in the evaluation of color change (24, 25).

For measuring color difference values, the Commission Internationale de l'Eclairage (CIE) L* a* b* color system is utilized (26, 27). L* a* b* values are referred to as "chromaticity coordinates" in this 3D color system: The L* a* b* values in this 3D color system are referred to as "chromaticity coordinates":(L*) stands for "lightness"; the higher the L value, the greater the lightness. (a*) shows positive values as red and negative values as green (-a*=green; +a*=red); (b*) shows positive values as yellow and negative values as blue (b*=blue; +b*=yellow). Mean color difference values (ΔE) is a numerical value indicating the amount of perceived color difference between two objects (26, 28).

In the researches, color changes and surface roughness of resin based composite blocks produced with CAD/CAM milling systems have been investigated (26, 29). However, a scoping analysis conducted recently (30) showed that the properties of 3D printing polymers have not yet been sufficiently assessed and characterized. This knowledge is important to successfully manage these materials and the satisfaction of patients' increasing aesthetic preferences. Although no comprehensive studies are comparing permanent polymeric-based composite resins produced by both subtractive and additive digital methods, the studies that have been conducted generally include 3D composite resins used for temporary restorations (1, 31-35).

Therefore, the purpose of this study was to compare the effects of coloring-potent beverages like coffee and tea on the staining and color stability of permanent composite resins produced by the AM and SM techniques. The study's null hypothesis declares that there won't be any variations in staining properties

based on the type of restoration material used, the kind of colorant solutions employed, or how long the ingredients in the colorants are stored.

MATERIALS AND METHODS

This study comparatively investigated the staining sensitivity and color stability of permanent composite resins produced by SM (Vita Enamic-VE, Cerasmart-CE, Lava Ultimate-LU) and AM (VarseoSmile Crown plus-VSC, Saremco print CROWNTECH-SPC, Formlabs 3B Permanent Crown-FPC) method in three different solutions (artificial saliva, black tea, coffee) at different times (0, 1 and 7 days).

Table 1. Content details of composite resins in test groups

Production method	Trade name	Abbr	Material type	Matrix Type	Filler type and content	Manufacturer
SM	Vita Enamic	VE	Polymer infiltrated ceramic network	UDMA, TEGDMA	Feldspar ceramic enriched with aluminum oxide (86%) Silica (20nm), zirconia (4–11 nm)	Vita Zahnfabrik, Bad Sackingen, Germany
	Cerasmart	CE	Resin nano ceramic	BisMEPP, UDMA, DMA	Silica (20 nm) ve Barium glass (300 nm) (71%)	GC Corp., Tokyo, Japan
	Lava Ultimate	LU		BisGMA, UDMA, BisEMA, TEGDMA	Silica (20 nm), zirconia (4–11 nm) (80%)	3M ESPE Dental Products, St. Paul, MN, USA
AM	Saremco print CROWNTEC	SPC	3D printing composite	BisEMA	Silanized dental glass (0.7μm) (30-50%)	Saremco Dental AG; Rebstein, Switzerland
	VarseoSmile Crown plus	VSC		2-methylprop-2-enoic acid phosphine oxide	Silanized dental glass (0.7μm) (30-50%)	Bego, Bremen, Germany
	Formlabs 3D Permanent crown	FPC		50-75% esterification products of 2-methylprop-2-enoic acid (methacrylate)	Silanized dental glass (0.7μm) (30-50%)	Formlabs, Somerville, MA, US

(SM: Subtractive manufacturing, AM:, Additive manufacturing, 3D: three-dimensional , Bis-GMA: bisphenol A diglycidylether methacrylate, Bis-MEPP: 2,2- Bis (4-methacryloxypolyethoxyphenyl) propane, UDMA: urethane dimethacrylate, TEGDMA: triethylene glycol dimethacrylate, Bis-EMA: ethoxyl ated bisphenol-A dimethacrylate, DMA: dimethacrylate)

The minimum sample size for this study was calculated as n = 12 (N = 216) per group with an effect size of 0.50, 90% power, and an error level of α = 0.05. Table 1 presents an overview of the properties and compositions of all the materials employed in the research.

Table 2. Production and polishing procedures of test groups

Group code	Production methods	Post-processing procedure*	Polishing procedure*
VE	CAD/CAM blocks were wet sliced with a diamond saw using a precision cutting machine (Microcut 201, Metkon, Turkey)	-	- The top surfaces of all samples were polished with Sof-Lex Diamond Polishing System (3M ESPE St Paul, MN, USA). - 4 different grades of abrasive aluminum oxide coated discs were applied in decreasing order of grits. - Coarse (100 μm), Medium (29 μm), Fine (14 μm), and Super Fine (8 μm) discs were used, respectively. - A single operator used a low speed hand equipment running at 15,000 rpm to apply a dry. - A new disc was used to polish each specimen. - Each disc was applied in the same direction for 15-20 seconds for standardization.
CE			
LU			
SPC	AM technique: DLP-based Printer: Asiga Max UV (Asiga, Anaheim Hills, CA, USA) Printing layer thickness: 50 μm Printing orientation:0	- Washing was performed for 2-3 minutes in 98% concentrated isopropanol using ultrasonic technology. - The Otoflash G171 device (NK Optik, Baierbrunn, Germany) was used to cure the light with 4000 lighting exposures while being in a nitrogen oxide gas atmosphere.	
VSC	AM technique: DLP-based Printer: Varseo XS (Bego, Bremen, Germany) Printing layer thickness: 50 μm Printing orientation:0°	-It was washed in a 96% concentrated ultrasonic ethanol bath for 3 minutes and then for 2 minutes. -It was pressurized with nitrogen gas (1.0–1.2 bar) in Otoflash (Bego, Bremen, Germany), which produced 1500 flashes while performing at a frequency of 10 light per second.	
FPC	AM technique: SLA-based Printer: Formlabs (Somerville, Massachusetts, USA) Printing layer thickness: 50 μm Printing orientation:0°	- Submerged in Form Wash (Formlabs, Somerville, MA, USA) for 3 minutes in 99% isopropyl alcohol. -Post-curing was performed twice in Form Cure (Formlabs, Somerville, MA, USA) at 390–405 nm, 60°C for 20 minutes.	

* Performed in accordance with the manufacturer's instructions.(CAD/CAM: Computer-aided design and computer-aided manufacturing, AM: Additive manufacturing, DLP: Digital light processing, SLA: Stereolithography, VE: Vita Enamic, CE: Cerasmart, LU: Lava Ultimate, SPC: Saremco print CROWNTEC, VSC: VarseoSmile Crown plus, FPC: Formlabs 3D Permanent crown)

CAD/CAM blocks were wet-sliced by a diamond saw (Micracut 201, Metkon, Bursa, Turkey) and 108 samples were obtained with a rectangular shape (14 mm x 14 mm x 1.0mm). 3D printing materials (VSC, SPC, FPC) were designed in the same dimensions using a CAD software program (SolidWorks Corp. Concord, MA, USA) and transported to a 3D printer after being converted to Standard Transform Language (STL) format. Group VSC, SPC, and FPC were produced with Asiga Max UV (Asiga, Anaheim Hills, CA, USA), Varseo XS (Bego, Bremen, Germany), Formlabs (Somerville, Massachusetts, USA) 3D printer with a

print layer thickness of 50 μm and a print orientation of 0°, respectively. Post-processing of the 3D test samples was performed by each manufacturer's instructions. Table 2 contains a detailed explanation of these procedures.

For surface standardization, the samples were ground wet with 600, 800, and 1000 grit silicon carbide abrasive paper. All of the sample's dimensions were measured using a digital caliper (Mitutoyo Corp., Tokyo, Japan). Then the top surfaces of all samples were polished by a trained inspector (N.E.O) with Sof-Lex (3M ESPE Dental Products, St. Paul, Minnesota) with low-speed hand equipment. Abrasive aluminum oxide-coated discs of 4 different grades, which are Coarse (100 μm), Medium (29 μm), Fine (14 μm), and Super Fine (8 μm), were applied in descending grit order (Table 2). The produced samples were then submerged in distilled water at 37°C for 24 hours after being washed for 5 minutes in an ultrasonic cleaner.

Following a random division into subgroups (n = 12), a total of 36 samples (A2 shade) from each type of material were submerged in two distinct staining solutions (tea, coffee) and artificial saliva to analyze the time-dependent color difference of the samples obtained. The properties and preparation procedures of the staining solutions used are presented in Table 3.

Table 3. The properties and preparation procedures of the staining solutions

Immersion solution	Manufacturer	Chemical composition	Preparation procedure
Artificial saliva	-	KCl (0.4 g L−1) NaCl (0.4gL−1) CaCl$_2$(H$_2$O) (0.795 g L−1) NaH$_2$PO$_4$(H$_2$O) (0.69 g L−1) Na$_2$S (0.005 g L−1) Urea (1 g L−1)	To create 1 L of artificial saliva, all of the ingredients were mixed. The pH of the saliva was then determined, and 15 ml of 0.1 M NaOH was added to the mixture to obtain a pH of 6.5.
Black Tea	Yellow Label Tea; Lipton, Rize, Turkey	Tea Leaves	1 tea bag was placed in 200 mL of boiled distilled water for 10 min.
Coffee (without sugar)	Nescafe Classic; Nestle,Switzerland	Coffee powder	2 g coffee granules were placed in 200 ml boiled distilled water for 7 min and allowed to cool at room temperature.

(NaCl: Sodium chloride, KCl: Potassium chloride, CaCl$_2$(H$_2$O): Calcium chloride hydrate, NaH$_2$PO$_4$(H$_2$O): Sodium dihydrogen phosphate monohydrate, Na$_2$S: Sodium sulfide, NaOH: Sodium hydroxide)

A spectrophotometer (VITA Easyshade V; Vita Zahnfabrik, Germany) was used to record the samples' quantitative basic color parameters (L*, a*, and b*) in accordance with the CIE system. Measurements were performed in standard D65 illumination (36) in a light-controlled box (31) against a neutral grey background (37). To minimize the possibility of external light reflection on the sample side and to ensure that the light

angle was maintained throughout the test procedure, a custom-made silicone mold was used to hold the sample during color measurement (33). The instrument was calibrated before each measurement, and each sample was measured three times. The values of L*, a*, and b* were obtained by averaging these measurements.

Using the previous reference for artificial saliva (38), coffee and tea were prepared in accordance with the manufacturer's instructions. All samples were then stored in coloring solutions for 24 hours at 37°C in an incubator. All staining solutions were refreshed after each 24 h immersion (39). After the coloring period, each sample was cleaned under distilled water to remove any deposits of coloring solutions and dried with tissue paper before re-measurements (40). The coloring cycle was performed for 7 days and color measurements of all samples were repeated on days 1 and 7. Assuming that 1 cup of coffee is drunk in 15 minutes, it was determined that the exposure time to the coloring beverage was 48 minutes per day and 24 hours per month with an average consumption of 3.2 cups of coffee per day (41). For this reason, the first measurement period selected in this study was determined as 1 day (24 hours), which corresponds to 1 month of use in the mouth, and the other measurement period was increased to 1 week to see the degree of exposure. The color changes of the samples were obtained by calculating the ΔE value according to the CIE L*a*b system. In the formula, L_1^*, a_1^*, and b_1^* are the first measurement values and L_2^*, a_2^*, and b_2^* are the second measurement values.

$$\Delta E^* = [(L_1^*-L_2^*)^2 + (a_1^*-a_2^*)^2 + (b_1^*-b_2^*)^2]^{1/2}$$

Statistical analyses of surface roughness and ΔE values were calculated using the SPSS (Version 22 IBM) package program. The Shapiro-Wilk and Kolmogorov-Smirnov tests were performed to determine whether the data was distributed normally. In determining the color differences between the test materials, the Kruskal-Wallis analysis was used when a one-way analysis of variance was not available. The time-dependent color change within each material group was evaluated by using the Wilcoxon sign test when the dependent sample t-test was normal distribution ($\alpha=0.05$).

RESULTS

The ΔE values obtained from the test groups are shown in Table 4. When material groups are examined on a solution basis; in the artificial saliva solution; Group VE was stained the least on the 1st day and there is a significant difference with all other groups except Group LU and Group VSC. On the 7th day, Group CE was stained the most and had a significant difference with Group VE and Group FPC (p<0.05). In the tea solution, between the materials, there was no difference in color change on the 1st and 7th day

(p>0.05). In the coffee solution, Group CE stained the least on the 1st day and had a significant difference with Group LU and Group FPC (p<0.05). On the 7th day, Group VE stained the least and there is a significant difference with Group LU which stained the most.

Table 4. ΔE values of the test groups in soaked solutions on the 1st and 7th day

Time	Materials	Staining solution			p
		Artificial saliva	**Black tea**	**Coffee**	
ΔE 0-1	**VE**	0.67 ± 0.37[abcAB] 0.57 (0.50)	3.07 ± 1.40[aA] 2.45 (2.32)	2.37 ± 1.15[aB] 2.06 (1.40)	**0.000***
	CE	1.56 ± 0.77[aA] 1.54 (1.00)	2.37 ± 0.89[bA] 2.32 (1.16)	1.67 ± 0.61[bcB] 1.78 (0.97)	**0.030***
	LU	1.35 ± 0.63[dA] 1.09 (1.22)	2.09 ± 0.70[cB] 2.16 (1.25)	3.14 ± 1.32[bAB] 2.90 (1.52)	**0.000***
	SPC	1.71 ± 0.74[bA] 1.57 (1.11)	2.76 ± 1.12[dA] 2.86 (2.84)	2.75 ± 1.39[dB] 2.93 (2.20)	**0.010***
	VSC	1.85 ± 1.66[eA] 1.18 (1.66)	2.06 ± 0.73[eB] 1.95 (1.30)	2.69 ± 1.35[eC] 2.65 (2.12)	0.278*
	FPC	2.34 ± 1.54[cA] 1.90 (1.54)	3.33 ± 1.52[fB] 3.07 (0.99)	3.23 ± 1.13[cC] 3.38 (1.48)	0.181*
p		**0.001****	0.027**	**0.025***	
ΔE 0-7	**VE**	1.72 ± 0.95[aAB] 1.44 (1.47)	5.25 ± 1,44[aA] 5.19 (2.33)	3.80 ± 1.94[aB] 2.96 (3.21)	**0.000***
	CE	4.66 ± 2.42[abA] 4.56 (2.88)	5.31 ± 2,27[bB] 5.50 (3.27)	4.87 ± 2.03[bC] 4.34 (2.54)	0.776*
	LU	2.44 ± 0.88[cA] 2.30 (0.87)	3.99 ± 1,59[cB] 3.62 (2.31)	6.05 ± 1.74[aAB] 5.96 (2.80)	**0.000***
	SPC	3.31 ± 1.41[dAB] 2.60 (1.29)	5.05 ± 1,87[dA] 4.47 (2.27)	4.70 ± 1.85[cB] 4.06 (3.50)	**0.004***
	VSC	2.29 ± 1.00[eAB] 2.13 (1.13)	5.13 ± 1,80[eA] 4.81 (2.31)	6.00 ± 2.01[dB] 5.91 (2.90)	**0.000***
	FPC	2.41 ± 0.89[bAB] 1.49 (0.85)	5.07 ± 1,11[fA] 4.83 (2.27)	5.63 ± 1.35[eB] 5.16 (2.51)	**0.000***
p		**0.000****	0.444*	**0.021***	

*One-way ANOVA, ** Kruskal-Wallis H test. (VE: Vita Enamic, CE: Cerasmart, LU: Lava Ultimate, SPC: Saremco print CROWNTEC, VSC: VarseoSmile Crown plus, FPC: Formlabs 3D Permanent crown). The data are presented as mean ±standard deviation (Mean ± SD) and median and interquartile range Median(IQR). The p value is statistically significant (in bold). Mean difference significant at p<.05; means with same letters statistically different. Lowercase letters for columns, uppercase letters for rows.

When examined according to the solutions immersed within the group on a material basis; in Group VE; tea and coffee solutions caused significant color change compared to artificial saliva on the 1st and 7th day (p<0.05). In Group CE; tea solution caused significant color change compared to artificial saliva on the

1st day (p<0.05), while the staining effect of the solutions was not significant on the 7th day (p>0.05). In Group LU, coffee showed significantly higher staining than the other solutions on the 1st and 7th day (p<0.05). In group SPC, tea solution caused significant color change compared to artificial saliva on the 1st day, while coffee, as well as tea, caused significant color change compared to artificial saliva on the 7th day (p<0.05). In Group VSC and Group FPC, while the staining effect of the solutions was not significant on the 1st day (p>0.05), tea and coffee solutions caused significantly higher discoloration compared to artificial saliva on the 7th day (p<0.05). When all test groups were analysed, 3D permanent composite resins generally showed more staining than CAD/CAM milled composite resins.

The comparison of the ΔE values of the composite samples on the 1st and 7th day within the groups are given in Figure 1. The ΔE values of all samples on the 7th day were higher than the 1st day ΔE values. Group VE, Group CE, and Group LU in black tea, Group SPC and Group VSC in artificial saliva solution, and Group VE and Group SPC in coffee showed statistical differences (p<0.05).
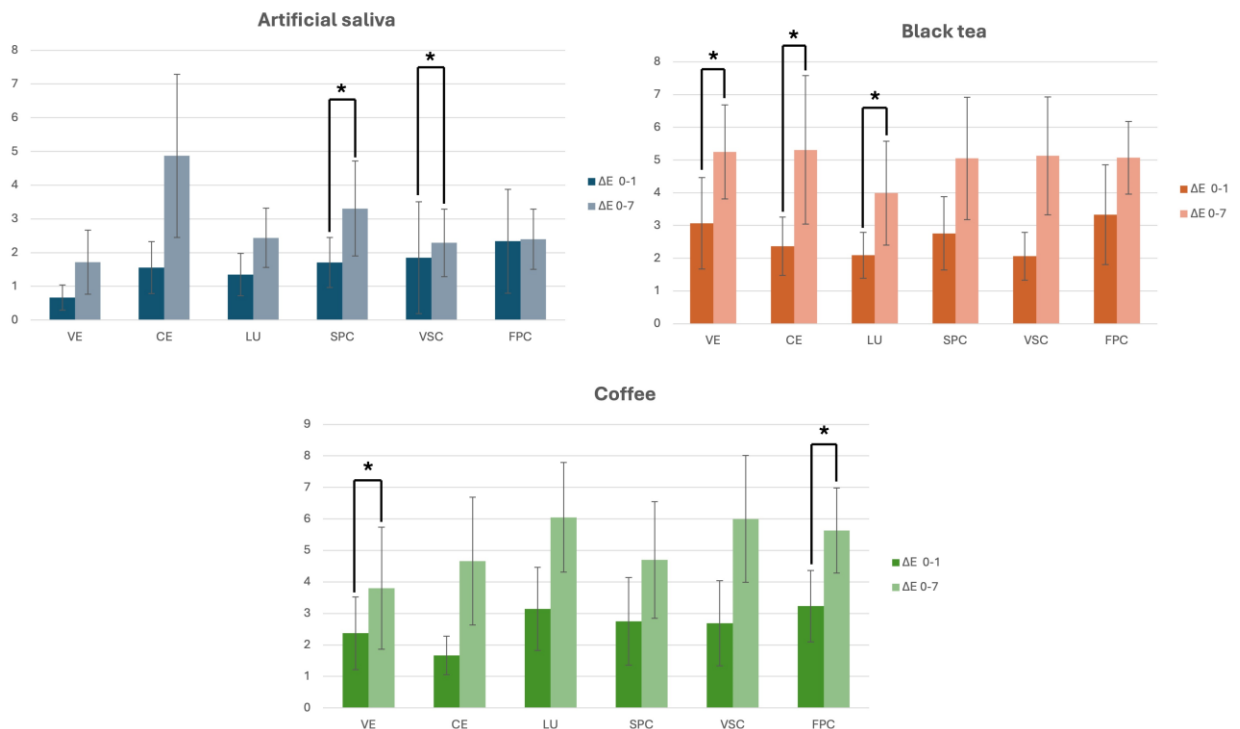
Figure 1. Comparison of ΔE values of material groups according to immersion time periods in the solutions. (VE: Vita Enamic, CE: Cerasmart, LU: Lava Ultimate, SPC: Saremco Print Crowntec, VSC: VarseoSmile Crown plus, FPC: Formlabs 3D Permanent crown) Mean ± standard deviation (Mean ± SD) of ΔE   values. (* p<0.05 indicate statistical differences between groups.)

DISCUSSION

This research compared the color stability of resins produced from permanent composites using digital techniques in different dye solutions in two different periods. The null hypothesis has been rejected in

accordance with this research's results. Significant distinctions have been found in terms of material and solution as well as storage duration.

Changes occur in the physical and chemical properties of resin composites and indirectly in their aesthetic properties due to exposure to food and beverages with coloring properties that are constantly consumed in the oral environment (42). One of the most important indications for the replacement of composite restorations after intraoral use is color change (19).

In dental material examinations, color evaluation by spectrophotometer is the most preferred and reliable method because it can obtain objective, fast and repeatable numerical data (43, 44). As a result, the spectrophotometer color-measuring device was used in this investigation to measure color.

For the numerical expression of color change, the Commission Internationale de l'Eclairage - CIE L* a* b* color system is used (18, 19). The L* a* b* values in this three-dimensional color system are known as "chromaticity coordinates" (26). ΔE is a numerical value that indicates the amount of color difference perceived between two objects and is calculated with the CIELAB formula (28). The data obtained from the study's measurements were recorded as CIE L*a*b* values and calculated using the formula as ΔE values.

O'Brien et al. evaluated the material as stable in terms of color difference if ΔE=0, clinically imperceptible if $0.5 \leq \Delta E \leq 1$, clinically perceptible if $1 \leq \Delta E \leq 2$ and clinically unacceptable if $\Delta E > 3.7$ (46). In dentistry, $\Delta E \geq 3.7$ is often determined as the clinically perceivable threshold value for color difference (45, 46). In this study, the material groups immersed in all solutions used on the 1st day were colored within the clinically acceptable threshold value. Despite the composition of each material, it was found that when the storage period was prolonged, all color changes by the end of the 7th day exceeded the clinical limit in all solutions exception for artificial saliva. In addition, the color change values of all 3D printing groups except Group FPC in artificial saliva, all CAD/CAM groups (Group VE, Group CE and Group LU) in tea, and Group VE and Group FPC materials in coffee on day 7th were statistically significantly higher than those at day 1st.

Depending on the material, colorant type, and timing of storage, the degree of discoloration could differ. The color stability of nanofilled and micro-hybrid composite resins was evaluated by Erdemir et al. (46) and Al-Dharrab et al. (47) following immersion in various a beverage. They found that the material's color stability was influenced by the type of colorant used, how long it was stored, and the chemical structure of the composite resin (47, 48). These results are in line with the study's findings, which showed that colorants and storage duration significantly affected the shades of color.

When the studies evaluating the color stability of composite resins according to the beverage consumption habits of individuals in society are examined, it is seen that many different beverages are used as coloring solutions (30). In this study, coffee and tea solutions were used as coloring solutions due to their popularity and artificial saliva was used as a control. As a result, depending on the type of colorant, the

degree of staining was found to be higher in tea and coffee solutions than in artificial saliva in each material group. On a similar note, Almejrad et al (33) and Ardu et al (37) stated that artificial saliva was the less coloring agent in their studies in which resin-based dental materials were soaked in different solutions including tea, coffee and artificial saliva.

Group VE (CAD/CAM milling) was the least stained group on the 1st and 7th day of artificial saliva solution and the 7th day of coffee solution, while Group CE (CAD/CAM milling) was the least stained group on the 1st day of coffee solution. In general, the discoloration was greater in 3D printing materials (Group SPC, Group VSC and Group FPC) and their color stability wasn't as good as the materials used in CAD/CAM milling (Group VE, Group CE, and Group LU). Similar to our study, Shin et al. (35) investigated the degree of discoloration based on material type, colorant kinds (grape juice, coffee, curry), and colorant storage period for CAD/CAM blocks and 3D printing resins. It was noted that color change increased in all groups with increasing storage times. However, since color stability was found to be less in 3D materials compared to other groups, they stated that color change is a feature that should be taken into consideration when 3D printing resins are used (35). Similarly, Alharbi et al (17) evaluated the color differences of labial veneers produced using milling and 3D printing techniques in different immersion media (coffee, tea and artificial saliva) at 12 and 24 days. Because 3D-printed restorations showed are more susceptible to stains than milled restorations, it is advised that these materials should be used as temporary, short- or long-term restorations rather than permanent restorations (17).

The literature reports a variety of causes for the color instability of 3D printed resin. The surface microstructure of 3D printing has layers because it is based on the AM process (3,24,62). This situation, known as the "stair-step phenomenon", may be important when surface roughness values are considered for color stability (17, 22). The presence of micropores, residual monomers, and potentially incomplete polymerization at the layer interface could all increase the coloration potential of printed materials (17). Another reason may be related to water absorption capacity and solubility. A higher degree of water absorption leads to the absorption of coloring agents, resulting in discoloration of the material (33). Low color stability may also be caused by the 3D-printed composite resin materials' (Group SPC, Group VSC, and Group FPC) lower polymerization rates when compared to other materials (35). In the SM method; Group VE, Group CE and Group LU materials are obtained by milling from industrially produced blocks by polymerizing at high temperature and pressure. As a result, these materials have more compact structures and high polymerization rates (49). In contrast, even though 3D printing resins are applied post-curing to ensure polymerisation and reduce the amount of residual monomer, Shin et al. reported that the polymerisation rate was relatively low in their study (35). In addition to having an impact on biological processes and mechanical strength, a low polymerization rate can raise the risk of discoloration from

decreased surface integrity (23). Also, the presence of residual monomers causes deterioration of surface integrity due to surface softening as a result of hydrolysis (45).

The color and translucency stability of 3D materials for temporary crown and bridge restorations were investigated by Kim et al. (45) at various times following the procedure, including one hour, one day, one week, one month, and six months. They discovered that while the translucency of the 3D printable dental materials varied relatively little, the color stability of the materials altered considerably. After six months of water storage, they discovered that the materials generally got more darker, yellower, and opaque (45). In our study, we measured the samples only on the 1st and 7th day. One of the limitations of our investigation is that the coloration resulting from post-processing procedures could not be observed for a longer period.

The type, size, and quantity of inorganic particles incorporated into the structure of resin composites can influence how susceptible they are to coloration (16, 34). Inorganic particles on the surface may move away from the organic resin matrix during the clinical life of the material and cause the formation of a cavity in that area. As the number of these voids increases, surface irregularity increases (15).

Although the filler content of all 3D printing materials (SPC, VSC, FPC: 30-50%) is less than CAD/CAM milling materials (VE: 86%, CE: 71%, LU: 80%), the high size (SPC, VSC, FPC: 0.7μm) [VE: Silica (20nm), zirconia (4-11nm), CE: Silica (20 nm) and barium glass (300 nm), LU: Silica (20 nm) and zirconia (4-11 nm)] and irregular distribution of fillers can explain the reason for the high color variation of the 3D printed materials in this study. Since the filler particle sizes of CAD/CAM milling materials are smaller, they may have a lower degree of surface discoloration than other materials when separated from the surface. In parallel with the findings of our study, Vichi et al. (15) reported that composites with large inorganic particle sizes had more discoloration compared to composites containing smaller particles. We think that the color change obtained from 3D printing materials is due to the inorganic particle sizes and ratios of the composite.

In addition, it has also been reported that composites with smaller amounts of inorganic particles show increased water absorption and more discoloration due to the higher volume of the organic resin matrix (50). It has an association with the early development of 3D printed material technology, which is still limited in terms of presenting more monomer types and filler loads. The variation in monomer composition in the chemical structure can also be as influential as the organic matrix ratio. The structure of 3D printing materials includes methacrylate (Group VSC and Group FPC) and BisEMA (Group SPC). Because the Bis-EMA monomer doesn't have hydroxyl groups in contrast to the BisGMA monomer, it is less viscous and has a high fluidity, which makes it suitable for 3D printing. Prospective advancements in the types (such as UDMA or TEGDMA) and amounts of classical monomers employed in CAD/CAM composite resins signify a crucial area of research and development for 3D-printed dental materials (15).

When the material groups were analyzed based on solutions; in the artificial saliva solution, there was a difference between Group VE - Group CE, Group VE - Group SPC and Group VE - Group FPC on the 1st

day and between Group VE - Group CE and Group CE - Group FPC on the 7th day. In the tea solution, there was no difference in terms of color change between the materials on the 1st and 7th day. In the coffee solution, there was a difference between Group CE - Group LU and Group CE - Group FPC on day 1 and between Group VE - Group LU on day 7. In paired comparisons, there was nothing noticeable between the groups that were 3D printed. The reason for this may be that the chemical contents are close to each other based on the sharing of the companies. Furthermore, the resins used in this study's 3D printing were produced with specific 3D printers that were appropriate to the resins that the companies suggested.

Print orientation and thickness have an impact on the optical characteristics of dental restorative resins that are 3D printed (51). Espinar et al (16) evaluated the effect of build orientation (0°, 45°, and 90°) on different parameters, including color difference, of 3D-printed provisional resins. As a result of the study, they determined that the effect of changes in build orientation on the topography of 3D printed restorations was significant, but build orientations did not affect any of the variables examined (16). In this study, the parameters for 3D printing were set constant for all samples (Printing layer thickness: 50 μm, Printing orientation: 0°). The study of Espinar et al. which reported that printing direction did not make a difference in terms of color change, supports the use of only 0 degree printing angle in this study.

Limitations of this study include the fact that thermocycling, ultraviolet exposure, smoking and brushing regimes were not applied, which are among the factors that can affect color staining and surface properties. In addition, surface preparation methods, which are necessary to ensure long-lasting aesthetic results, have not been investigated.

Currently, there's not enough data to make a firm judgment about how well 3D-printed permanent restorative materials perform clinically (8). In-vitro studies of much longer duration than this study are needed to improve material development in restorative and prosthetic dentistry and to better understand the optical properties of 3D printed materials. It will be necessary to conduct a follow-up study to determine how various printing parameters and variables, such as light source or temperature variations, affect the color stability of 3D-printed resins during post-curing processes. By using 3D-printed crown and bridge materials, a thorough study in these areas will increase the predictability and dependability of the dental treatment procedure.

CONCLUSION

Within the limitations of this study; when compared to artificial saliva, the materials were considerably discolored by different colorants. It was observed that the color change was more as the storage time increased. The material groups immersed in all solutions used on the 1st day were colored within the clinically acceptable threshold value ($\Delta E \leq 3.7$). At the end of the 7th day, all color changes in all solutions,

except for the artificial saliva, were observed to go beyond the clinical limit. 3D permanent composite resins generally showed more staining than CAD/CAM milling composite resins.

Clinical impact

To maximize the clinical effectiveness of 3D-printed restorative dental resins, it is essential to understand their optical behavior. When 3D-printed resin restorations are utilized in clinics for aesthetic reasons, particularly in the anterior region, low color stability may make patients feel dissatisfied in terms of appearance. Therefore, while prescribing 3D-printed resins to patients, clinicians need to be concerned due to their limited color stability.

Acknowledgments

Authorship contributions

Concept: NEB, ZS, CYC Design: NEB, ZS, CYC Data collection or processing: NEB, ZS, CYC, OA Analysis and interpretation: NEB, ZS, CYC, OA, MAK, Literature search: NEB, ZS, CYC, Writing: NEB, ZS, CYC.

Data availibity statement

The data that support the findings of this study are available from the corresponding author upon reasonable request.

Declaration of competing interest

There is no conflict of interest in this study.

Ethics

Since resources obtained from humans or animals were not used in this study, ethics committee approval was not obtained.

Funding

REFERENCES

1. Lee EH, Ahn JS, Lim YJ, Kwon HB, Kim MJ. Effect of post-curing time on the color stability and related properties of a tooth-colored 3D-printed resin material. J Mech Behav Biomed Mater. 2022;126:104993.

2. Miyazaki T, Hotta Y, Kunii J, Kuriyama S, Tamaki Y. A review of dental CAD/CAM: current status and future perspectives from 20 years of experience. Dent Mater J. 2009;28(1):44-56.

3. Schweiger J, Edelhoff D, Güth JF. 3D printing in digital prosthetic dentistry: An overview of recent developments in additive manufacturing. J Clin Med. 2021;10(9).

4. Bhargav A, Sanjairaj V, Rosa V, Feng LW, Fuh Yh J. Applications of additive manufacturing in dentistry: A review. J Biomed Mater Res B Appl Biomater. 2018;106(5):2058-64.

5. Monzón M, Ortega Z, Martínez A, Ortega F. Standardization in additive manufacturing: activities carried out by international organizations and projects. IJAMT. 2015;76:1111-21.

6. Sulaiman TA. Materials in digital dentistry-A review. J Esthet Restor Dent. 2020;32(2):171-81.

7. Aati S, Shrestha B, Fawzy A. Cytotoxicity and antimicrobial efficiency of ZrO2 nanoparticles reinforced 3D printed resins. Dent Mater. 2022;38(8):1432-42.

8. Atria PJ, Bordin D, Marti F, Nayak VV, Conejo J, Benalcázar Jalkh E, et al. 3D-printed resins for provisional dental restorations: Comparison of mechanical and biological properties. J Esthet Restor Dent. 2022;34(5):804-15.

9. Simoneti DM, Pereira-Cenci T, Dos Santos MBF. Comparison of material properties and biofilm formation in interim single crowns obtained by 3D printing and conventional methods. J Prosthet Dent. 2022;127(1):168-72.

10. Zimmermann M, Ender A, Egli G, Özcan M, Mehl A. Fracture load of CAD/CAM-fabricated and 3D-printed composite crowns as a function of material thickness. Clin Oral Investig. 2019;23(6):2777-84.

11. Borella PS, Alvares LAS, Ribeiro MTH, Moura GF, Soares CJ, Zancopé K, et al. Physical and mechanical properties of four 3D-printed resins at two different thick layers: An in vitro comparative study. Dent Mater. 2023;39(8):686.

12. Nam NE, Hwangbo NK, Jin G, Shim JS, Kim JE. Effects of heat-treatment methods on cytocompatibility and mechanical properties of dental products 3D-printed using photopolymerized resin. J Prosthodont Res. 2023;67(1):121-31.

13. Jin G, Gu H, Jang M, Bayarsaikhan E, Lim JH, Shim JS, et al. Influence of postwashing process on the elution of residual monomers, degree of conversion, and mechanical properties of a 3D printed crown and bridge materials. Dent Mater. 2022;38(11):1812-25.

14. Ozer NE, Sahin Z, Yikici C, Duyan S, Kilicarslan MA. Bacterial adhesion to composite resins produced by additive and subtractive manufacturing. Odontology. 2024;112(2):460-71.

15. Vichi A, Balestra D, Scotti N, Louca C, Paolone G. Translucency of CAD/CAM and 3D printable composite materials for permanent dental restorations. Polymers (Basel). 2023;15(6).

16. Espinar C, Bona AD, Pérez MM, Tejada-Casado M, Pulgar R. The influence of printing angle on color and translucency of 3D printed resins for dental restorations. Dent Mater. 2023;39(4):410-7.

17. Alharbi N, Alharbi A, Osman R. Stain susceptibility of 3D-printed nanohybrid composite restorative material and the efficacy of different stain removal techniques: An in vitro study. Materials (Basel). 2021;14(19).

18. Deligeorgi V, Mjör IA, Wilson NH. An overview of reasons for the placement and replacement of restorations. Prim Dent Care. 2001;8(1):5-11.

19. Park JK, Kim TH, Ko CC, García-Godoy F, Kim HI, Kwon YH. Effect of staining solutions on discoloration of resin nanocomposites. Am J Dent. 2010;23(1):39-42.

20. Kim JH, Lee YK, Powers JM. Influence of a series of organic and chemical substances on the translucency of resin composites. J Biomed Mater Res B Appl Biomater. 2006;77(1):21-7.

21. Mundim FM, Garcia Lda F, Pires-de-Souza Fde C. Effect of staining solutions and repolishing on color stability of direct composites. J Appl Oral Sci. 2010;18(3):249-54.

22. Alharbi N, Wismeijer D, Osman RB. Additive manufacturing techniques in prosthodontics: Where do we currently stand? A critical review. Int J Prosthodont. 2017;30(5):474–84.

23. Mostafavi D, Methani MM, Piedra-Cascón W, Zandinejad A, Att W, Revilla-León M. Influence of polymerization postprocessing procedures on the accuracy of additively manufactured dental model material. Int J Prosthodont. 2023;36(4):479-85.

24. Paravina RD, Ghinea R, Herrera LJ, Bona AD, Igiel C, Linninger M, et al. Color difference thresholds in dentistry. J Esthet Restor Dent. 2015;27:S1-S9.

25. Soares-Geraldo D, Scaramucci T, Steagall W, Jr., Braga SR, Sobral MA. Interaction between staining and degradation of a composite resin in contact with colored foods. Braz Oral Res. 2011;25(4):369-75.

26. Adawi HA, Al Mialeem MM, Al Ahmari NM, Shariff M, Qahhar MA, Muharraq SMH, et al. Assessment of color stainability of computer-aided design and computer-aided manufacturing (CAD/CAM) ceramic materials after hot and cold coffee ımmersion at different time ıntervals. Med Sci Monit. 2021;27:e932745.

27. Della Bona A, Kelly JR. The clinical success of all-ceramic restorations. JADA. 2008;139:S8-S13.

28. Joiner A. Tooth colour: a review of the literature. J Dent. 2004;32 Suppl 1:3-12.

29. Aydın N, Karaoğlanoğlu S, Oktay EA, Kılıçarslan MA. Investigating the color changes on resin-based CAD/CAM blocks. J Esthet Restor Dent. 2020;32(2):251-6.

30. Espinar Pulgar C, Della Bona A, Pérez Gómez MDM, Pulgar Encinas RM. Color and optical properties of 3D printing restorative polymer-based materials: A scoping review. J Esthet Restor Dent. 2022;34(6):853-864.

31. de Castro EF, Nima G, Rueggeberg FA, Araújo-Neto VG, Faraoni JJ, Palma-Dibb RG, et al. Effect of build orientation in gloss, roughness and color of 3D-printed resins for provisional indirect restorations. Dent Mater. 2023;39(7):e1-e11.

32. Shishehian A, Firouz F, Khazaee S, Rajabi H, Farhadian M, Niaghiha F. Evaluating the color stability of 3D-printed resins against various solutions. Eur J Transl Myol. 2023;33(3).

33. Almejrad L, Yang CC, Morton D, Lin WS. The effects of beverages and surface treatments on the color stability of 3D-printed interim restorations. J Prosthodont. 2022;31(2):165-70.

34. Atria PJ, Lagos I, Sampaio CS. In vitro evaluation of surface roughness, color stability, and color masking of provisional restoration materials for veneers and crowns. Int J Comput Dent. 2020;23(4):343-50.

35. Shin JW, Kim JE, Choi YJ, Shin SH, Nam NE, Shim JS, et al. Evaluation of the color stability of 3D-printed crown and bridge materials against various sources of discoloration: An in vitro study. Materials (Basel). 2020;13(23).

36. Seyidaliyeva A, Rues S, Evagorou Z, Hassel AJ, Rammelsberg P, Zenthöfer A. Color stability of polymer-infiltrated-ceramics compared with lithium disilicate ceramics and composite. J Esthet Restor Dent. 2020;32(1):43-50.

37. Ardu S, Braut V, Di Bella E, Lefever D. Influence of background on natural tooth colour coordinates: an in vivo evaluation. Odontology. 2014;102(2):267-71.

38. Nozaki K, Koizumi H, Horiuchi N, Nakamura M, Okura T, Yamashita K, et al. Suppression effects of dental glass-ceramics with polarization-induced highly dense surface charges against bacterial adhesion. Dent Mater J. 2015;34(5):671-8.

39. Aydın N, Topçu FT, Karaoğlanoğlu S, Oktay EA, Erdemir U. Effect of finishing and polishing systems on the surface roughness and color change of composite resins. J Clin Exp Dent. 2021;13(5):e446-e54.

40. Topcu FT, Sahinkesen G, Yamanel K, Erdemir U, Oktay EA, Ersahan S. Influence of different drinks on the colour stability of dental resin composites. Eur J Dent. 2009;3(1):50-6.

41. Güler AU, Güler E, Yücel AC, Ertaş E. Effects of polishing procedures on color stability of composite resins. J Appl Oral Sci. 2009;17(2):108-112.

42. Lee YK, Yu B, Lim HN, Lim JI. Difference in the color stability of direct and indirect resin composites. J Appl Oral Sci. 2011;19(2):154-60.

43. Seyidaliyeva A, Rues S, Evagorou Z, Hassel AJ, Rammelsberg P, Zenthöfer A. Color stability of polymer-infiltrated-ceramics compared with lithium disilicate ceramics and composite. J Esthet Restor Dent. 2020;32(1):43-50.

44. Bahannan SA. Shade matching quality among dental students using visual and instrumental methods. J Dent. 2014;42(1):48-52.

45. Kim JE, Choi WH, Lee D, Shin Y, Park SH, Roh BD, et al. Color and translucency stability of three-dimensional printable dental materials for crown and bridge restorations. Materials (Basel). 2021;14(3).

46. O'Brien WJ, Hemmendinger H, Boenke KM, Linger JB, Groh CL. Color distribution of three regions of extracted human teeth. Dent Mater. 1997;13(3):179-85.

47. Erdemir U, Yildiz E, Eren MM. Effects of sports drinks on color stability of nanofilled and microhybrid composites after long-term immersion. J Dent. 2012;40 Suppl 2:e55-63.

48. Al-Dharrab A. Effect of energy drinks on the color stability of nanofilled composite resin. J Contemp Dent Pract. 2013;14(4):704-11.

49. Duarte S, Sartori N, Phark J-H. Ceramic-reinforced polymers: CAD/CAM hybrid restorative materials. Curr. Oral Health Rep. 2016;3:198-202.

50. Paolone G, Mandurino M, De Palma F, Mazzitelli C, Scotti N, Breschi L, et al. Color stability of polymer-based composite CAD/CAM blocks: A systematic review. Polymers (Basel). 2023;15(2).

51. Espinar C, Della Bona A, Tejada-Casado M, Pulgar R, Pérez MM. Optical behavior of 3D-printed dental restorative resins: Influence of thickness and printing angle. Dent Mater. 2023;39(10):894-902.

Research Article

THE ASSOCIATIONS OF ADHERENT GINGIVAL THICKNESS IN THE BUCCAL AND PALATAL REGIONS OF THE MAXILLA AND MANDIBULA WITH AGE AND GENDER

Cem GÜNALTAY [1], Mine GEÇGELEN CESUR [1,*]

[1] Department of Orthodontics, Faculty of Dentistry, Aydın Adnan Menderes University, Aydin, TURKIYE

Correspondence: minegecgelen@hotmail.com

ABSTRACT

Objective: This study aimed to investigate gingival thickness variations regarding age, gender, and sites where mini-screws are frequently applied and to guide mini-screw size selection.

Materials and Methods: In our study, gingival thickness measurements were performed by a transgingival probing method in 224 patients who presented for examination to the Department of Orthodontics, Faculty of Dentistry, Aydın Adnan Menderes University. Fifty-six females and 56 males aged 14-20 and 21-27 years were enrolled in the study. In each individual, measurements were made from the mucogingival junction at the interdental area in the buccal mandibular and buccal maxillary regions, whereas at the interdental area within 4 mm and 8 mm distance from the gingival crest in the palatinal maxilla.

Results: Comparisons between genders indicated that gingival thickness in the buccal region of the maxilla was statistically significantly greater in males than in females (p<0.005). In age-based comparisons, gingival thickness in the buccal and palatinal regions of the maxilla in younger age group individuals was significantly less than in older age group individuals (p<0.005). Interregional comparisons revealed that gingival thickness was most significant in the molar zone in the buccal region of the mandible, in the incisor zone in the buccal region of the maxilla, in the premolar zone within 4 mm of the maxillary palatinal region, and the molar zone within 8 mm of the maxillary palatinal region.

Conclusion: Our study results suggest that the gingival thickness varies with age and gender in different mini-screw applied sites.

Keywords: Gingival thickness, maxilla, mandibula

INTRODUCTION

The gingiva is the masticatory mucosa lining the alveolar ridge and surrounding the cervical aspect of the teeth (1). Periodontal probe visualization, transgingival measurements, ultrasonic devices, direct visual inspection, transformer probing, and cone beam computed tomography can determine gingival thickness (2). In orthodontics, anchorage refers to resistance against undesired tooth movements. Anchorage planning and control are of critical importance in orthodontic management. Anchorage loss during orthodontic treatment is among the most significant complications that can be encountered. Therefore, anchorage control should be considered from initiating orthodontic treatment (3).

Mini-screws, which are among the anchorage devices, have been favored frequently in recent years for their advantages, such as providing total anchorage capacity, easy applicability, not requiring patient cooperation, their small size, their possibility to be used for anchorage purposes without waiting for osteointegration like dental implants, and their easy removal when their function is over(4-6). The sites in the mouth where mini-screws are frequently applied are the mucogingival junction in the interdental buccal area and the interdental sites 4mm and 8mm from the gingival crest in the palatinal region (7).

On the other hand, drawbacks restricting mini-screw use include complications such as inflammation of soft tissues, damage to adjacent structures, and the lack of initial stability (8-9). Many factors, including mini-screw-related, patient-related, surgical application-related, and anatomical structures-related factors, affect successful mini-screw use. The mini-screw-related factors include the mini-screw's length and shape, the mini-screw's diameter and groove structure, the material that the mini-screw is made of, and the mini-screw's surface properties. As the length, diameter, number of grooves, and distance between the grooves increase, the mini-screw's stability increases (10). Age, gender, oral hygiene, and systemic diseases are among the patient-related factors affecting the success of the mini-screw. The mini-screw loss rate is higher in patients with poor oral hygiene than those with adequate oral hygiene.

The dimensions of the mini-screws to be positioned vary based on the application sites. The bone content and gingival thickness in the application site of the mini-screw are critical factors in mini-screw selection. In cases in whom the bone content is insufficient or the gingival thickness is excessive, the mini-screw application's failure rate is higher (9). This study aimed to investigate gingival thickness variations by age, gender, and mini-screws' common application sites and also to guide the mini-screw size selection process. Our study's working hypothesis was 'There are no significant differences in the thickness of adherent gingiva among different sites, age, and gender groups concerning the mini-screw application. On the other hand, our study's alternative hypothesis was 'There are significant differences for mini-screw application among different sites, age, and gender groups regarding adherent gingival thicknesses.

MATERIALS AND METHODS

Study Sample

The present study was conducted as an analytical cross-sectional prospective study. A total of 56 male and female individuals aged 14-20 years and 56 male and female individuals aged 21-27 years, who voluntarily agreed to participate in the study and presented to Aydin Adnan Menderes University, Faculty of Dentistry, Department of Orthodontics for examination were enrolled in our study.

The sample size required to detect the difference between male and female patients was calculated using the G*Power 3.1.9.2 software and was based on the upper jaw p2m1 point measurements in the study "Soft Tissue Thickness for Placement of an Orthodontic Miniscrew Using an Ultrasonic Device" by Cha et al. (11) The effect size was determined as 0.538. For this effect size, taking the Type-1 error as 0.05, the Type-2 error as 0.20, and the female-to-male ratio as 1, it was determined that a minimum of 56 individuals were needed for each group.

The participants were informed verbally and in writing, and informed consent forms were obtained. Participants over 18 signed the informed consent form, whereas those under 18 and their parents/guardians signed it. The inclusion criteria were as follows: being between 14-27 years of age, having no systemic disease, being free of any medication that might affect periodontal tissues, having no previous orthodontic or prosthodontic treatment, not being pregnant or lactating, maintaining good oral hygiene, and not having any missing teeth except for the third molars.

On the other hand, the exclusion criteria were defined as the age not being within the 14-27 years range, presence of a systemic disease, taking any medication that would interfere with periodontal tissues, previous orthodontic or prosthodontic treatment, being pregnant or breastfeeding, lack of good oral hygiene, and missing any teeth other than the third molars. Participants who fulfilled the study criteria and agreed to participate were divided into two groups based on age distribution. The numbers of females and males were distributed equally in each group. Group 1 comprised 56 females and 56 males aged 14-20 years, and Group 2 comprised 56 females and 56 males aged 21-27.

Ethical approval was obtained from the Clinical Research Ethics Committee in Faculty of Dentistry , University of Aydin Adnan Menderes on February 24, 2021 (DHF2021/06). Taking the regions shown in the study by Papadopoulos and Tarawneh as a reference, measurements were made in the maxillary buccal, mandibular buccal, and maxillary palatal regions, respectively (7). Table 1   show the buccal and palatal measurement sites. All measurements were performed by the same observer (C.G.). Regarding the measurement process, first, the measurement sites were topically anesthetized with Vemcaine spray containing 10% lidocaine (Vem İlaç, Istanbul).

Table 1. Measurement sites in the buccal regions of the maxilla, mandibula and in the palatinal regions of the maxilla

Maxilla	
B-11-21	adherent gingiva adjacent to the mucogingival junction in the interradicular area of the right central and left central tooth
B-11-12	adherent gingiva adjacent to the mucogingival junction in the interradicular area of the right central and right lateral tooth
B-12-13	adherent gingiva adjacent to the mucogingival junction in the right lateral and interradicular area of the right canine tooth
B-13-14	adherent gingiva adjacent to the mucogingival junction in the interradicular area of the right canine and right 1st premolar
B-14-15	adherent gingiva adjacent to the mucogingival junction in the interradicular area of the right 1st and right 2nd premolars
B-15-16	adherent gingiva adjacent to the mucogingival junction in the interradicular area of the right 2nd premolar and 1st molar
B-16-17	adherent gingiva adjacent to the mucogingival junction in the interradicular area of the right 1st molar and right 2nd molar
B-21-22	adherent gingiva adjacent to the mucogingival junction in the interradicular area of the left central and left lateral tooth
B-22-23	adherent gingiva adjacent to the mucogingival junction in the interradicular area of the left lateral and left canine teeth
B-23-24	adherent gingiva adjacent to the mucogingival junction in the interradicular area of the left canine and left 1st premolar
B-24-25	adherent gingiva adjacent to the mucogingival junction in the interradicular area of the left 1st and 2nd premolars
B-25-26	adherent gingiva adjacent to the mucogingival junction in the interradicular area of the left 2nd premolar and left 1st molar
B-26-27	adherent gingiva adjacent to the mucogingival junction in the interradicular area of the left 1st and 2nd molars
Mandibula	
B-31-41	adherent gingiva adjacent to the mucogingival junction in the interradicular area of the right central and left central tooth
B-31-32	adherent gingiva adjacent to the mucogingival junction in the interradicular area of the left central and left lateral tooth
B-32-33	adherent gingiva adjacent to the mucogingival junction in the interradicular area of the left lateral and left canine teeth
B-33-34	adherent gingiva adjacent to the mucogingival junction in the interradicular area of the left canine and left 1st premolar
B-34-35	adherent gingiva adjacent to the mucogingival junction in the interradicular area of the left 1st and 2nd premolars
B-35-36	adherent gingiva adjacent to the mucogingival junction in the interradicular area of the left 2nd premolar and left 1st molar
B-36-37	adherent gingiva adjacent to the mucogingival junction in the interradicular area of the left 1st molar and left 2nd molar
B-41-42	adherent gingiva adjacent to the mucogingival junction in the interradicular area of the right central and right lateral teeth
B-42-43	adherent gingiva adjacent to the mucogingival junction in the interradicular area of the right lateral and right canine teeth
B-43-44	adherent gingiva adjacent to the mucogingival junction in the interradicular area of the right canine and right 1st premolar
B-44-45	adherent gingiva adjacent to the mucogingival junction in the interradicular area of the right 1st and 2nd premolars
B-45-46	adherent gingiva adjacent to the mucogingival junction in the interradicular area of the right 2nd premolar and 1st molar
B-46-47	adherent gingiva adjacent to the mucogingival junction in the interradicular area of the right 1st molar and right 2nd molar
4 mm from the gingival crest in the palatinal regions of the maxilla	
P4-11-21	mucosa at a distance of 4 mm from the gingival crest in the interradicular area of the right central and left central tooth
P4-11-12	mucosa at a distance of 4 mm from the gingival crest in the interradicular area of the right central and right lateral tooth
P4-12-13	mucosa at a distance of 4 mm from the gingival crest in the interradicular area of the right lateral and right canine tooth
P4-13-14	mucosa 4 mm from the gingival crest in the interradicular area of the right canine and right 1st premolar
P4-14-15	mucosa at a distance of 4 mm from the gingival crest in the interradicular area of the right 1st and right 2nd premolars
P4-15-16	mucosa 4 mm from the gingival crest in the interradicular area of the right 2nd premolar and right 1st molar
P4-16-17	mucosa 4 mm from the gingival crest in the interradicular area of the right 1st molar and right 2nd molar
P4-21-22	mucosa 4 mm from the gingival crest in the interradicular area of the left central and left lateral tooth
P4-22-23	mucosa at a distance of 4 mm from the gingival crest in the interradicular area of the left lateral and left canine tooth
P4-23-24	mucosa 4 mm from the gingival crest in the interradicular area of the left canine and left 1st premolar
P4-24-25	mucosa at a distance of 4 mm from the gingival crest in the interradicular area of the left 1st and left 2nd premolar teeth
P4-25-26	mucosa 4 mm from the gingival crest in the interradicular area of the left 2nd premolar and left 1st molar
P4-26-27	mucosa 4 mm from the gingival crest in the interradicular area of the left 1st molar and left 2nd molar
8 mm from the gingival crest in the palatinal regions of the maxilla	
P8-11-21	mucosa at a distance of 8 mm from the gingival crest in the interradicular area of the right central and left central tooth
P8-11-12	mucosa at a distance of 8 mm from the gingival crest in the interradicular area of the right central and right lateral tooth
P8-12-13	mucosa at a distance of 8 mm from the gingival crest in the interradicular area of the right lateral and right canine tooth
P8-13-14	mucosa 8 mm from the gingival crest in the interradicular area of the right canine and right 1st premolar
P8-14-15	mucosa at a distance of 8 mm from the gingival crest in the interradicular area of the right 1st and right 2nd premolars
P8-15-16	mucosa 8 mm from the gingival crest in the interradicular area of the right 2nd premolar and right 1st molar
P8-16-17	mucosa 8 mm from the gingival crest in the interradicular area of the right 1st molar and right 2nd molar
P8-21-22	mucosa 8 mm from the gingival crest in the interradicular area of the left central and left lateral tooth
P8-22-23	mucosa at a distance of 8 mm from the gingival crest in the interradicular area of the left lateral and left canine tooth
P8-23-24	mucosa 8 mm from the gingival crest in the interradicular area of the left canine and left 1st premolar
P8-24-25	mucosa at a distance of 8 mm from the gingival crest in the interradicular area of the left 1st and left 2nd premolar teeth
P8-25-26	mucosa 8 mm from the gingival crest in the interradicular area of the left 2nd premolar and left 1st molar
P8-26-27	mucosa 8 mm from the gingival crest in the interradicular area of the left 1st molar and left 2nd molar

After anesthesia, the endodontic spreader # 15 (Güvenç Dental, Istanbul) was placed at the determined points perpendicular to the gingiva and passively advanced until the bone was contacted. After the silicone

rondel on the spreader was contacted with the gingiva with the help of a dental tweezer, the endodontic spreader was carefully removed from the gingiva to prevent the silicone rondel's movement. After calibrating before the measurements and setting in mm., the digital caliper (Mitutoyo Cihaz, İzmir) was used to measure the distance from the end of the spreader to the silicone rondel. The measurements were recorded in the file created using Microsoft Excel software and based on the patient's gender and age.

Statistical Analysis

It was found that the p2m1 distance had to be re-measured in at least 18.4 images to test the hypotheses H0: $\varrho=0.70$ and H1: $\varrho=0.90$ at the type 1 error level of 0.05 and type 2 error level of 0.20 to assess intra-observer agreement (12). Therefore, the pre-treatment measurements of 19 randomly selected patients were evaluated a second time 10 days after the first evaluation. Shapiro-Wilk's test examined the conformity of all adherent gingival thickness measurements to a normal distribution, and these measurements were summarized as mean±ss and median (interquartile range-IQR: first quartile-third quartile). The level of intraobserver agreement for the adherent gingival thickness measurements was evaluated with the intraclass correlation coefficient (ICC). ICC was obtained from a two-way mixed model for absolute agreement and single measurement—a ICC value of 0.90 as excellent agreement (13). Differences in gingival thicknesses according to gender and age group were analyzed by independent two-sample t-test or Mann-Whitney U test. The measurements of the buccal and palatinal surfaces of the canine, premolar, and molar regions in the lower and upper jaw were obtained by averaging the gingival thicknesses of the relevant regions and surfaces and compared by repeated measures ANOVA. Huynh-Feldt correction was applied since the buccal surface gingival thickness measurements of canine, premolar, and molar regions in the mandible did not meet the sphericity assumption. LSD was used as a post-hoc test for multiple comparisons of the regions' gingival thicknesses. The statistical significance level of $p \leq 0.05$ was considered. IBM SPSS Statistics 22.0 (IBM Corp. Released 2013. IBM SPSS Statistics for Windows, Version 22.0. Armonk, NY: IBM Corp.) software package was used.

RESULTS

Comparison Results by Gender

The ICC values for adherent gingival thickness measurements ranged between 0.940 and 0.999. The intraobserver compliance levels for these measurements were excellent at all measurement sites (p<0.001). It was observed that the gingival thickness at points B-45-46, B-46-47, and B-36-37 was statistically significantly greater in males as compared to females (p<0.05), whereas no statistically significant inter-gender difference was observed regarding gingival thickness at other points (p>0.05). The distribution of the measurements

made at a distance of 4 mm from the gingiva in the palatal region of the maxilla by gender is presented in Table 2. Based on these results, no statistically significant difference was found between the two genders regarding the gingival thicknesses in the palatinal region of the maxilla (p>0.05).

Table 2. Comparison of gingival thicknesses at a distance of 4 mm and 8 mm from the gingival margin in the palatinal region of the maxilla by gender

	Distance of 4 mm from the gingival margin			
	Males (n=112)	**Females (n=112)**	**Comparison Results**	
Measurement Site	Mean±SD Median (IQR)	Mean±SD Median (IQR)	t/Z	p-value
P4-11-21	2.42±0.20 2.43 (2.31-2.55)	2.44±0.22 2.43 (2.29-2.62)	0.700	0.485
P4-11-12	2.66±0.20 2.64 (2.53-2.79)	2.64±0.24 2.65 (2.46-2.83)	0.467	0.641
P4-12-13	2.79±0.20 2.79 (2.67-2.92)	2.75±0.18 2.74 (2.64-2.86)	1.617	0.107
P4-13-14	3.22±0.25 3.23 (3.03-3.39)	3.23±0.21 3.21 (3.08-3.39)	0.229	0.819
P4-14-15	3.28±0.22 3.28 (3.10-3.42)	3.24±0.23 3.27 (3.08-3.39)	1.115	0.266
P4-15-16	2.83±0.16 2.84 (2.72-2.93)	2.84±0.2 2.85 (2.72-2.98)	0.367	0.714
P4-16-17	2.57±0.24 2.61 (2.42-2.72)	2.55±0.26 2.58 (2.35-2.72)	Z=0.600	0.548
P4-21-22	2.66±0.20 2.66 (2.54-2.79)	2.64±0.24 2.65 (2.47-2.81)	0.606	0.545
P4-22-23	2.79±0.21 2.78 (2.65-2.94)	2.75±0.19 2.75 (2.64-2.85)	1.433	0.153
P4-23-24	3.22±0.25 3.24 (3.05-3.37)	3.22±0.21 3.21 (3.08-3.39)	0.129	0.897
P4-24-25	3.28±0.21 3.26 (3.10-3.45)	3.24±0.23 3.27 (3.09-3.4)	1.142	0.255
P4-25-26	2.82±0.17 2.85 (2.71-2.93)	2.84±0.2 2.85 (2.70-3.00)	Z=0.845	0.398
P4-26-27	2.56±0.24 2.60 (2.40-2.75)	2.55±0.26 2.59 (2.35-2.73)	Z=0.467	0.640
	Distance of 8 mm from the gingival margin			
	Males (n=112)	**Females (n=112)**	**Comparison Result**	
Measurement Site	**Mean±SD Median (IQR)**	**Mean±SD Median (IQR)**	**t/Z**	**p-value**
P8-11-21	2.29±0.17 2.32 (2.18-2.40)	2.16±0.18 2.16 (2.02-2.31)	Z=5.674	**<0.001***
P8-11-12	2.69±0.18 2.69 (2.55-2.85)	2.64±0.23 2.65 (2.45-2.80)	2.005	**0.046***
P8-12-13	2.80±0.20 2.85 (2.65-2.95)	2.77±0.20 2.75 (2.65-2.94)	Z=0.950	0.342
P8-13-14	3.42±0.18 3.45 (3.30-3.51)	3.46±0.22 3.45 (3.31-3.65)	Z=1.631	0.103
P8-14-15	3.52±0.19 3.52 (3.42-3.69)	3.52±0.22 3.54 (3.37-3.65)	0.144	0.885
P8-15-16	3.46±0.16 3.45 (3.35-3.60)	3.47±0.18 3.45 (3.35-3.59)	Z=0.639	0.523
P8-16-17	3.89±0.19 3.85 (3.75-4.03)	3.85±0.17 3.85 (3.75-3.95)	1.358	0.176
P8-21-22	2.70±0.18 2.70 (2.56-2.85)	2.64±0.24 2.65 (2.47-2.81)	1.987	**0.048***
P8-22-23	2.81±0.21 2.82 (2.65-2.95)	2.77±0.20 2.78 (2.68-2.91)	1.283	0.201
P8-23-24	3.44±0.20 3.44 (3.31-3.60)	3.47±0.22 3.48 (3.30-3.64)	0.845	0.399
P8-24-25	3.54±0.20 3.54 (3.42-3.71)	3.53±0.21 3.53 (3.38-3.68)	0.529	0.598
P8-25-26	3.46±0.17 3.45 (3.35-3.6)	3.48±0.18 3.46 (3.37-3.59)	0.674	0.501
P8-26-27	3.89±0.20 3.89 (3.75-4.03)	3.87±0.18 3.88 (3.74-3.98)	0.960	0.338

SD: Standard Deviation, IQR: Interquartile Range. Inter-gender significance levels according to Mann Whitney U test or independent two-sample t-test results; *p<0.05 significance level

The distribution of the measurements taken 8 mm from the gingiva in the maxillary palatinal region by gender is listed in Table 2. Gingival thicknesses at points P8-11-21, P8-11-12, and P8-21-22 were statistically significantly higher in males than females (p<0.05); however, at other points, no statistically significant male-female difference was observed regarding gingival thickness (p>0.05). Except for measurement site B-25-26, the gingival thickness was statistically significantly higher in males than females in all other measurements (p<0.001 for all measurements).

Comparison Results by Age

Table 3. Comparison of gingival thicknesses at a distance of 4 mm and 8 mm from the gingival margin in the maxillary palatinal region by age groups

Measurement Site	Younger Age Group (n=112) Mean±SD Median (IQR)	Older Age Group (n=112) Mean±SD Median (IQR)	t/Z	p-value
Distance of 4 mm from the gingival margin			
P4-11-21	2.33±0.19	2.53±0.19	8.054	<0.001
	2.33 (2.18-2.46)	2.54 (2.38-2.65)		
P4-11-12	2.57±0.20	2.73±0.21	6.075	<0.001
	2.57 (2.45-2.67)	2.74 (2.58-2.89)		
P4-12-13	2.75±0.20	2.79±0.18	1.463	0.145
	2.74 (2.62-2.90)	2.80 (2.67-2.91)		
P4-13-14	3.10±0.20	3.34±0.20	9.195	<0.001
	3.12 (2.97-3.23)	3.34 (3.20-3.49)		
P4-14-15	3.15±0.19	3.37±0.19	8.490	<0.001
	3.13 (3.04-3.30)	3.39 (3.25-3.52)		
P4-15-16	2.77±0.16	2.90±0.17	5.885	<0.001
	2.77 (2.66-2.89)	2.89 (2.77-3.01)		
P4-16-17	2.43±0.22	2.69±0.20	Z=8.352	<0.001
	2.44 (2.28-2.58)	2.70 (2.59-2.81)		
P4-21-22	2.57±0.20	2.73±0.21	5.965	<0.001
	2.58 (2.43-2.69)	2.75 (2.58-2.89)		
P4-22-23	2.75±0.21	2.79±0.19	1.419	0.157
	2.74 (2.64-2.91)	2.80 (2.65-2.92)		
P4-23-24	3.11±0.20	3.34±0.20	8.747	<0.001
	3.11 (2.97-3.24)	3.33 (3.20-3.47)		
P4-24-25	3.15±0.19	3.37±0.19	8.523	<0.001
	3.15 (3.04-3.30)	3.39 (3.25-3.50)		
P4-25-26	2.77±0.17	2.89±0.18	Z=5.209	<0.001
	2.76 (2.66-2.9)	2.90 (2.80-3.02)		
P4-26-27	2.43±0.23	2.68±0.21	Z=8.039	<0.001
	2.45 (2.29-2.58)	2.70 (2.60-2.80)		
Distance of 8 mm from the gingival margin			
P8-11-21	1.17±0.15	1.22±0.18	t=2.373	0.019*
	1.16 (1.06-1.28)	1.23 (1.10-1.38)		
P8-11-12	1.59±0.18	1.63±0.21	1.520	0.129
	1.61 (1.47-1.73)	1.65 (1.49-1.80)		
P8-12-13	1.29±0.16	1.35±0.17	2.599	0.009*
	1.28 (1.18-1.39)	1.33 (1.22-1.51)		
P8-13-14	1.10±0.13	1.23±0.15	t=6.849	<0.001*
	1.11 (1.02-1.19)	1.24 (1.13-1.33)		
P8-14-15	1.14±0.16	1.25±0.16	5.297	<0.001*
	1.16 (1.02-1.25)	1.30 (1.13-1.37)		
P8-15-16	1.03±0.14	1.20±0.17	7.146	<0.001*
	1.04 (0.92-1.13)	1.23 (1.09-1.33)		
P8-16-17	1.04±0.16	1.07±0.15	1.960	0.050
	1.05 (0.95-1.15)	1.11 (0.99-1.18)		
P8-21-22	1.58±0.18	1.62±0.20	1.487	0.137
	1.60 (1.45-1.71)	1.64 (1.49-1.8)		
P8-22-23	1.28±0.16	1.35±0.17	2.667	0.008*
	1.25 (1.15-1.37)	1.34 (1.24-1.5)		
P8-23-24	1.10±0.13	1.23±0.15	6.725	<0.001*

	1.13 (1.03-1.18)	1.25 (1.13-1.34)		
P8-24-25	1.14±0.17	1.26±0.15	5.599	<0.001*
	1.15 (1.03-1.25)	1.29 (1.16-1.37)		
P8-25-26	1.06±0.13	1.07±0.13	0.802	0.423
	1.05 (0.95-1.15)	1.10 (0.99-1.15)		
P8-26-27	1.03±0.14	1.09±0.14	3.360	0.001*
	1.05 (0.95-1.14)	1.12 (0.99-1.17)		

SD: Standard Deviation, IQR: Interquartile Range

Accordingly, at sites B-44-45, B-34-35, and B-31-32, the gingival thickness was statistically significantly higher in the individuals of the older age group compared to those of the younger age group (p<0.05); yet, there were no significant differences between the older and younger age groups (p>0.05) in the measurements taken at other sites. The distributions of the measurements obtained from the sites 4 mm from the gingiva in the maxillary palatinal regions by age groups are presented in Table 3. Except for the sites P4-12-13 and P4-22-23, the gingival thickness measurements of the older age group were significantly higher than those of the younger age group (p<0.001). The distributions of the measurements made at a distance of 8 mm from the gingival margin in the maxillary palatinal region by age group are presented in Table 3.

Table 4. Comparison of gingival thickness in the maxillary buccal region by the age groups.

Measurement Site	Younger Age Group (n=112) Mean±SD Median (IQR)	Older Age Group (n=112) Mean±SD Median (IQR)	Comparison result t/Z	p-value
B-11-21	1.17±0.15	1.22±0.18	t=2.373	**0.019***
	1.16 (1.06-1.28)	1.23 (1.10-1.38)		
B-11-12	1.59±0.18	1.63±0.21	1.520	0.129
	1.61 (1.47-1.73)	1.65 (1.49-1.80)		
B-12-13	1.29±0.16	1.35±0.17	2.599	**0.009***
	1.28 (1.18-1.39)	1.33 (1.22-1.51)		
B-13-14	1.10±0.13	1.23±0.15	t=6.849	**<0.001***
	1.11 (1.02-1.19)	1.24 (1.13-1.33)		
B-14-15	1.14±0.16	1.25±0.16	5.297	**<0.001***
	1.16 (1.02-1.25)	1.30 (1.13-1.37)		
B-15-16	1.03±0.14	1.20±0.17	7.146	**<0.001***
	1.04 (0.92-1.13)	1.23 (1.09-1.33)		
B-16-17	1.04±0.16	1.07±0.15	1.960	0.050
	1.05 (0.95-1.15)	1.11 (0.99-1.18)		
B-21-22	1.58±0.18	1.62±0.20	1.487	0.137
	1.60 (1.45-1.71)	1.64 (1.49-1.8)		
B-22-23	1.28±0.16	1.35±0.17	2.667	**0.008***
	1.25 (1.15-1.37)	1.34 (1.24-1.5)		
B-23-24	1.10±0.13	1.23±0.15	6.725	**<0.001***
	1.13 (1.03-1.18)	1.25 (1.13-1.34)		
B-24-25	1.14±0.17	1.26±0.15	5.599	**<0.001***
	1.15 (1.03-1.25)	1.29 (1.16-1.37)		
B-25-26	1.06±0.13	1.07±0.13	0.802	0.423
	1.05 (0.95-1.15)	1.10 (0.99-1.15)		
B-26-27	1.03±0.14	1.09±0.14	3.360	**0.001***
	1.05 (0.95-1.14)	1.12 (0.99-1.17)		

SD: Standard Deviation, IQR: Interquartile Range

Except for the P8-11-12, P8-16-17, P8-21-22, and P8-25-26 sites, the older age group's gingival thickness measurements were statistically significantly higher than those of the younger age group (p<0.05). The distributions of gingival thicknesses obtained from the maxillary buccal regions by age group are shown in Table 4. Except for B-11-12, B-16-17, B-21-22, and B-25-26 sites, the gingival thicknesses were statistically significantly higher in the older age group than in the younger age group (p<0.05).

Comparison Results by Regions

The distribution of gingival thicknesses in the incisor, premolar, and molar regions by the measurement sites is presented in Table 5. The mean gingival thicknesses of all three regions were statistically significantly different from each other (p<0.001). The mean gingival thicknesses obtained from the mandibular buccal surfaces were 1.14±0.07 mm in the canine region, whereas 1.10±0.11 mm in the premolar region and 1.20±0.09 mm in the molar region. Thus, the maximum gingival thickness was recorded in the molar region and the minimum in the premolar region.

Table 5. Distributions of gingival thicknesses by regions located in buccal (mandibular and maxillary) and palatinal (4 mm and 8 mm) surfaces

Surface	Canine Mean±SD Median (IQR)	Premolar Mean±SD Median (IQR)	Molar Mean±SD Median (IQR)	Comparison result F	Comparison result p-value
Mandibular buccal	1.14±0.07	1.10±0.11	1.20±0.09	77.295	**<0.001[*,1]**
	1.14 (1.10-1.19)	1.10 (1.03-1.19)	1.21 (1.15-1.26)		
Palatinal 4mm	2.65±0.13	3.24±0.18	2.69±0.17	1291.847	**<0.001[*]**
	2.65 (2.57-2.74)	3.24 (3.11-3.38)	2.7 (2.58-2.82)		
Palatinal 8mm	2.63±0.13	3.49±0.16	3.67±0.14	4864.306	**<0.001[*]**
	2.63 (2.53-2.73)	3.50 (3.36-3.63)	3.69 (3.55-3.78)		
Maxillary buccal	1.41±0.14	1.18±0.13	1.07±0.13	600.937	**<0.001[*]**
	1.40 (1.30-1.53)	1.17 (1.10-1.28)	1.08 (0.97-1.16)		

SD: Standard Deviation, IQR: Interquartile Range , *P≤0.001 was obtained in all regional pairwise comparisons. The result with Huynh-Feldt correction is given.

DISCUSSION

This study evaluated the variations of the adherent gingival thickness in the buccal and palatinal regions of the maxilla and mandible regarding different age and gender groups. Regarding gender difference, the study found that gingival thickness in the maxillary buccal region was thicker in males than in females. However, In the measurements made in the mandibular buccal region and the maxillary palatinal region at distances of 4 mm and 8 mm from the gingival crest, there were no overall differences in gingival thickness between the genders. Regarding the effect of age, the study found that gingival thicknesses in the maxillary palatinal and buccal regions were more significant in the older age group than in younger age group individuals. However, there was no difference between the older and younger age groups regarding gingival thickness in the mandibular buccal region. Regarding the regional effects, the highest gingival thickness for the molars was in the mandibular buccal region, whereas for the incisors, in the maxillary buccal region. For

palatinal gingival thicknesses, the thickest gingiva located 4 mm from the gingival crest belonged to the premolars region, and the thickest gingiva located 8 mm from the gingival crest belonged to the molars.

Inter-gender Comparisons

Our study revealed no inter-gender difference regarding anterior gingival thickness in the mandibular buccal region. Many studies have evaluated gender-related changes in gingival biotypes in the literature(11,14-16). Alkan et al. evaluated gingival thickness variations in the anterior mandibular region by gender and age in 171 individuals (108 females and 63 males) and reported that the gingival thickness was 0.70±0.15 mm in females and 0.77±0.19 mm in males (14). Vandana and Savitha reported the gingival thickness in the anterior mandibular region in 16 females and 16 males as 1.02±0.33 mm in females and 1.11±0.35 mm in males (15). These studies used the transgingival probing method and reported no inter-gender difference. Our study was consistent with these studies regarding the method and the result.

Contrary to our study, in the study by Zawawi et al., the anterior mandibular gingival thickness was evaluated by periodontal probing in 142 individuals (64 males and 78 females) (16). Their study reported thinner gingiva in females than in males. The reason for the difference between the results of their study and ours might be the different gingival thickness measurement techniques in the two studies. Cha et al. evaluated the gingival thickness variations in the maxilla and mandible in 61 individuals (28 males and 33 females) with an ultrasonic device (11). They found that the gingival thickness changes in the posterior mandibular buccal region concerning gender were not significant. Our study found no statistically significant difference between genders at all sites except for three points. It has been reported that gingival thickness measurement with ultrasonic devices is reliable in the anterior regions but not in the posterior locations because of the difficulty of placing the device (17). It is thought that the difference between the two studies might have been due to differences between the measurement techniques and racial distributions.

Age Group-Based Comparisons

Vandana and Savitha evaluated gingival thickness in the anterior mandibular buccal region in 16 males and 16 females aged 16-38 years and reported that gingival thickness was more significant in the younger age group than in the older age group (15). The reason for the difference between this study and ours might have been racial, genetic, and age-group differences. Alkan et al. evaluated age-related alterations of gingival thickness in the anterior mandibular region in individuals under and over 18; the difference between the two age groups was insignificant, consistent with our study (14).

Alhajj et al. evaluated gingival thickness variations in the posterior maxillary buccal region in 456 individuals (18). Their study's age groups were determined as under and over 25 years. They found that the difference between age groups regarding gingival thickness was not statistically significant. As the reason for

the difference from our findings, we think that Alhajj had a vast age range in his study. While our study's spreader measurements were made with a digital caliper, Alhajj et al. used a periodontal probe. The literature has reported that the measurement sensitivity of the periodontal probe was low (17).   Another reason for the difference between their and our results might be the difference in measurement methods.

Inter-Regional Comparisons

Cha et al. compared gingival thickness among regions with the ultrasonic measurement method, and consistent with our study, they found that gingival thickness in the mandibular buccal region was highest in the molar region and lowest in the premolar region, while gingival thickness in the maxillary buccal region was highest in the incisor region and lowest in the molar region (11). Similar to the results of our study, they reported that the maximum gingival thickness was in the posterior palatinal region in the measurements made 8 mm from the gingival crest. However, contrary to our study, the mean gingival thickness in the palatinal region at a distance of 4 mm from the gingival crest was the highest in the anterior region. We think that the difference of their findings from the present study might occur because the gingival thickness in the rugae region might have been affected by individual factors such as genetic factors and oral hygiene.

In another study by Parmar et al., the gingival thickness was compared among regions using the ultrasonic measurement method in 32 individuals (9). It was determined that the gingival thickness in the mandibular buccal region was the highest in the molar region and the lowest in the premolar region, whereas the incisors had the thickest gingivae in the maxillary buccal region. Those results were compatible with our study's results.

CONCLUSION

In conclusion, our study's initial hypothesis was rejected and alternative hypothesis   was approved. This study will contribute to the literature due to the high number of patients evaluated, including the comparison of age and gender, the use of a measurement technique that the clinician can practically apply before mini-screw application with a simple endodontic instrument in clinical settings. It may help in the stability of the mini screws to be applied in the maxillary buccal region to choose more extended sizes in male patients than in female patients. However, gender is not a determining factor in selecting the mini-screw size to be applied in the mandibular buccal region and the maxillary palatinal regions at distances of 4 mm and 8 mm from the gingival crest. Regarding the size of the mini-screw to be applied in the maxillary palatinal region, we recommend longer mini-screw sizes in older age groups compared to younger age group individuals. Since gingival thickness might be affected by numerous factors, particularly racial and genetic ones, more research is needed to enrich the literature and enable using guidelines in clinical practice.

Declaration of competing interest

The authors have no conflicts of interest to declare.

Ethics

The decision of Aydin Adnan Menderse University Faculty of Dentistry Clinical Research Ethics Committee 2021/06, dated February 24, 2021, was obtained.

REFERENCES

1. Bartold PM, Walsh LJ, Narayanan AS. Molecular and cell biology of the gingiva. Periodontol 2000. Oct 2000;24:28-55.

2. Zweers J, Thomas RZ, Slot DE, Weisgold AS, Van der Weijden FG. Characteristics of periodontal biotype, its dimensions, associations and prevalence: a systematic review. J Clin Periodontol. Oct 2014;41(10):958-971.

3. Ülgen M. Ortodontik tedavi prensipleri. Ankara: Ankara Üniversitesi Basımevi; 1983.

4. Kuroda S, Sugawara Y, Deguchi T, Kyung HM, Takano-Yamamoto T. Clinical use of miniscrew implants as orthodontic anchorage: success rates and postoperative discomfort. Am J Orthod Dentofacial Orthop. Jan 2007;131(1):9-15.

5. Melsen B. Mini-implants: Where are we? J Clin Orthod. Sep 2005;39(9):539-547; quiz 531-532.

6. Park HS, Kwon TG. Sliding mechanics with microscrew implant anchorage. Angle Orthod. Oct 2004;74(5):703-710.

7. Papadopoulos MA, Tarawneh F. The use of miniscrew implants for temporary skeletal anchorage in orthodontics: a comprehensive review. Oral Surg Oral Med Oral Pathol Oral Radiol Endod. May 2007;103(5):e6-15.

8. Papageorgiou SN, Zogakis IP, Papadopoulos MA. Failure rates and associated risk factors of orthodontic miniscrew implants: a meta-analysis. Am J Orthod Dentofacial Orthop. Nov 2012;142(5):577-595 e577.

9. Parmar R, Reddy V, Reddy SK, Reddy D. Determination of soft tissue thickness at orthodontic miniscrew placement sites using ultrasonography for customizing screw selection. Am J Orthod Dentofacial Orthop. Oct 2016;150(4):651-658.

10. Wilmes B, Drescher D. Impact of insertion depth and predrilling diameter on primary stability of orthodontic mini-implants. Angle Orthod. Jul 2009;79(4):609-614.

11. Cha BK, Lee YH, Lee NK, Choi DS, Baek SH. Soft tissue thickness for placement of an orthodontic miniscrew using an ultrasonic device. Angle Orthod. May 2008;78(3):403-408.

12. Walter SD, Eliasziw M, Donner A. Sample size and optimal designs for reliability studies. Stat Med. Jan 15 1998;17(1):101-110.

13. Portney LG, Watkins MP. Foundations of clinical research: applications to practice Upper Saddle River, N. J.: Pearson/Prentice Hall; 2015.

14. Alkan EA, Alkan Ö, Kaya Y, Keskin S. Alt ve Üst Çene Ön Bölge Diş Eti Kalınlığının Cinsiyet ve Yaşla Olan İlişkisinin Değerlendirilmesi. Türkiye Klinikleri Diş Hekimliği Bilimleri Dergisi. 2016;22(3):157-162.

15. Vandana KL, Savitha B. Thickness of gingiva in association with age, gender and dental arch location. J Clin Periodontol. Jul 2005;32(7):828-830.

16. Zawawi KH, Al-Zahrani MS. Gingival biotype in relation to incisors' inclination and position. Saudi Med J. Nov 2014;35(11):1378-1383.

17. Wang J, Cha S, Zhao Q, Bai D. Methods to assess tooth gingival thickness and diagnose gingival phenotypes: A systematic review. J Esthet Restor Dent. Jun 2022;34(4):620-632.

18. Alhajj WA. Gingival phenotypes and their relation to age, gender and other risk factors. BMC Oral Health. Mar 25 2020;20(1):87.

Research Article

EVALUATING THE MARGINAL FIT OF GALVANOCERAMIC INLAYS: IS IT CLINICALLY ACCEPTABLE?

Özlem ÇÖLGEÇEN [1, *], Zekiye EROĞLU [2], Ayşegül GÜLERYÜZ [3]

[1] 1 Department of Prosthodontics, Faculty of Dentistry, Izmir Kâtip Celebi University, Izmir, TURKIYE
[2] Department of Prosthodontics, Faculty of Dentistry, Nevşehir Hacı Bektaş Veli Univercity, Nevşehir, TURKIYE
[3] Department of Prosthodontics, Faculty of Dentistry, Erciyes University, Kayseri, TURKIYE
Correspondence: ozlemalan@yahoo.com

ABSTRACT

Aim: The aim of this study was to investigate the marginal adaptation of galvanoceramic inlay comparing two different ceramic inlays used in dental practice.

Materials and methods: Class II inlay cavity was prepared on an ivorine mandibular left first molar and a metal master die was produced from stainless steel. Using electroforming machine, fifteen galvanoformed copings were produced firstly, and then galvanoceramic inlays were obtained by firing feldspathic porcelain on them. For comparison with ceramic inlays, two different groups were prepared from lithium disilicate and alumina ceramic. The absolute marginal discrepancy of galvanoformed copings and three different inlay restorations were measured onto the master die in described 16 different reference points by scanning electron microscope. Data obtained from the measurements were statistically analysed using paired t-test and two-way analyses of variance (α=.05).

Results: The galvanoceramic inlays showed a significantly higher marginal discrepancy than other ceramic inlays (P<.001). The mean marginal discrepancy was 379±153µm for galvanoceramic inlays, whereas other inlays had marginal gaps under 200µm. Galvanoformed copings had lowest marginal gap, but the adaptation of these copings was failed after porcelain firing.

Conclusion: Galvanoformed copings have superior marginal fit than other ceramic inlays, but the marginal gaps increased after porcelain firing and marginal adaptations became clinically unacceptable. Clinical usage of galvanoceramic inlays is questionable due to their marginal discrepancies.

Keywords: Inlay; Marginal Discrepancy; Galvanoceramic; Electroforming

INTRODUCTION

Ideally, dental restorations should provide an excellent marginal fit to ensure their long-term success. Poor marginal fit increases the potential for microleakage and plaque retention, which in turn elevates the risk of recurrent caries and periodontal disease (1,2). The marginal fits of inlay/onlay and partial crown restorations are more critical than that of full crown restorations because they have longer margins than the crowns. Therefore, factors affecting the marginal fit of these restorations should be evaluated to achieve desirable clinical outcomes. Many studies have indicated that restoration material and fabrication techniques affect marginal integrity, leading to dimensional changes in the final restoration (3,4). Even the marginal integrity of the restoration may become clinically unacceptable due to these dimensional changes.

Minimal invasive approach in dentistry has resulted in the development of numerous ceramic inlay systems. To produce ceramic inlays, there are both conventional methods such as using pressable ceramics and modern methods such as computer aided design and manufacturing system (CAD/CAM)(3,4). Additionally, there is also galvanoceramic restoration manufacturing technology which incorporates the positive properties of both gold and ceramics (5,6). CAD/CAM systems have become widespread today, but they cannot offer the positive effects that gold can provide at the restoration margin. Gold, a noble metal, is known for high chemical resistance and reduces microorganism adhesion to surface due to its oligodynamic effect and reduces microleakage in margins due to its burnishable structure. The incidence of microleakage and marginal caries is lower in gold restorations compared to others because of these favourable properties. However, gold inlays are losing their widespread usage in today dentistry due to the increase in gold prices and its yellow appearance. However, this does not change the fact that it is biologically more advantageous.

Galvano ceramic restoration manufacturing technology uses electroforming system that combines porcelain and gold, so making both aesthetic and hygienic restorations possible. Since the amount of gold used is not too much, it does not increase the cost excessively. According to literature, galvanized gold has a range of advantages such as biocompatibility, endurance, aesthetic appearance of warm yellow hue of pure gold, bacteriostatic features, better periodontal health, energy saving of electroplating (less than 1% of the energy required for conventional casting) (5–7).

Crown restorations produced by galvanoforming technology have excellent marginal or internal adaptation and high biocompatibility. Additionally, the electroforming system has been made practical for use in small dental laboratories. In the literature, although a large number of galvanoceramic crown studies exist (8–10), there are limited data about galvanoceramic inlays (7,11). In the literature, it is reported that galvano-inlays are clinically advisable, but no detailed study has been found investigating their marginal fit.

The purpose of this in vitro study was to investigate the marginal fit of galvanoceramic inlays and to compare two different all-ceramic inlays. The null hypothesis was that no differences in the marginal adaptation among all three inlays and also, between the galvanoformed coping and galvanoceramic inlay.

MATERIALS AND METHODS

Inlay Preparation Design

A standard class II (mesio-occlusal) inlay cavity was prepared on an ivorine mandibulary left molar teeth using a diamond coated bur (Columbia Dentaform Corp., Long Island City, NY).   Occlusal depth was prepared to 3 mm from the oclusal margin, the occlusal width was 5 mm, and proximal depth was 4 mm in central fossa and 3 mm in other areas. The proximal box was extended 1.5 mm above from the cervical line and the taper between the cavity walls was 6 degrees. All internal cavity angles were rounded.   A butt-joint margin preparation was made at the all margins and no bevels were utilized in the preparation to obtain accurate measurements. To control of the cavity preparation was used a paralleling device which reduced operator error (Paraskop, Bego Bremer Goldschlagerei Wihl., Hebst GmbH&Co., Germany). In this way, the cavity was cut accurately with the 6° taper determined by the taper of the bur. An impression of the cavity was made using a polyether impression material (Impregum 3M Espe, Germany). The master die model for SEM analysis was prepared by pouring carbonizes acrylic resin (Pattern Resin LS, GC Dental Products Corp., Japan) into this impression. The master model was fabricated with a base metal alloy (Nicor, Schütz Dental, Germany), and the surface was smoothed using diamond impregnated green stone wheels to remove metal casting burrs. The polishing process of the master model was performed using a medium-grit green hard rubber polisher (Dentauram, Germany), a fine-grit gray soft rubber polisher, a felt buff with pumice slurry, and a felt buff with green polishing compound (Degussa, USA), respectively.

Table 1. Inlay materials used in this study

Inlay type	Material	Manufacturer	Chemical composition
All-ceramic inlay	Alumina based all-ceramic	Turcom-Ceramics, Kuala Lumpur, Malaysia	99.15% Al_2O_3 (52.93%Al , 47.07% O)
All-ceramic inlay	Lithium disilicate-reinforced all-ceramic	Ivoclar Vivadent, Schaan, Liechtenstein Gramm Technique, Heimerdingen, Germany	SiO_2 57-80%, Li_2O 11-19%, Al_2O_3 0-5%, La_2O_3 0.1-6%, ZnO 0-8%, K_2O 0-13%, MgO 0-5%, P_2O_5 0.5-11%, Additives 0-6%, Colorants 0-8%
Galvanoceramic inlay	24-K Gold	VITA Zahnfabrik, Bad sackingen, Germany	99.99% of pure gold
	Feldspathic porcelain		SiO_2 60-64%, Al_2O_3 13-15%, K_2O 7-10%, Na_2O 4-6%, TiO_2 <0.5%, CeO_2 <0.5%, ZrO_2 0-1%, CaO 1-2%, B_2O_3 3-5%, BaO 1-3%, SnO_2 0.1%, Oxides of Mg, Fe <0.5%

Stereomicroscopic evaluation (Zeiss S100, Carl Zeiss Surgical GmbH, Oberkochen, Germany) with 25× magnification was conducted to check the marginal integrity of the master die. Impressions for fabricating of

each inlay restoration were taken using a polyether impression material (Impregum 3M Espe, Germany) and cast in Type IV stone.

Inlay Fabrication

A total of 45 inlay restorations were produced by the same laboratory from three different materials and technique. The materials used to fabricate inlays, along with their manufacturers and chemical compositions, are presented in Table 1. Fifteen galvanoceramic inlays were fabricated in two stages; producing of gold galvanoformed coping and adding feldspathic porcelain on it. Galvanoformed copings of 0.25 mm were fabricated by a galvanoforming machine (GES Gold–Electroforming System, Gramm Technique GmbH, Heimerdingen, Germany) produced for dental usage. Fifteen duplicated stone (Type IV Suppen-Sockler G, Picodent Productions und Vertriebs GmbH, Germany) dies were prepared, and covered a thin silver layer and then connected to a copper wire. Thanks to this way, transition of the galvanic current through dies was provided to enable the gold electrodeposition. The dies were immersed into the gold electrolyte solution (Ecolyt SG 100, Gramm Technik, GmbH, Germany) in the beaker. The beaker was placed in the galvanoforming machine (GES Gold –Electroforming–System, Gramm Technique GmbH, Germany) and electrodeposition process was started. After the completion of the electro deposition, the gypsum dies were removed into the gold electrolyte solution and electroformed inlay copings were removed from the dies using gypsum remover (Gips Löser, Gramm Technik GmbH,Germany) in a ultrasonic cleaner. The removed inlay copings were re-cleaned by nitric acid with %5 solution in ultrasonic cleaner. So that, the silver nitrate solution that remained on the inner surface of the inlay copings, was cleaned. After cleaning and adjustments all specimens were examined for integrity under a stereomicroscope magnification x 25 (Carl Zeiss f 170, Carl Zeiss Surgical GmbH, Germany) via the copings were placed one by one on the master metal die. After marginal measurements, feldspathic porcelain application was made on the copings to produce galvanoceramic inlays. The galvano ceramic bonder (GES Galvano-bonder, Gramm GmbH Co. Heimerdingen, Germany), opaque porcelain, dentin porcelain, and enamel porcelain (VMK95; VITA Zahnfabrik, Bad Sackingen, Germany) were applied on these copings, respectively. The firing procedures were performed according to the firing schedule recommended by the manufacturer. Prepared galvanoceramic specimens were placed one by one on the master die to examine their integrity under a stereomicroscope (Carl Zeiss 170, Carl Zeiss Surgical GmbH, Oberkochen, Germany) at 25× magnification.

In this study two different ceramic inlays (lithium disilicate based and alumina based) were used as control groups to compare galvanoceramic inlays. Fifteen lithium disilicate-reinforced all-ceramic inlays (IPS Empress 2; Ivoclar Vivadent, Schaan, Liechtenstein) were fabricated using a high-temperature injection molding technique following manufacturer's instructions. Fifteen alumina-based all ceramic inlays were also fabricated according to the manufacturers' direction using the Turkom-Cera technique (Turcom-Ceramics, Sdn Bhd, Kuala Lumpur, Malasia).
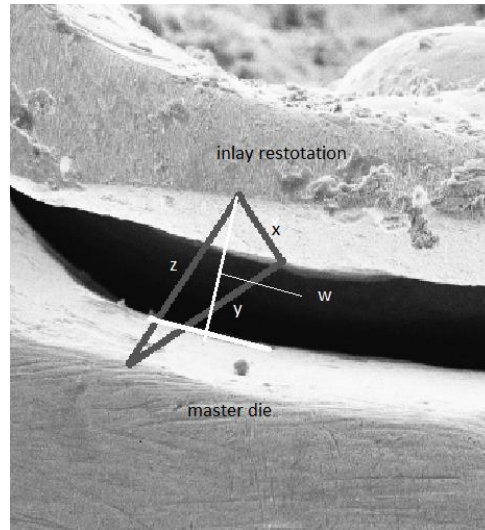
Figure 1. SEM image of a sample. Definition of measuring distances for marginal accuracy. x: horizontal marginal discrepancy; y: vertical marginal discrepancy; z: absolute marginal discrepancy; w: marginal gap.

Marginal Gap Analyses

The absolute marginal discrepancy measurements defined by Holmes (12) were used in this study to evaluate marginal gap analyses. The marginal distance between the external edges of the inlay cavity on the master die and the marginal edges of the fabricated inlays was defined as "the absolute marginal discrepancy". It is the hypotenuse of a right triangle, the sides of which are the vertical and horizontal marginal discrepancies (Figure 1).

Measured points

1. Mesio-bucco-occlusal point
2. Top point of the mesio-buccal cusp
3. Top point of the disto-buccal cusp
4. Disto-bucco-occlusal point
5. Center point of the disto-buccal wall
6. Disto-linguo-occlusal point
7. Top point of the disto-lingual cusp
8. Top point of the mesio-lingual cusp
9. Mesio-linguo-occlusal point
10. Center point of mesio-lingual wall
11. Mesio-linguo–cervical point
12. Corner of mesio-lingual cervical point
13. Mesio-cervical point
14. Corner of mesio-buccal cervical point
15. Mesio-bucco-cervical point
16. Center point of mesio-buccal wall

Figure 1. Measurement points on the master die. Occlusal view of the master die is in the picture A, mesial view of the master die is in the picture B. Custom made specimen positioning device is in the picture C.

The sixteen different points were scribed on the master die for standardised measurements without damaging the margins. The master die was mounted onto a custom-made specimen-positioning device that swivels around its axis to observe al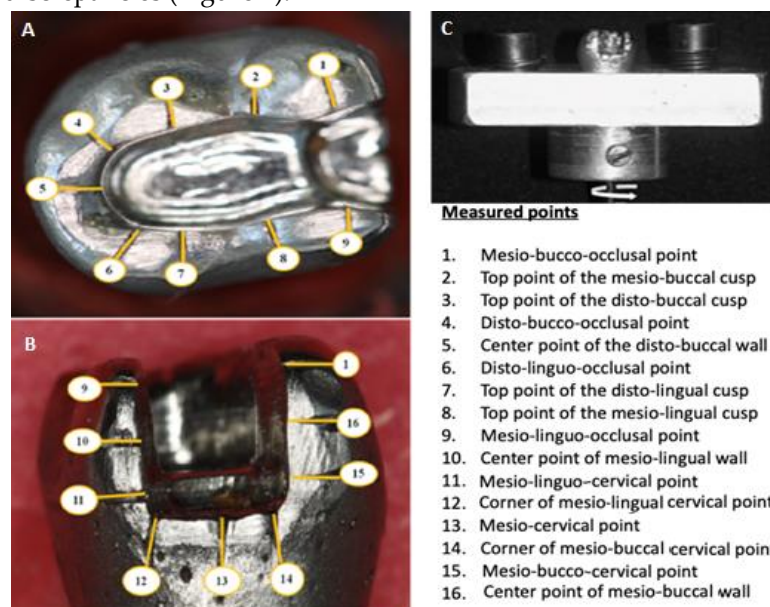l measurements points without removing the master die during microscopic investigation (Figure 2). The absolute marginal discrepancies of each inlay were measured at the 16 scribed reference points using scanning electron microscope (SEM) (LEO 440 Computer Controlled Digital, Leica Zeiss, Cologne, Oberkochen, Germany) at an accelerating voltage of 20–30 kV and 100μm bar. Each point was measured twice. A total of 32 marginal adaptation measurements were performed for each specimen. All measurements were performed without cementation. At the galvanoceramic inlay, the measurements were conducted both before and after porcelain application. A total of 1920 measurements of the marginal gap were performed (45 samples×16 points×2 times on inlays; 15samples×16 points×2 times on galvano-copings).

Statistical analyses

The statistical analysis of the data was performed using the SPSS version 22.0 statistical software package program. Shapiro-wilk tests were used to evaluate normal distribution of the data. Levene test was used to determine homogeneity of the variances. The data of the marginal discrepancies were statistically compared among the measurement points and inlay material using two-way analysis of variance (2-side ANOVA). Comparison between galvanoformed copings and galvanoceramic inlays were made using paired t-test. Post-hoc Tamhane T2 test was used for multiple comparisons. The level of significance was set at α=0.05.
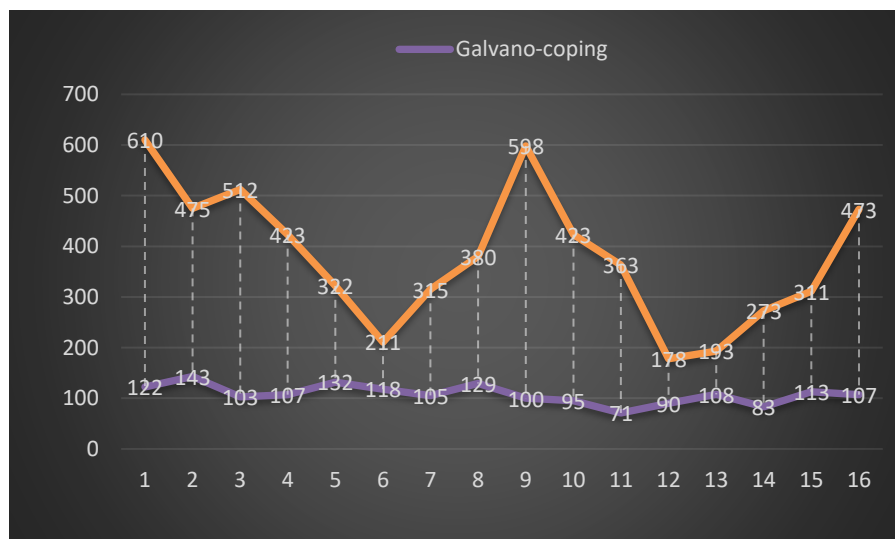
RESULTS

Figure 2. The galvanoceramic inlays exhibited a significantly larger marginal gap at all points (The highest p value belonged to the 13th point. p=0.011).

Marginal gap differences between galvanoformed copings and galvanoceramic inlays at each measurement points are shown in Figure 3. The mean marginal gap of galvanoformed copings for all points prior to porcelain firing ranged from 71 to 143 μm, whereas after firing the mean marginal gap ranged from 178 to 610 μm. According to the paired t-test, the differences in the marginal fit between galvanoformed copings and galvanoceramic inlays were significant at all measurement points (p<.001). Figure 3 presents grafical outline of the differences in marginal fit between galvanocoping and galvanoceramic inlay at each measurement point. Galvanoceramic inlays exhibited a significantly larger marginal gap than galvanoformed copings. The maximum changes were observed in points 1 and 9 (mesio-bucco-oclusal and mesio-linguo-oclusal points; at the ocluso-proximal corner part of the restoration), and the minimum changes were determined in points 12, 13 (corner of the mesiolingual cervial point and mesio-cervical point; at cervical terminal part of the inlay) and 6 (at disto-linguo-occlusal point; at occlusal terminal part of the inlay). The highest p value represented the least change in marginal adaptation and was attributed to the 13th point (at the mesio-cervical terminal point) (p=0.011).
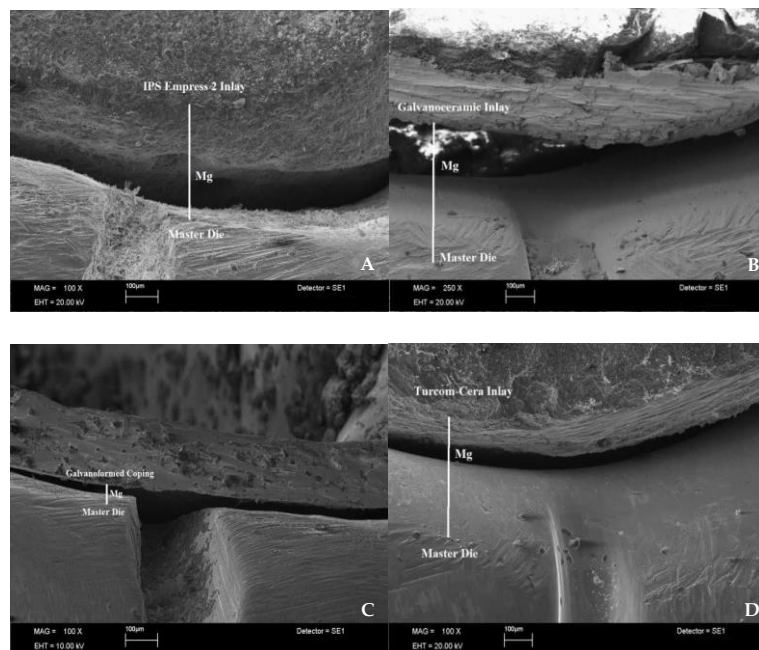
Figure 4. SEM images that were taken from same measurement point (point 5). A. Marginal gap of Lithium disilicate reinforced all-ceramic inlay B. Marginal gap of galvanoceramic inlay; C. Marginal gap of galvanoformed coping D. Marginal gap of Alumina based all ceramic inlay.; Mg: marginal gap.

Scanning electron microscopic images in Figure 4 demonstrates the marginal gaps were taken from same measurement point (point 5) for all inlay type and galvanocoping. As observed, galvanocoping exhibited the closest marginal adaptation, while the galvanoceramic inlay had a significantly greater marginal gap than the other types of inlays. The comparison of marginal gap in measurement points among inlay types are shown in Table 2.

Two-way ANOVA results indicated a significant difference among inlay types and measurement points. The effect of the inlay material and measurement points and the interaction between these two parameters was found to be significant (F=32.805, p<.001). The mean and standard deviation of the marginal gap was 186±34 μm in alumina inlays, 188±36 μm in lithium disilicate ceramic inlays, and 379±153 μm in galvanoceramic inlays. Except three points (6-distolinguoocclusal point, 12- corner of the mesiolingual cervical point and 13- mesiocervical point), marginal gap of the galvanoceramic inlays higher than 250 μm (Figure 5). When evaluated the marginal gap obtained from the all-measurement points, other two ceramic inlays exhibited similar marginal gap (p=.857).

Table 2. The comparison of marginal gap in measurement points among inlay types used in the study (the unit of measurement is micron, i.e. μm)

Measured Points	n	Number of measurement	Alumina Based inlay Mean(SD)	Lithium Disilicate Based Inlay Mean(SD)	Galvanoceramic inlay Mean(SD)	p
1	15	30	178(27)[ab,A]	208(34)[de,B]	610 (191)[af,C]	.000
2	15	30	184(32)[ab,A]	211(28)[e,A]	475(108)[adg,B]	.000
3	15	30	207(27)[b,A]	189(26)[cde,A]	512(84)[af,B]	.000
4	15	30	203(34)[b,A]	201(27)[cde,A]	423(44)[ab,B]	.000
5	15	30	209(20)[b,A]	203(21)[cde,A]	322(67)[bh,B]	.000
6	15	30	177(23)[ab,A]	168(28)[bc,A]	211(16)[c,B]	.000
7	15	30	174(37)[ab,A]	186(44)[bcde,A]	315(74)[bh,B]	.000
8	15	30	183(32)[ab,A]	219(22)[e,B]	380(75)[bde,C]	.000
9	15	30	198(30)[b,A]	127(18)[a,B]	598(78)[f,C]	.000
10	15	30	195(30)[ab,A]	190(27)[cde,A]	423(58)[ae,B]	.000
11	15	30	176(36)[ab,A]	173(32)[bcd,A]	363(95)[beg,B]	.000
12	15	30	200(25)[b,A]	198(31)[cde,A]	178(28)[c,A]	.099*
13	15	30	206(28)[b,A]	210(28)[e,A]	193(31)[c,A]	.249*
14	15	30	173(38)[a,A]	152(28)[ab,A]	273(48)[bh,B]	.000
15	15	30	156(29)[a,A]	195(25)[cde,B]	311(53)[bh,C]	.000
16	15	30	150(19)[a,A]	183(31)[bcde,A]	473(111)[aef,B]	.000
TOTAL	45	1440	186(34)[b,A]	188(36)[cde,A]	379 (153)[beg,B]	.000

Different small letter superscripts in a column show the significant difference among measurement points at p<.05. Different capital letter superscripts in a row shows the significant differences among inlay types at p<.05. Sd: Standart deviation. *p >.05
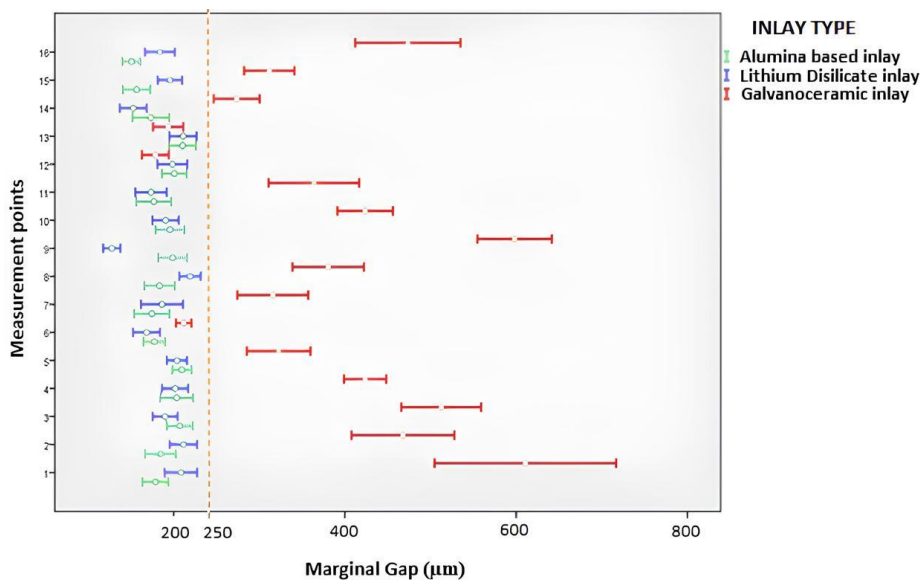
Figure 3. Error bars graphic showing the clustering differences about marginal gaps of the inlays. Marginal gaps of the alumina and lithium disilicate inlay groups are generally under 250 microns. In galvanoceramic inlays, only the measurement points of 6,12 and 13 are under 250 microns. Error bars indicated 95% confidence interval.

DISCUSSION

This in vitro study was designed to assess the marginal adaptation of galvano-ceramic inlays with gold margins versus conventionally produced ceramic inlays made by different materials and techniques, and to determine whether had clinically acceptable marginal adaptation. To our knowledge, our study is the first to demonstrate that galvanoceramic inlays do not provide good marginal adaptation and even have clinically unacceptable marginal fit.

Numerous studies have designed in literature to determine the marginal adaptation in restorative materials (1–4). Researchers have preferred on in vitro simulations due to the advantages of the controlled conditions, standardization and reasonable time(13–15). In the present study, one single metal die was used for fabrication of the inlays. The advantage of this was the standardised preparation, which assured that the fabrication of all specimens was based on the same original source and that minimal wear of the die margins occurred during measurements. Moreover, the master die was mounted on a custom-made specimen positioning apparatus that swivelled around its axis, allowing the observation of measurement points without removing the master die during microscopic investigation.

The film thicknesses of cements after cementation can vary depending on the type and properties of the cement and the cementation pressure applied by the dentist. The marginal adaptation of the restoration can be affected by cementation process (16,17). For this reason, the cementation procedure was not accomplished

in this study in order to determine the effect of the material used and the fabrication technique regardless of the cements and cementation processes.

Although numerous studies have been reported regarding the marginal fit of galvanoceramic crowns(9,12,18), information about marginal integrity of galvanoceramic inlays is unclear. Galvanoformed crown copings and galvanoceramic crowns have exhibited superior marginal adaptation when compared the crowns made of all ceramic or non-noble alloy materials (12,18). Buso et al. (8) reported that the mean marginal gap of the galvanoformed crown copping was 30±19 μm. Shiratsuchi et al. (9) reported that the marginal gap of the galvanoformed crown copping was between 18–50 μm. In our study, we observed that the mean marginal gap of the galvanoformed copings to be 107±25 μm, higher than that reported by these studies(8,9) The reason of this would be galvanoformed crown copings have a circular margin, while galvanoformed inlay copings have linear occlusal and approximal margins, intersecting at right angles to each other.

The results of this study revealed that there was a significant increase at marginal gap of galvanoceramic inlay after porcelain firing. Studies about crown restorations in literature has been reported that there was a change in marginal fit after porcelain firing. A previous study(9) reported that the marginal gap of the galvanoformed crown copping was 18–50 μm, while that of the galvanoceramic crown was 24–89 μm. Petteno et al.(18) reported that the marginal gap of the galvanoceramic crown was approximately two times greater than that of the galvanoformed crown copings. In our study, the marginal gaps of galvanoceramic inlays were increased after porcelain firing, in agreement with the results of these studies (9,18). However, we differently found that the marginal discrepancy of galvanoceramic inlays was approximately three times greater than that of the galvanoformed copings. These differences may be the result of variability in the restoration type used and/or the measurement method. Some studies in literature (19,20) indicated that firing of the porcelain may cause marginal distortion. Komine et al.(20) stated that galvanoformed crowns undergo marginal distortion due to shrinkage of porcelain mass, and this factor caused marginal discrepancy nearly 34μm when used shoulder finish line. Since inlay margins extend linearly, unlike crown margins, the shrinkage in the porcelain would be pulled the galvanocoping margins towards the centre of the inlay and away from the inlay cavity walls. This may explain why the marginal discrepancy after porcelain firing was much higher in inlays compared to crowns.

According to the literature, the acceptable marginal gap for dental restorations, including both crown and inlay/onlay, is controversial. Some studies accepted that the ideal marginal gap should be below 120 μm to prevent dissolution of the luting cement, while the most authors have stated that a marginal gap should be below 200 μm that is the clinically acceptable threshold (3,13,17,21–23). There are many factors that can influence this value; among them are production methods, materials used for restorations, and measurement techniques. Holmes et al. (12)defined the absolute marginal discrepancy as the hypotenuse of a right triangle, the sides of which are the vertical and horizontal marginal discrepancies. The perpendicular measurement

from the surface of the abutment to the margin of the retainer is called the "marginal gap". Absolute marginal discrepancy values are higher than marginal gap values and it can be up to 250 μm (24) According to a systematic review study investigated marginal and internal fit of inlay/onlay restorations stated that the measured mean marginal gap of inlay/onlay restorations ranged between 36 μm and 222.5 μm (13). Another study that used the absolute marginal discrepancy measurement technique to evaluate the marginal fit of inlays reported a mean marginal gap of 177 ± 69 μm (25). These different results indicate that marginal gap measurements can vary depending on restoration types and measurement methods, but are generally under 250 micrometers. According to our results, mean marginal discrepancy of alumina based and lithium disilicate based inlays were within clinically acceptable limitations, whereas the mean data from galvanoceramic inlays had clinically unacceptable marginal discrepancy (over 250 μm), in contrary to manufacturer's declarations and commonly predicted. Only the 3 points at the occlusal and gingival terminal ends of the inlay restoration were within acceptable limits. Considering the linear structure of the inlay restoration, it can be seen that these three points are on the short edges. This confirmed that the porcelain shrinks substantially towards the center of the inlay, so that the marginal discrepancy at the long edges is much greater.

Galvanoformed copings for inlays exhibited much better marginal adaptation than both galvano-ceramic inlay and the other ceramic inlays at all measurement points in our study.   This shows that if thin galvanoformed coping structure can be protected from the negative effects of porcelain firing, it can have a much better marginal fit than ceramic inlays produced by other methods. In order to obtain the advantage of the superior properties of gold margins, future studies should focus on methods to apply porcelain into the inlay without allowing shrinkage of the galvanoformed copings.

CONCLUSION

Within the limitations of this in vitro study, the following conclusions may be drawn; First, the galvano-copings exhibited that nearly perfect marginal fit, but porcelain application dramatically disrupted this adaptation, so galvanoceramic inlays had the largest marginal gaps. Second, the marginal fit of the lithium disilicate and the alumina-based inlay restorations were generally similar to each other. Additionally, mean marginal fit of these inlays was within clinically acceptable limits, but galvanoceramic inlays had marginal discrepancy over 200-250 μm that is upper limit of marginal discrepancy for clinical acceptance of dental restorations.

Conclusively, the inlays produced with current galvanoforming technology is inconvenient due to high marginal discrepancy.   However, if the new methods that reduce or eliminate the shrinkage effect of the porcelain can be developed in further studies, much more adapted and highly biocompatible inlays with gold margins can be used in dental practice.

Acknowledgments

The authors thank to Assoc. Prof. Dr. Eyup Gerçekçioğlu for fabricating specimen positioning device and his technical assistance. A part of this study was presented as poster presentation at the 16. Aegean Region Chambers of Dentist, International Scientific Congress and Exhibition in Izmir, Turkey.

Authorship contributions

Concept: OC, ZE, AG; Design: OC, ZE, AG; Data Collection or Processing: OC, ZE, Analysis or Interpretation: OC, AG; Literature Search: OC, ZE; Writing: OC, AG.

Declaration of competing interest

No conflict of interest was declared by the authors.

Ethics

This article does not contain any studies with human participants or animals performed by any of the authors.

Funding

This work has not received any funding support.

REFERENCES

1. Adel M, Hamdy A, Sabet A, Ebeid K. Effect of cervical margin relocation on marginal adaptation and microleakage of indirect ceramic restorations. Journal of Prosthodontics. 2024;33(4).
2. Haralur SB, AL Ghaseb GA, Alqahtani NA, Alqahtani B. Comparison of microleakage between different restorative materials to restore marginal gap at crown margin. PeerJ. 2021;9.
3. Taha AI, Hafez ME. An in vitro study measuring marginal gaps of inlay restorations fabricated from different CAD-CAM materials after thermocycling. BMC Oral Health. 2023;23(1).
4. Papadiochou S, Pissiotis AL. Marginal adaptation and CAD-CAM technology: A systematic review of restorative material and fabrication techniques. Vol. 119, Journal of Prosthetic Dentistry. 2018.
5. Weishaupt P, Bernimoulin JP, Lange KP, Rothe S, Naumann M, HÄgewald S. Clinical and inflammatory effects of galvano-ceramic and metal-ceramic crowns on periodontal tissues. J Oral Rehabil. 2007;34(12).
6. Oleszek-Listopad J, Sarna-Bos K, Szabelska A, Czelej-Piszcz E, Borowicz J, Szymanska J. The use of gold and gold alloys in prosthetic dentistry - A literature review. Vol. 28, Current Issues in Pharmacy and Medical Sciences. 2015.
7. Gradinaru I, Jipu R, Hurjui L, Balcoş C, Mitrea M, Antohe ME. Galvanoformation in fixed prostheses: procedure always up to date. Vol. 9, Romanian Journal of Medical and Dental Education.
8. Buso L, Neisser MP, Bottino MA. Evaluation of the marginal fit of electroformed copings in function of the cervical preparation. Braz Dent Sci. 2010;7(1).
9. Shiratsuchi H, Komine F, Kakehashi Y, Matsumura H. Influence of finish line design on marginal adaptation of electroformed metal-ceramic crowns. Journal of Prosthetic Dentistry. 2006;95(3).
10. Polansky R, Heschl A, Arnetzl G, Haas M, Wegscheider W. Comparison of the marginal fit of different all-ceramic and metal-ceramic crown systems: an in vitro study. Int J Stomatol Occlusion Med. 2010;3(2).
11. Kaán B, Eichner K, Kaán M, Fejérdy P, Róth L. In vivo and in vitro study of the marginal sealing in ceramic-covered gold inlays. Fogorv Sz. 1998;91(12).

12. Holmes JR, Pilcher ES, Rivers JA, Stewart RMQ. Marginal fit of electroformed ceramometal crowns. Journal of Prosthodontics. 1996;5(2).

13. Goujat A, Abouelleil H, Colon P, Jeannin C, Pradelle N, Seux D, et al. Marginal and internal fit of CAD-CAM inlay/onlay restorations: A systematic review of in vitro studies. Vol. 121, Journal of Prosthetic Dentistry. 2019.

14. Raghav PS, Abirami S, Gupta A, Yusufi FNK, Afroz S. Effect of Different Impression Techniques on Marginal Fit of Restoration – An In Vitro Study. Indian Journal of Dental Research. 2023;34(3).

15. Yang S, Li Q, Chen S yuan, Yu H. Effect of multiple firings on the marginal fit of monolithic zirconia crowns: An in vitro study. Journal of Prosthetic Dentistry. 2023;130(6).

16. de Almeida JG dos SP, Guedes CG, Abi-Rached F de O, Trindade FZ, Fonseca RG. Marginal Fit of Metal-Ceramic Copings: Effect of Luting Cements and Tooth Preparation Design. Journal of Prosthodontics. 2019;28(1).

17. Ferrari M, Dagostin A, Fabianelli A. Marginal integrity of ceramic inlays luted with a self-curing resin system. Dental Materials. 2003;19(4).

18. Pettenò D, Schierano G, Bassi F, Bresciano ME, Carossa S. Comparison of marginal fit of 3 different metal-ceramic systems: an in vitro study. Int J Prosthodont. 2000;13(5).

19. Balkaya MC, Cinar A, Pamuk S. Influence of firing cycles on the margin distortion of 3 all-ceramic crown systems. Journal of Prosthetic Dentistry. 2005;93(4).

20. Komine F, Shiratsuchi H, Kakehashi Y, Matsumura H. Influence of porcelain-firing procedures on the marginal distortion of electroformed metal-ceramic restorations. Quintessence Int (Berl). 2007;38(10).

21. Papaspyridakos P, Vazouras K, Chen Y wei, Kotina E, Natto Z, Kang K, et al. Digital vs Conventional Implant Impressions: A Systematic Review and Meta-Analysis. Vol. 29, Journal of Prosthodontics. 2020.

22. Björn AL, Björn H, Grkovic B. Marginal fit of restorations and its relation to periodontal bone level. II. Crowns. Odontol Revy. 1970;21(3).

23. McLean JW, Von F. The estimation of cement film thickness by an in vivo technique. Br Dent J. 1971;131(3).

24. Demir N, Ozturk AN, Malkoc MA. Evaluation of the marginal fit of full ceramic crowns by the microcomputed tomography (micro-CT) technique. Eur J Dent. 2014;8(4).

25. Rippe MP, Monaco C, Volpe L, Bottino MA, Scotti R, Valandro LF. Different methods for inlay production: Effect on internal and marginal adaptation, adjustment time, and contact point. Oper Dent. 2017;42(4).

Research Article

THE ROLE OF INFLAMMATORY PARAMETERS AND SCORING SYSTEMS IN PREDICTING COMPLICATED ACUTE APPENDICITIS

Mehmet Gökhan KAYA [1,*], Ethem ACAR [2]

[1] Emergency Medicine Service, Yatagan State Hospital, Yatagan, Mugla, TURKIYE
[2] Department of Emergency Medicine, Faculty of Medicine, Mugla Sitki Koçman University, Mugla, TURKIYE

Correspondence: mgokhankaya@windowslive.com

ABSTRACT

Aim: To assess the complications associated with acute appendicitis (AA) and to evaluate how specific routine patient parameters influence disease severity.

Materials and Methods: A retrospective study was carried out on patients diagnosed with AA who presented to the emergency department (ED) between January 1, 2019, and December 31, 2020. Data collected included demographic details, blood test results, and specific scoring systems utilized in the ED.

Results: Of the 223 patients studied, 63.7% were male with a mean age of 37.5 ± 16.8 years. Patients with complicated appendicitis (CA) showed significantly elevated hematological parameters such as neutrophil-to-lymphocyte ratio (NLR), platelet-to-lymphocyte ratio (PLR), C-reactive protein (CRP), systemic immune inflammation index (SII), white blood cell count (WBC), and neutrophil levels. Conversely, decreased lymphocyte/C-reactive protein ratio (LCRP) and lymphocyte levels were noted. Furthermore, CA cases exhibited significantly greater Appendicitis Inflammatory Response (AIR) and Alvarado scores. In the context of diagnosing CA, the AIR score had a sensitivity of 85.9% and a specificity of 47.9% with a cut-off value of ≥6 (95% CI 0.675-0.821, Area Under the Curve (AUC): 0.748; p<0.01). The Alvarado score showed a sensitivity of 80.6% and a specificity of 44.5%, using a cut-off value of ≥6 (95% CI 0.527-0.683, AUC: 0.605; p=0.10).

Conclusion: Our study determined that inflammatory markers such as LCRP, SII, NLR, and PLR serve as significant indicators for distinguishing between CA and its NCA.

Keywords: Acute appendicitis, Appendicitis inflammatory response score, Alvarado score, Emergency department, Complicated appendicitis, Non-complicated appendicitis

INTRODUCTION

Approximately 5% to 10% of patients presenting to the Emergency Department (ED) report abdominal pain (1). Given the frequent occurrence of this problem and its varied etiologies, there is a growing interest in imaging and laboratory methods to aid differential diagnosis (2). Acute appendicitis (AA) stands out as the predominant abdominal surgical condition encountered globally. Its prevalence is approximately 8.6% in males and 6.9% in females (3). The significance of early diagnosis in AA cannot be overstated. The risk of perforation, for instance, ranges from 16% to 36% within the initial 36 hours of abdominal pain onset, and sees an additional increase of 5% every subsequent 12 hours (4). This is concerning, especially since perforation stands as the most common complication of AA, contributing substantially to increased mortality and morbidity (5). Thus, timely intervention and early diagnosis in patients susceptible to complications are paramount. Notably, the challenge persists in identifying a universally acknowledged gold standard for diagnosing AA. Even with assessments from seasoned radiologists, imaging techniques like ultrasonography (USG) and computed tomography (CT) haven't met the expected diagnostic precision, prompting continuous research into alternative diagnostic methodologies (6).

The primary objective of this study is to determine the discriminatory power of laboratory values, imaging results, and appendicitis scoring systems in distinguishing between complicated appendicitis (CA) and non-complicated appendicitis (NCA) by comparing them with pathology reports.

MATERIALS AND METHODS

Study Design and Setting

This retrospective, single-center, observational, cross-sectional study was conducted in the ED of a university-affiliated training and research hospital in Muğla, Turkey. Data were collected from consecutive patients admitted to the ED between January 1, 2019, and December 31, 2021, who were subsequently diagnosed with concomitant acute appendicitis. Ethical approval for the study was obtained from the local ethics committee (Reference Number: 7), and the research was performed in accordance with the Principles of the Declaration of Helsinki (1975), as revised in 1983. Due to the retrospective nature of the study, the necessity for written informed consent was waived.

Definitions and Clinical Scoring Systems

AA refers to the inflammation of the appendix, which is a blind-ended pouch located in the lower right abdomen. When patients present with abdominal pain in the ED, a diagnosis of AA is established through the patient's history, physical examination, laboratory tests, clinical scoring systems, and imaging methods.

Patients in the study were categorized into two groups: those with CA and NCA. The identification of CA was based on surgical and pathological findings, with the aim to ascertain the prevalence of CA. Specifically, surgical and/or pathological reports that described conditions as gangrenous/necrotizing, abscessed, or perforated were classified under CA. All other diagnostic outcomes were categorized as NCA.

To evaluate the severity of AA, we utilized both the Appendicitis Inflammatory Response (AIR) score and Alvarado score.

Outcome Measures

The differentiation between CA and NCA is important to assess the severity of the health issue and determine the appropriate treatment method. CA indicates advanced stages of appendicitis. In cases of CA, there may be perforation of the appendix or other serious complications. Perforation, spreading of inflammation to surrounding tissues, or other appendicitis-related complications can pose a significant risk to the patient's outcome. Early diagnosis and treatment can reduce the risk of such complications.

On the other hand, in NCA cases, patients may experience a quicker recovery process, and their length of stay (LOS) hospital stay may be shorter. In contrast, in cases of CA, the recovery process can be more prolonged and complex.

CA cases can lead to more complex surgical interventions and an increased risk of surgical complications. Therefore, it is essential to differentiate between CA and NCA to manage patients effectively and prevent complications. Consequently, clinical, laboratory, imaging results and scoring systems can be used to make this distinction.

Patient Selection

Our study primarily encompassed 223 patients who were aged 18 years and above, had been diagnosed with AA in the ED, and had operated by the general surgery team. However, certain groups were excluded to maintain the study's integrity. These included 85 patients under 18 years, those with incomplete data or a recent hospitalization history within the last 14 days, 5 pregnant individuals, 2 immunosuppressed patients, 3 patients diagnosed with hematological or liver diseases, and 10 patients underwent an appendectomy for reasons other than AA.

Data Collection

Patient records were retrieved via archival research, utilizing the HIMS for laboratory result extraction. For every patient satisfying the study's inclusion criteria, a dedicated form was developed. This form encapsulated various parameters: demographic details (age and gender), laboratory results, C-reactive protein (CRP), White blood cell count (WBC), Platelet (PLT), Neutrophil (NEU), Lymphocyte (LYM), Neutrophil-to-Lymphocyte ratio (NLR), Platelet-to-Lymphocyte ratio [PLR], Systemic Immune-Inflammation Index (SII), and Lymphocyte to CRP ratio (LCRP)], length of stay (LOS) hospital, CT scan outcomes, the patient group

diagnosed with CA, AIR and Alvarado scores from the ED, and admission year (2019-2020). The initial Alvarado score, and AIR score were systematically calculated for each patient.

Statistical Analysis

Whether the continuous variables conformed to a normal distribution was assessed using the Kolmogorov-Smirnov test. Descriptive statistics were reported as mean ± standard deviation for continuous and discrete numerical variables, while for categorical variables, the number of cases and percentage (%) were provided. For parameters showing a normal distribution, Student t-test was employed for comparisons, while the Mann–Whitney U test was used for comparisons between two different groups for parameters that did not display a normal distribution. Sensitivity, specificity, the positive predictive value (PPV) and the negative predictive value (NPV) were evaluated for parameters used in distinguishing between the groups. Receiver Operating Characteristic (ROC) analysis was performed to determine the appropriate cutoff value along with specificity and sensitivity values. Results obtained with $p<0.05$ were considered statistically significant. Statistical analyses were performed using the SPSS software package, version 22 (SPSS Inc., Chicago, Illinois, USA).

RESULTS

Between January 1, 2019, and December 31, 2020, a total of 328 patients were diagnosed with AA at the Emergency Department of Muğla Training and Research Hospital and subsequently underwent surgery in the hospital's General Surgery Department. Following the application of the exclusion criteria), the study focused on a final sample of 223 patients.

The patient cohort exhibited a mean age of 37.5 ± 16.8 years, encompassing a range of 18–90 years, with males constituting 63.7% of the population. Central tendency and variability in laboratory results were noted as follows: a median WBC count of 12.61 (3,30-24,96), mean NEU count of 9.83±3,70, median NLR of 7.25 (0,67-40,39), median PLR of 172,31(50,11-780,65), median LCRP of 0,40 (0,00-4,72), and median SII of 1816,99(158,03-10828,33). Tables 1 provide an in-depth view of the patients' laboratory results. Furthermore, significant differences were identified in several laboratory parameters between CA and NCA, specifically in WBC, NLR, PLR, LCRP and SII. ($P = 0.045$, $P < <0.001$, $P = 0.010$, $P<0.001$ and $P = <0.001$, respectively).

Table 1. Comparison of age, hemogram and crp values in the differentiation of complicated appendicitis

	Complicated Appendicitis (n= 57)	Non-complicated appendicitis (n= 166)	Total (n=223)	*P* Value
Age	41.00 (19.00-90.00)	30.00 (18.00-85.00)	37.54 (18-90)	**<0.001**
WBC(10^3/μg)	13.35 (6.90-24.96)	12.18 (3.30-20.02)	**12.61(3.30-24.96)**	**0.045**
PLT (10^3/μg)	239 (147.00-365.00)	242.5 (101.00-611.00)	252.35(101.00-611.00)	0.693
NEU (10^3/μg)	10.99 ±3.63	9.43 ±3.65	**9.83±3.70**	**0.006**
LYM (10^3/μg)	1.36 (0.41-3.41)	1.80 (0.31-4.44)	**1.79(0.31-4.44)**	**0.002**
NLR	8.20 (1.94-29.75)	5.18 (0.67-40.39)	**7.25(0.67-40.39)**	**<0.001**
PLR	203.17 (78.42-715.60)	161.72 (50.11-780.65)	**172.31(50.11-780.65)**	**0.010**
CRP(mg/L)	51.78 (3.73-599.00)	9.90 (0.60-303.92)	**47.40(0.60-599.00)**	**<0.001**
LCRP	0.07(0.00-0.48)	0.51(0.00-4.72)	**0.40(0.00-4.72)**	**<0.001**
SII	2316.05(488.75-10828.33)	1645.63(158.03-9773.68)	**1816.99(158.03-10828.33)**	**<0.001**

Note: Data showing parametric distribution is presented as Mean ± Standard Deviation, while data that does not show parametric distribution is presented as Median (minimum-maximum). *WBC: White Blood Cell, PLT: Platelet, NLR: Neutrophil / Lymphocyte Ratio, PLR: Platelet / Lymphocyte Ratio, CRP: C-Reactive Protein, LCRP: Lymphocyte / C-Reactive Protein Ratio, SII: Systemic Immune Inflammation Index

According to the data presented in Table 1 when patients were divided into two groups as AA and CA, in CA cases, NLR, PLR, CRP, SII, WBC levels were found to be statistically significantly higher, while LCRP and lymphocyte values were lower. Additionally, it was determined that CA cases were significantly older.

As shown in Table 2, when comparing the CA and NCA patient groups in terms of gender ratio, no statistically significant difference was obtained. However, among 105 patients who presented in 2019, KA was detected in 27 (25.7%), while among 118 patients who presented in 2020, KA was identified in 30 (23%). The mean length of hospital stay (LOS) was 2 (1-12) days, and it was determined that CA cases stayed in the hospital for a longer period.

A total of 179 patients underwent CT scans, and of these patients, 16 had CT reports consistent with CA. Additionally, Table 3 shows that the median AIR and Alvarado scores were 6. When NCA and CA cases were compared based on this value, it was determined that the appendicitis scores of CA cases were statistically significantly higher.

Table 2. Comparison of gender, length of stay, and application years in the differentiation of complicated appendicitis.

		Complicated Appendicitis (n: 57)	Non Complicated Appendicitis (n: 166)	*P* Value
Gender	**Male n(%)**	41 (71.9)	101 (60.8)	0.180
	Female n(%)	16 (28.1)	65 (39.2)	
Length of Stay n(min-max)		3 (1-12)	2 (1-12)	**<0.001**
Application Year	**2019**	27	78	0.960
	2020	30	88	

The initial AIR score of the CA was significantly higher than NCA (8, [range, 3–10] vs. 6 [range, 1–10], P < .001). The initial Alvarado score of the CA was significantly higher than NCA (6, [range, 2-9] vs. 6 [range, 1–10], P=0.017).

Table 3.Comparison of clinical scoring in the differentiation of complicated appendicitis

	Complicated Appendicitis (n: 57)	Non Complicated Appendicitis (n: 166)	*P* Value
AIR Score	8 (3-10)	6 (1-10)	**<0.001**
Alvarado Score	6 (2-9)	6 (1-10)	**0.017**

In Table 4, when the cutoff values for diagnostic tests to determine whether cases are CA or not are provided, the sensitivity of CT is 30.7%, the specificity is 96.9%, and the accuracy rate is 77.6%. These rates, when an AIR score of ≥6 is considered, are 85.9%, 47.9%, and 57.5%, respectively. When an Alvarado score of ≥6 is considered, these rates are 80.6%, 44.5%, and 54.9%, respectively. When LCRP is ≤0.1, these rates are 78.9%, 89.7%, and 87%, respectively. When NLR is ≥8.2, these rates are 64.9%, 77.1%, and 73.9%, respectively.

In ROC curve analysis, the closer the area under the curve (AUC) of a tested parameter is to 1, the more important the marker is in predicting the complication. In this study, for predicting complications, the AUC of LCRP was 0.782 (95% CI, 0.711-0.847, p: 0.00), the AUC value of CRP was 0.765 (95% CI 0.697-0.833; p: 0.00), the AUC value of AIR score was 0.748 (95% CI, 0.675-0.821; p: 0.00), the AUC value of NLR was 0.664 (95% CI, 0.585-0.743, p: 0.01), the AUC value of SII was 0.644 (95% CI, 0.565-0.723; p: 0.00) and the AUC value of Alvarado score was 0.605 (95% CI, 0.527-0.683; p: 0.1). This is shown in Figure 1

Table 4. Diagnostic effectiveness of parameters in the differentiation of complicated appendicitis

CT	Complication Present	No Complication	Sensitivity	Specificity	Accuracy	PPV	NPV
Positive	16	4	30.7%	96.9%	77.6%	80%	77.3%
Negative	36	123					
AIR Score ≥6	Complication Present	No Complication	Sensitivity	Specificity	Accuracy	PPV	NPV
Positive	49	87	85.9%	47.9%	57.5%	36%	90.9%
Negative	8	80					
Alvarado Score ≥6	Complication Present	No Complication	Sensitivity	Specificity	Accuracy	PPD	NPV
Positive	44	92	80.6%	44.5%	54.9%	36.9%	85%
Negative	13	74					
LCRP ≤0.1	Complication Present	No Complication	Sensitivity	Specificity	Accuracy	PPV	NPV
Positive	45	17	78.9%	89.7%	87.0%	72.5%	92.5%
Negative	12	149					
SII ≥2300	Complication Present	No Complication	Sensitivity	Specificity	Accuracy	PPV	NPV
Positive	23	36	40.3%	78.3%	68.6%	38.9%	79.2%
Negative	34	130					
NLR ≥8.2	Complication Present	No Complication	Sensitivity	Specificity	Accuracy	PPV	NPV
Positive	37	38	64.9%	77.1%	73.9%	49.3%	86.4%
Negative	20	128					
PLR ≥182	Complication Present	No Complication	Sensitivity	Specificity	Accuracy	PPV	NPV
Positive	24	45	42.1%	72.8%	65.0%	34.7%	78.5%
Negative	33	121					

*CT: Computed Tomography, AIR score: Appendicitis Inflammatory Response Score, LCRP: Lymphocyte / C-Reactive Protein Ratio, SII: Systemic Immune Inflammation Index, NLR: Neutrophil / Lymphocyte Ratio, PLR: Platelet / Lymphocyte Ratio
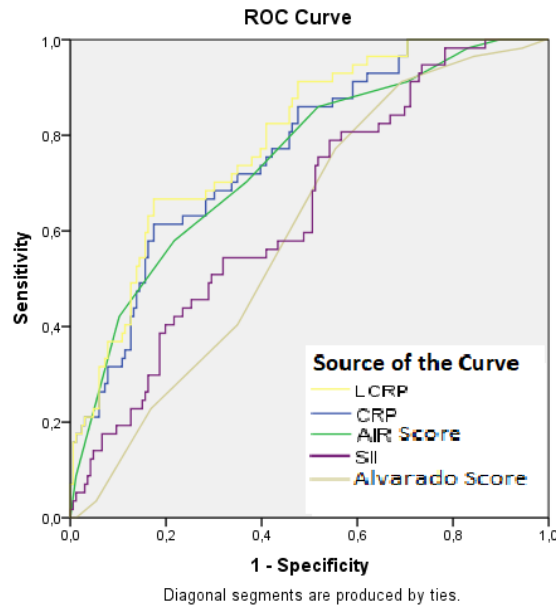
Figure 1. ROC Analysis Showing the Relationship Between AIR and Alvarado Scores, CRP, LCRP and SII Values And Complicated Appendicitis.

DISCUSSION

The aim of this study is to identify parameters that could help distinguish between CA and NCA in patients undergoing surgery in the ED with a diagnosis of acute AA. According to the results obtained from the study, WBC, NLR, PLR, LCRP, and SII were found to be statistically significant in determining the differences between CA and NCA in patients diagnosed with AA in the ED. The specificity of CT was 97%, the sensitivity of the AIR score was 86%, the sensitivity of the Alvarado score was 81%, the specificity of LCRP was 90%, the specificity of SII was 78%, the specificity of NLR was 77%, and the specificity of PLR was 73%. Additionally, while the AIR score was identified as the most sensitive indicator, CT was found to be the most specific screening tool for distinguishing between CA and NCA.

When the literature is reviewed, it is observed that CA cases are more frequently encountered in pediatric, elderly, and male patient groups (7; 8). Similarly, in this study, it was found that the majority of CA cases were male, and the average age was significantly higher compared to the NCA group, which is consistent with the literature. This situation is thought to be related to delayed diagnosis in the elderly patient group due to atypical presentation and less pronounced clinical symptoms, which may lead to more frequent complications.

In a study conducted in 2022 covering 449 patients, it was determined that the CA group had a LOS hospital stay duration 6 times longer (9). Similarly, in this study, it was found that the LOS hospital in CA

cases was longer compared to NCA cases. The reason for this could be the possibility of pathogens to contaminate the surgical area.

There are numerous studies that have demonstrated the relationship between hematologic parameters in patients with AA and underlying inflammatory or infectious processes (8; 10). The elevation of WBC counts in AA cases has thoroughly studied. While an increase in WBC count is commonly encountered in the diagnosis of AA, it has low diagnostic value when used alone. Additionally, other inflammatory conditions may also lead to elevated WBC counts in differential diagnosis (11). In cases without complications such as perforation and periappendicular abscess, the WBC count typically ranges between 10,000 and 18,000 (12). Left shift, often accompanied by leukocytosis, is present in approximately 80-90% of cases. In NCA cases, the WBC count is not expected to be above 18,000 (13). Yang et al. (10) have noted that the increase in leukocytes and the percentage of neutrophils are related to the degree of appendix inflammation. In a study conducted in 2018 with 576 patients, it was found that the WBC value is a useful parameter for distinguishing between CA and NCA patient groups (8). Similarly, in this study, it was found that there was a statistically significant difference in the averages of WBC and neutrophil values in the distinguishing between CA and NCA.

Kahramanca et al. (14) reported that NLR is a valuable parameter for both diagnosing AA and distinguishing between CA and NCA. In a meta-analysis that examined the role of NLR in the differentiation of AA, CA, and NCA in 8914 patients, a threshold value of 8.8 yielded 76.9% sensitivity and an AUC of 0.91 with 100% specificity for CA (15). In this study as well, the mean NLR of CA patients was significantly higher than that of the NCA group. NLR with a cutoff value of 8.2 was found to have 64.9% sensitivity and 77.1% specificity. The increase in WBC and neutrophil values and the decrease in lymphocyte values were found to be significant. It is suggested that evaluating NLR would be more useful in distinguishing between CA and NCA rather than considering only WBC or neutrophil values.

The PLR value, calculated by dividing the platelet count by the lymphocyte count, is reported to be a potential important marker in determining the diagnosis of CA (16). In a study covering 334 pediatric patients diagnosed with AA and undergoing surgery, the group of patients with a higher PLR ratio was found to have a higher likelihood of developing complications, and PLR was found to have a sensitivity of 42% and a specificity of 86% (17). In this study as well, for a PLR value ≥182, the sensitivity was 42.1% and the specificity was 72.8%. The mean PLR in CA cases was found to be significantly higher than in NCA cases.

CRP, first defined in 1930, was later recognized as an acute-phase protein serving as an early indicator of inflammatory processes (18). In their research conducted in 2021, Fujiwara et al. (19) found that high serum CRP levels were significantly associated with CA. In this study as well, a statistically significant difference in CRP, a valuable acute-phase reactant, was obtained between the CA and NCA groups.

The LCRP value, obtained by dividing the lymphocyte count by the CRP value, and SII are considered parameters that increase in many inflammatory and infectious disease processes and play a role in

determining disease severity and predicting mortality (20). Acar et al. (21), in their study on patients diagnosed with community-acquired pneumonia, found a threshold of 4 for LCRP to predict 28-day mortality, with a sensitivity of 89% and specificity of 73%. They also determined a threshold of >3551 for the SII parameter, which yielded 63.8% sensitivity and 68.1% specificity in predicting mortality and considered them valuable markers in assessing disease severity. In this study, when the cutoff value for LCRP was set at 0.1 in CA cases, it resulted in 78.9% sensitivity and 89.7% specificity. When a cutoff of 2300 or higher was used for SII in distinguishing between CA and NCA cases, it resulted in 40.3% sensitivity and 78.3% specificity. Decreased LCRP and increased SII were found meaningful. There is no known study in the literature that has examined this aspect of the topic. Therefore, further research to support the findings would be beneficial.

During the COVID-19 pandemic, it has been reported that there is a higher rate of CA due to delays in the time between the onset of symptoms and presentation to the ED (22). Wang et al. (23) in their research reported that patients could delay seeking medical attention for COVID-19 due to the fear of transmission, and as a result, there could be an increase in the number of CA cases. However, in this study, there was a slight increase in the number of CA cases during the pandemic period, but no statistically significant difference was observed. This may be attributed to the perception of abdominal pain as a serious condition in our country and early presentation to the ED.

The diagnosis of AA is subjective as it is associated with multiple parameters, and clinical scoring systems can make the diagnostic process more objective. AIR and Alvarado are among these scoring systems (7). In a study conducted with 578 patients in 2018, the AIR and Alvarado scoring systems were compared for distinguishing between CA and NCA, and the AIR score was found to be more significant in predicting CA and appendix diameter (24). In a retrospective analysis of two cohorts from referral centers in Switzerland and Germany, it was stated that the highest Alvarado and AIR scores with >90% sensitivity for detecting CA were ≥5 and ≥3, respectively (25). In this study, when the total scores were ≥6, the AIR score had a sensitivity of 85.9% and specificity of 47.9%, while the Alvarado score had a sensitivity of 80.6% and specificity of 44.5%. Additionally, both AIR and Alvarado scoring systems were found to significantly distinguish between CA and NCA cases.

It has been reported that CT, one of the imaging methods used for the diagnosis of AA, has a sensitivity of 98% and a specificity of 98% (24). Tsuboi et al. (26) found a sensitivity of 95% and a specificity of 97% for CT in detecting perforated appendicitis. In this study, the sensitivity of CT in detecting perforated appendicitis was found to be 31%, while the specificity was 97%. This is attributed to radiologists interpreting CT scans focusing more on the diagnosis of AA rather than complications.

Limitations

The study is designed retrospectively, and has some limitations. Since it's a single-center study, further research is needed to apply the results to the general population. Information about the time interval between

patients being diagnosed with acute appendicitis (AA) and their presentation to the emergency department, followed by surgery, is not available. During this elapsed time, the possibility of complications should be considered. Therefore, it cannot be predicted at which stage of inflammation the detection occurred.

CONCLUSION

Many factors influence the differentiation between CA and NCA. Inflammatory markers are important parameters in distinguishing between CA and NCA. This study has shown that values such as LCRP, SII, NLR, and PLR may be useful markers in differentiating CA from NCA. Additionally, it has been concluded that the diagnostic process can be strengthened by using AIR and Alvarado scores and CT in addition to these markers.

Acknowledgments
This study represents the transformed version of researcher's thesis.

Authorship contributions
All authors contributed equally to the writing of this paper.

Data availibity statement
Data available on request.

Declaration of competing interest
All authors declare no potential conflicts of interest in this study.

Ethics
The ethics committee approval for the study was obtained Mugla Sıtkı Kocman Univesity Clinical Research Ethics Committee (30/11/2021).

Funding
This study was not funded by any institution or organization.

REFERENCES

1. Natesan S, Lee J, Volkamer H, Thoureen T. Evidence-Based Medicine Approach to Abdominal Pain. Emerg Med Clin North Am. 2016 May; 34(2):165-90.
2. Abdolrazaghnejad A, Rajabpour-Sanati A, Rastegari-Najafabadi H, Ziaei M, Pakniyat A. The Role of Ultrasonography in Patients Referring to the Emergency Department with Acute Abdominal Pain. Adv J Emerg Med. 2019 May; 3(4):e43.
3. Körner H, Söndenaa K, Söreide JA, Andersen E, Nysted A, Lende TH, et al. Incidence of acute nonperforated and perforated appendicitis: age-specific and sex-specific analysis. World J Surg. 1997 Mar-Apr; 21(3):313-7.
4. Bickell NA, Aufses AH Jr, Rojas M, Bodian C. How time affects the risk of rupture in appendicitis. J Am Coll Surg. 2006 Mar; 202(3):401-6.

5. Liang MK, Andersson RE, Jaffe BM, Berger DH. The Appendix. In: Brunicardi FC, Andersen DK, Billiar TR, Dunn DL, Hunter JG, Matthews JB, et all editors. Schwartz's Principles of Surgery. 10ed. New York, McGraw-Hill Education; 2014.p.1241-1262.

6. Young P. Appendicitis and its history. Rev Med Chil, 2014. 142(5): p. 667-72.

7. Cormier JN, Gronchi A, Pollock RE. Appendix. In:Brunicardi FC, Andersen DK, Billiar TR, Dunn DL, Hunter JG, Schwartz SI, editors. Schwartz's principles of surgery. Tenth edition. New York London : McGraw-Hill Education / Medical;2014.

8. Dinç T, Sapmaz A, Erkuş Y, Yavuz Z. Complicated or non-complicated appendicitis? That is the question. Ulus Travma Acil Cerrahi Derg. 2022 Mar;28(3):390-394.

9. Alotaibi AM, Alfawaz M, Felemban L, Moshref L, Moshref R. Complicated appendicitis increases the hospital length of stay. Surg Open Sci. 2022 May 20;9:64-68.

10. Yang HR, Wang YC, Chung PK, Chen WK, Jeng LB, Chen RJ. Laboratory tests in patients with acute appendicitis. ANZ J Surg. 2006 Jan-Feb;76(1-2):71-4.

11. Kaplan GG, Pedersen BV, Andersson RE, Sands BE, Korzenik J, Frisch M. The risk of developing Crohn's disease after an appendectomy: a population-based cohort study in Sweden and Denmark. Gut. 2007 Oct;56(10):1387-92.

12. Aren A, Gökçe A, Gökçe F, Özakay K, Aksoy Ş, Karagöz B ve ark. Akut apandisitin yaş, cinsiyet, lökosit değerleri ile ilişkisi. İstanbul Tıp Dergisi. 2009;10(3):126-129.

13. Brunicardi F, Andersen D, Billiar T, Dunn D, Hunter J, Matthews J. Schwartz's principles. 10th ed. New York: McGraw-hill; 2014.

14. Kahramanca S, Ozgehan G, Seker D, Gökce EI, Seker G, Tunç G et al. Neutrophil-to-lymphocyte ratio as a predictor of acute appendicitis. Ulus Travma Acil Cerrahi Derg. 2014 Jan;20(1):19-22.

15. Hajibandeh S, Hobbs N, Mansour M. Neutrophil-to-lymphocyte ratio predicts acute appendicitis and distinguishes between complicated and uncomplicated appendicitis: A systematic review and meta-analysis. Am J Surg. 2020 Jan;19(1):154-163.

16. Rajalingam VR, Mustafa A, Ayeni A, Mahmood F, Shammout S, Singhal S, et al. The Role of Neutrophil-Lymphocyte-Ratio (NLR) and Platelet-Lymphocyte-Ratio (PLR) as a Biomarker for Distinguishing Between Complicated and Uncomplicated Appendicitis. Cureus. 2022 Jan;14(1):e21446.

17. Celik B, Nalcacioglu H, Ozcatal M, Altuner Torun Y. Role of neutrophil-to-lymphocyte ratio and platelet-to-lymphocyte ratio in identifying complicated appendicitis in the pediatric emergency department. Ulus Travma Acil Cerrahi Derg. 2019 May;25(3):222-22.

18. Clyne B, Olshaker JS. The C-reactive protein. J Emerg Med. 1999 Nov-Dec;17(6):1019-25.

19. Fujiwara K, Abe A, Masatsugu T, Hirano T, Hiraka K, Sada M. Usefulness of several factors and clinical scoring models in preoperative diagnosis of complicated appendicitis. PLoS One. 2021 Jul;16(7):e0255253.

20. Acar E, Demir A, Yıldırım B, Kaya MG, Gökçek K. The role of hemogram parameters and C-reactive protein in predicting mortality in COVID-19 infection. Int J Clin Pract. 2021 Jul;75(7):e14256.

21. Acar E, Gokcen H, Demir A, Yildirim B. Comparison of inflammation markers with prediction scores in patients with community-acquired pneumonia. Bratisl Lek Listy. 2021;122(6):418-423.

22. Kariya A, Krutsri C, Singhatas P, Sumritpradit P, Thampongsa T, Lertsitthichai P, et al. Incidence of complicated appendicitis during the COVID-19 pandemic: A systematic review and meta-analysis. Int J Surg Open. 2022 Aug;45:100512.

23. Wang AW, Prieto J, Ikeda DS, Lewis PR, Benzer EM, Van Gent JM. Perforated Appendicitis: An Unintended Consequence During the Coronavirus-19 Pandemic. Mil Med. 2021 Jan;186(1-2):e94-e97.

24. Yeşiltaş M, Karakaş DÖ, Gökçek B, Hot S, Eğin S. Can Alvarado and Appendicitis Inflammatory Response scores evaluate the severity of acute appendicitis? Ulus Travma Acil Cerrahi Derg. 2018 Nov;24(6):557-562.

25. Haak F, Kollmar O, Ioannidis A, Slotta JE, Ghadimi MB, Glass T, et al. Predicting complicated appendicitis based on clinical findings: the role of Alvarado and Appendicitis Inflammatory Response scores. Langenbecks Arch Surg. 2022 Aug;407(5):2051-2057.

26. Tsuboi M, Takase K, Kaneda I, Ishibashi T, Yamada T, Kitami M, et al. Perforated and nonperforated appendicitis: defect in enhancing appendiceal wall-depiction with multi-detector row CT. Radiology. 2008 Jan;246(1):142-7.

Research Article

AGMATINE ADMINISTRATION ALLEVIATES NERVE DAMAGE AND IMPROVES NERVE FUNCTION IN METHOTREXATE-INDUCED PERIPHERAL NEUROPATHY IN RATS

Hatice Fulya YILMAZ [1], Özlem BOZKURT GİRİT [2, *]

[1] Aydın Adnan Menderes University, Institute of Health Sciences, Department of Biophysics, Aydın, TURKIYE
[2] Aydın Adnan Menderes University, School of Medicine, Department of Biophysics, Aydın, TURKIYE

Correspondence: ozlem.bozkurt@adu.edu.tr

ABSTRACT

Objective: Chemotherapeutic agents can produce neurodegenerative changes. This study was conducted to assess the therapeutic potential of agmatine, a neuromodulator, on methotrexate induced neurodegeneration in sciatic nerve.

Materials and Methods: 40 male Wistar albino rats were assigned into four groups at random as control, methotrexate, agmatine and methotrexate-agmatine. Methotrexate was injected intraperitoneally at a 37.5 mg/kg/week dose for 3 weeks. Afterwards, agmatine was administered intraperitoneally twice a day at a 40 mg/kg dose for 7 days. Sciatic functional index, nociceptive pain perception and behavioral changes were analyzed every week. Nerve conduction velocity was evaluated. Apoptotic activity and mitophagy, histopathological changes in sciatic nerves were examined.

Results: Methotrexate administration resulted in a prolonged escape time to the platform and decreased the time spent in the quadrant in the water maze test; elevated nociceptive latencies; decreased the number of frames passed in the open field test; reduced sciatic NCV and SFI score. Besides, methotrexate administration caused a reduction in myelin thickness and axon diameter in sciatic nerve and a more intense glial fibrillary acidic protein immunoreactivity. Methotrexate administration triggered an increase in the Bax/Bcl2 protein expression ratio without changing the expression level of Parkin, indicating a slight apoptotic activation. agmatine administration improved methotrexate induced changes in behavioral performances, nociceptive pain perception, nerve conduction, SFI scores and histopathological changes.

Conclusion: Agmatine has been demonstrated to possess a therapeutic potential in methotrexate induced degeneration and peripheral neuropathy in the rat sciatic nerve.

Keywords: Methotrexate, Agmatine, Sciatic nerve, Peripheral neuropathy

INTRODUCTION

Methotrexate (MTX) is a folic acid analog and a first-line synthetic antimetabolite commonly used in the treatment of cancer types affecting the nervous system and certain chronic autoimmune inflammatory diseases (1). Serious side effects associated with MTX use include progressive hepatotoxicity and nephrotoxicity, peripheral neuropathy, axonopathy, and varying degrees of demyelination. Due to these severe consequences, it may be necessary to adjust the treatment dose or even discontinue the medication, which can lead to incomplete treatment and serious health issues for many patients (2). Some of these conditions, especially neuropathy and demyelination induced by MTX usage, may last for several years adversely affecting patient welfare. Although the adversative effects of MTX administration on central nervous system has been of great concern, little is known on the effects of MTX administration on peripheral nervous system. Whilst, when MTX use is unavoidable, it is crucial to develop methods to prevent and/or treat probable peripheral nervous system degeneration. The long-term use of chemotherapeutic agents at high therapeutic levels was stated to affect the plasticity of the nervous system leading to irreversible neuronal damage (3) and neuropathic pain.

Agmatine (AgM) is an endogenous neuromodulator known for modulating various functions both in central and peripheral nervous system. As it possesses N-methyl-D-aspartate receptor (NMDAR) antagonist and nitric oxide synthase (NOS) inhibitor activities (4), the studies on the effect of AgM on peripheral nervous system have been focused on its role in the modulation of neuropathic pain and its antinociceptive function. AgM was reported to play an antiplasticity and antinociceptive role to reverse pain induced by cisplatin-induced neuropathy (5) peripheral nerve injury (6, 7), inflammation and spinal cord injury (7). Additionally, AgM has been reported to enhance cognitive functions through its analgesic, anti-inflammatory, and neuroprotective effects, and it has been suggested to be beneficial in the treatment of neurodegenerative diseases (4, 7). Consequently, this study was addressed to evaluate the remedial potential of AgM on peripheral nervous system neuropathy or degeneration induced by MTX.

MATERIALS AND METHODS

Animals

All experimental procedures to be applied were firstly approved by the Adnan Menderes University Experimental Animal Ethics Committee with an approval number 64583101/2020/074 and the experiments were accomplished in compliance with ethical guidelines. 11-week old adult male Wistar-albino rats (n = 40) (250-300 g) were maintained in a controlled ambient environment and were assigned randomly into four experimental groups, each consisting of 10 animals, namely a control group (C), a MTX administered group (MTX), an only AgM administered group (AgM) and a group where the rats recieved AgM after MTX

administration. Figure 1 demonstrates the time schedule of drug administrations and the measurements performed by the use of the animals belonging to experimental groups.
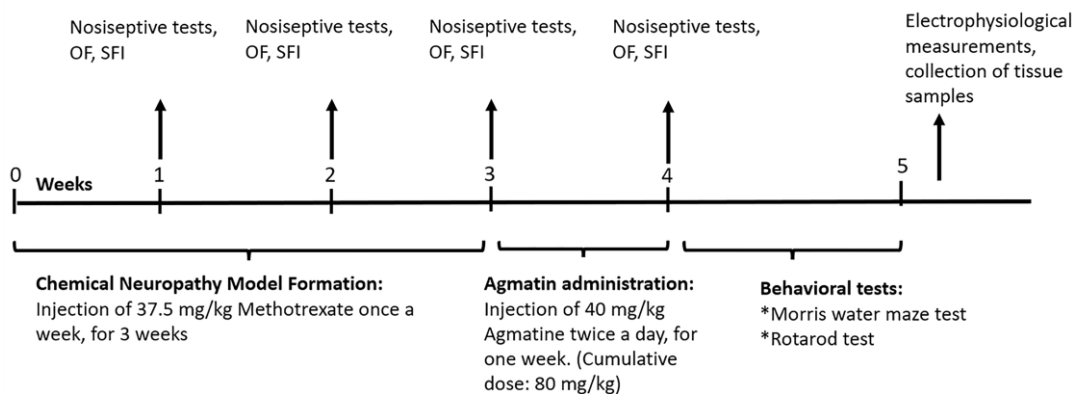

Figure 1. Schematic diagram demonstrating the timing of experimental procedures applied on rats.

Drugs and their administration

In order to achieve a rat model of methotrexate-induced neuropathy, MTX (item no: BD43028, BLD pharm, China) was administered to MTX and MTX-AgM groups at a dose of 37.5 mg/kg, dissolved in physiological saline and injected (i.p.) once a week for 21 days (8). Following the neuropathy induced by methotrexate injection over a period of three weeks, the treatment groups (AgM and MTX-AgM) were administered with a 40 mg/kg dose of AgM (item no: BD112829, BLD phram, China), dissolved in physiological saline and injected (i.p.) twice a day (at a 12-hour interval) for seven days (9).

Nociceptive tests

Hot plate and tail flick tests were applied as nociceptive tests at the end of the first and third weeks of MTX administration and at the end of the week of Agmatine administration (on the fourth week). In the tail-flick test, a beam of radiant heat was focused on the lower one-third portion of the tail via an automated device (May Tic., Ankara, Türkiye), and the latency for a tail withdrawal upon thermal stimulation was recorded in seconds. In the hot-plate test, the rats were placed onto a preheated ($55 \pm 0.3°C$) plate (May Tic., Ankara, Türkiye) and the time needed for a response, for instance licking the hind legs or jumping, to the thermal stimulation was documented. With the aim of avoiding irreversible injury, the cut-off time was set to 10 s in both tests.

Sciatic functional index (SFI)

Sciatic Function Index (SFI) was measured once a week for five weeks. The hind paws of the animals were coated with blue ink and the animal was let to move freely on a blotting paper. The paw-prints were then used to calculate the SFI where at least three paw prints were evaluated per animal in a single

measurement. Before the drug administrations started, paw-prints collected from all animals were considered as the healthy prints for calculations, and the paw-prints of every animal was compared to this first collected healthy paw-print of the same animal throughout the drug administration period. The paw-prints were loaded to ImageJ-Win64 program (NIH, USA) and the following distances were measured: the 3rd toe-to-heel distance (NPL) for the healthy foot, the 1st to 5th toe distance (NTS) for the healthy foot, the 2nd to 4th toe distance (NITS) for the healthy foot, the 3rd toe-to-heel distance (EPL) for the damaged foot, the 1st to 5th toe distance (ETS) for the damaged foot, and the 2nd to 4th toe distance (EITS) for the damaged foot. The 'multiple linear regression formula' was used in the SFI calculation as previously reported (10,11).

Behavioral analyses

Open Field Test: All experimental groups were tested with the open field test once a week throughout the duration of the experiment. The platform for the open field test is a 20 x 20 cm area with a white floor divided into a total of 16 squares by black lines. Each rat was placed on the open field platform from the same corner square of the platform. For each rat, a 2-minute observation period was recorded with a camera. During this period, the total number of squares the rat crossed, as well as the frequency of rearing and grooming, were recorded and scored (12). The locomotor activities of the rats were assessed using the data obtained from the open field test.

Rotarod test: The test was executed at the fifth week of experiments, after the cessation of AgM administration. The rats were separately placed on the rotating rod of the platform (at a speed of 5 rpm), and their latencies to fall from the rotarod platform were recorded in a 1-minute period, and their latencies to fall from the rotarod platform were recorded and analyzed with a video camera (13). Data obtained from the rotarod test were used to evaluate the balance, coordination, and locomotor activities of the rats.

Morris's water maze (MWM) test: A circular swimming pool (150 cm in diameter with 60 cm depth) was allocated into four equal quadrants, where different symbols were assigned to each quadrant and a transparent hidden platform was placed in the pool, submerged 2 cm below the surface in one quadrant. The rats were placed in the pool facing different quadrants each time, and a total of 4 trials were conducted. The escape latencies of the rats to the hidden platform in the designated quadrant were recorded with a stopwatch, and this phase of the experiment was repeated for four days. On the fifth day, the hidden platform was removed, and the time spent by the rats in the previously designated quadrant was recorded. All MWM test trials were recorded with a video camera to confirm the measured latencies. The escape latencies to the

platform during the first four days and the time spent in the designated quadrant after the removal of the platform on the fifth day were evaluated to determine the learning and memory abilities of the rats (14).

Electrophysiological measurements

Electrophysiological measurements were performed using a four-channel clinical electromyography (EMG) device (4-channel Nicolet Viking Quest VIASYS, Natus Medical Inc., CA, USA) at the Faculty of Veterinary Medicine, Aydın Adnan Menderes University. For the electrophysiological measurements, the rats were anesthetized with an intraperitoneal injection of ketamine (50 mg/kg) and xylazine (10 mg/kg). Then the hind limbs were shaved starting from the point where the femur meets the hip joint to the point corresponding to the back of the femoral knee joint, and cleaned. The measurements were performed using reusable surface electrodes. The active recording electrode was placed in the center of the plantar surface of the paw, the reference electrode was placed on the heel, and the ground electrode was positioned at the base of the tail. Two electrical stimulations were applied by a small bipolar surface electrode (Natus Medical Incorporated, Pleasanton, CA, USA) from a proximal and a distal stimulation point. Proximal stimulation was applied from the point aligned with the hip end of the femur, and distal stimulation was applied from the point aligned with the back of the knee joint of the femur. The EMG device settings and amplifier filter settings were adjusted to 10 Hz-10 kHz, sweep speed to 1 ms, stimulation duration to 0.5 ms, and gain to 2 mV. Electrical stimulations were manually applied at right angles with the respective electrode at random intervals. For each rat, a total of three compound muscle action potential (CMAP) recordings were obtained in response to the proximal and distal stimulations, and the averages of the calculations were considered in data analysis. From the CMAP recordings, proximal and distal latencies (ms), total CMAP duration (ms) and peak-to-peak amplitude (mV) were analyzed using the VIASYS Nicolet Viking Quest software program. The sciatic nerve motor nerve conduction velocity was calculated by taking the ratio of the distance between the stimulating electrodes to the difference between the proximal and distal latencies.

Afterwards, the animals were sacrificed and sciatic tissue samples were dissected from both limbs. The right sciatic nerves to be used in histological analysis were placed into 10% formalin for fixation. The left sciatic nerves were stored at -80°C until further usage in Western blot analysis.

Western blot analysis

For the determination of protein expression levels, sciatic nerves were homogenized by sonication in a 5X (w:v) RIPA lysis buffer (Catalog # 20188, Merck Millipore, Germany) containing a 1:10 (v:v) protease inhibitor cocktail (Catalog # K297, BioVision, USA) and sonicated (HD2200, Bandelin SONOPULS, Germany) on ice until the tissue was homogenized. Then homogenates were centrifuged at 16.000 g for 10 minutes at 4°C to collect the supernatants. The protein concentration in lysates was determined by using Bradford assay kit (Catalog # P010A, ABY Bioscience, USA). Tissue lysates were then mixed with 6 µl loading dye (Catalog # 751-

00, Pagesta, 5X SDS-PAGE sample buffer, Korea) and boiled at 95°C for 5 min. Each sample containing an equal amount of protein (30 µg) was loaded onto the polyacrylamide gel (4 and 12% stacking and resolving gels, respectively), underwent gel electrophoresis, transferred onto polyvinylidene fluoride membranes (Catalog # D9160172A, Bio-Rad, USA) and blocked. The membranes were then incubated with primary antibodies against Bcl-2 (1:1000, Catalog # bsm-3304M, Bioss, USA), Bax (1:1000, Catalog # bsm-33283M, Bioss, USA), Parkin (1:1000, Catalog # 4211S, Cell signaling, Netherlands), and β-Actin (1:1000, Catalog # sc-47778, Santa Cruz, USA), at 4℃ overnight. After washing, the membranes were incubated with the secondary antibody (1:5000, anti-mouse IgG HRP, Catalog # 7076S, Cell Signaling, Netherlands) at room temperature for 2 h. Afterwards the membrane was washed, added with the ECL substrate (Catalog #1705060, BIO-RAD, California, USA) to be visualized using the UVP system (G:Box Syngene, DR4V/1309, UK) with antibody-specific varying exposure times. The protein band intensities were measured by the usage of ImageJ (MD, USA, 64-bit version) software. The expression level of each protein was compared to that of β-actin (reference protein).

Histological analysis

The formalin was removed from the fixated right sciatic nerves under running water and the tissues were dehydrated through passages of ethanol (Catalog # UN1170, Isolab, Germany). Subsequently, the tissues were cleared in xylene at 60°C (Catalog # 108297, Merck, Germany) and infiltrated with paraffin (Catalog # 8002-74-2, Tekkim, Türkiye) and embedded in paraffin blocks. 5 µm thick serial sections were obtained from the blocks via a rotary microtome (RM 2265, Leica, Germany) with a microtome blade (Catalog # 3051835, Thermo Fisher MX35 Premier, Singapore). Paraffin sections obtained from the sciatic nerve tissue were stained using histochemical methods with Hematoxylin (Catalog # RRSP67-E, Atom Scientific, United Kingdom) & Eosin (Catalog #RRSP35-E, Atom Scientific, United Kingdom), Luxol Fast Blue (Catalog # RRSK345-100, Atom Scientific, United Kingdom), and Masson Trichrome (Catalog # RRSK20-100, Atom Scientific, United Kingdom). Additionally, immunohistochemical staining was performed using GFAP Rabbit monoclonal primary antibody (Catalog # bsm-52254R, Bioss, USA). The stained sections were visualized using an Olympus CX21 microscope (Olympus, Japan). The LFB stained images were further loaded to ImageJ (NIH, USA, 64-bit version) software program and myelin sheath thickness, axon and myelinated fiber diameter in the sections were calculated.

Statistical analysis

The data obtained in the study were expressed mean ± standard error of mean (SEM) and analyzed via SPSS Statistics software (version 26.0, IBM, USA). Kolmogorov-Smirnov test was used to confirm that the data exhibited a normal distribution. Intergroup comparisons of normally distributed data were accomplished via Student's t-test or One-way ANOVA and Tukey's test was performed as a post-hoc test, while non-normally

distributed data were compared using non-parametric Kruskal-Wallis test. A p value equal to or less than 0.05 was accepted as statistically significant. For the denotation of the degree of significance, an asterisk (*) was used for the comparisons of all groups with regard to the control (C); a dagger (†) was used for comparisons with regard to the MTX administered group; and a hashtag (#) was used for comparisons with respect to the AgM treatment group. (*p<0.05, **p<0.01, ***p<0.001).

RESULTS

Nociceptive pain perception

The results from the nociceptive tests showed that a 3-week administration of MTX led to significantly prolonged latencies of responses to thermal painful stimuli when compared to that of control (Table 1). This result indicates a decrease in thermal pain perception due to MTX administration. It was observed that AgM treatment after MTX administration (MTX-AgM group) resulted in a reduction in the latencies of hot plate and tail flick responses to thermal painful stimuli compared to the MTX-treated groups (p<0.05) (Table 2).

Table 1. Results of the nociceptive tests recorded as latency (s) of a reaction given in response to thermal painful stimuli during the 3-week period of chemical neuropathy induction induced by MTX.

		Latency (s)	
Nociceptive Test	Groups	1st week	3rd week
Hot Plate	C	5.85 ± 0.28	5.75 ± 0.25
	MTX	7.65 ± 0.39***	7.94 ± 0.28***
Tail Flick	C	6.49 ± 0.15	6.54 ± 0.12
	MTX	6.79 ± 0.13	7.49 ± 0.12***

The data were represented as mean ± standard error of mean. Differences in means were compared by student t-test. P-values equal or less than 0.05 were considered as statistically significant (*p<0.05, **p<0.01, ***p<0.001). The degree of significance was symbolized with asterisks (*) for the comparisons to that of control group (C).

Sciatic functional index (SFI)

Figure 2a-2d demonstrates the paw-prints obtained from the experimental groups and Figure 2e shows the results of the 5-week SFI analysis. In the measurements taken over five weeks, no treatment was applied to the experimental groups during the first week. In the SFI measurements taken at the end of the 2nd and 3rd weeks, where only MTX was administered to relevant groups, as well as those taken in the 4th week, a statistically significant reduction in SFI values was observed in the MTX and MTX-AgM groups compared to that of control (p<0.001).
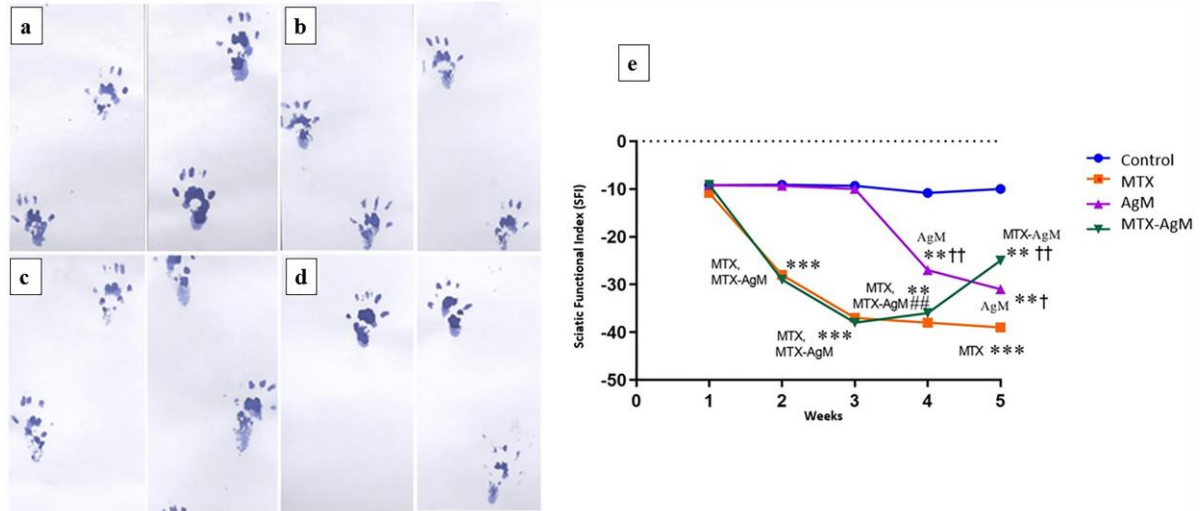
Figure 2. Representative photographs of the paw-prints of rats in a) Control group, b) MTX group, c) AgM group, d) MTX-AgM group; and e) the alterations in the SFI values of the experimental groups throughout the study. Data were represented as mean ± standard error of mean. Differences in between variances were compared by One-way ANOVA test with Tukey's test applied as a post-hoc test. A p value equal to or less than 0.05 was accepted as statistically significant (*p<0.05, **p<0.01, ***p<0.001). The degree of significance was indicated by an asterisk (*) for comparisons of all groups with respect to the control (C) group; by a dagger (†) for comparisons with respect to the MTX administered group; and by a hashtag (#) for comparisons with respect to the AgM treatment group.

At the end of the 4th week, where AgM was administered, the SFI values of the MTX and MTX-AgM groups were observed to be close to each other, where the SFI values of both groups were significantly lower compared to that of control (p<0.01) and to that of only AgM administered group (p<0.01). At the end of the 5th week, the SFI values of the MTX group was the lowest among the other experimental groups with a statistically significant difference with respect to control (p<0.001).

Table 2. Results of the nociceptive tests recorded as latency (s) of a reaction given in response to thermal painful stimuli during the 4th week of AgM treatment.

Nociceptive Test	Groups	Latency (s)		
		1st week	3rd week	4th week
Hot Plate	**C**	5.85 ± 0.28	5.75 ± 0.25	5.9 ± 0.26
	MTX	7.65 ± 0.39	7.94 ± 0.28	7.77 ± 0.2***
	AgM	5.96 ± 0.3	5.99 ± 0.28	5.88 ± 0.31†††
	MTX-AgM	7.53 ± 0.39	7.76 ± 0.16	7.13 ± 0.14†
Tail Flick	**C**	6.49 ± 0.15	6.54 ± 0.12	6.48 ± 0.11
	MTX	6.79 ± 0.13	7.49 ± 0.12***	7.64 ± 0.16***
	AgM	6.34 ± 0.05	6.58 ± 0.16	6.43 ± 0.09†††
	MTX-AgM	6.71 ± 0.13	7.03 ± 0.11	6.91 ± 0.21†

The data were represented as mean ± standard error of mean. Differences in between variances were compared by One-way ANOVA test with Tukey's test applied as a post-hoc test. A p value equal to or less than 0.05 was accepted as statistically significant (*p<0.05, **p<0.01, ***p<0.001). The degree of significance was indicated by an asterisk (*) for comparisons of all groups with respect to the control (C) group; by a dagger (†) for comparisons with respect to the MTX administered group (*p<0.05, **p<0.01, ***p<0.001).

However, the SFI values of the MTX-AgM group was observed to be significantly increased at the end of the 5th week with respect to that of MTX (p<0.01) and only AgM administered groups, and the SFI values of the MTX-AgM group were observed to be approaching to that of control. Taking these results into consideration, MTX administration in the first three weeks led to a decrease in sciatic functioning and SFI values, and the treatment of AgM to MTX administered rats led to an increase in sciatic functioning and SFI values at the end of the 5th week. Additionally, AgM administration alone also causes to a decrease in SFI values, even one week after the cessation of the AgM administration.

Electrophysiological recordings

The results of the measurements obtained from CMAP recording are presented in Table 3. As can be seen from the table, there was a significant decrease in nerve conduction velocity in the MTX group (p<0.001) and the MTX-AgM group (p<0.01) compared to that of control, where the NCV of the AgM treated MTX group was slightly higher to that of MTX administered group. It was also observed that the only AgM administered group had a significantly higher nerve conduction velocity compared to the MTX group (p<0.05). The decrease in nerve conduction velocity in the MTX and MTX-AgM groups indicates the presence of myelin damage. The total CMAP duration was observed to be significantly prolonged in the MTX-AgM group compared to the MTX group (p<0.05), with no significant differences observed among other groups. In addition, there was a slight decrease in distal amplitude (peak-to-peak (P-P)) values in the MTX, AgM, and MTX-AgM groups compared to the control group. However, this decrease is not statistically significant. This suggests that axonal damage may have remained at a cellular level.

Table 3. The results of the alterations in motor nerve conduction velocities, peak-to-peak amplitude and duration of the compound muscle action potential recordings (CMAP) of the sciatic nerves in the experimental study groups.

Electrophysiological measurements	Control	MTX	AgM	MTX-AgM
Nerve conduction velocity (m/s)	64.02 ± 0.96	52.46 ± 1.15***	62.48 ± 1.39†††	55.46 ±1.07***
Amplitude (peak-to-peak) (mV)	3.88 ± 0.61	3.33 ± 0.47	2.72 ± 0.36	3.51 ± 0.9
Total CMAP duration (ms)	2.71 ± 0.12	2.68 ± 0.08	3.31 ± 0.22	3.48 ± 0.20†

The data were represented as mean ± standard error of mean. Differences in between variances were compared by One-way ANOVA test with Tukey's test applied as a post-hoc test. A p value equal to or less than 0.05 was accepted as statistically significant (*p<0.05, **p<0.01, ***p<0.001). The degree of significance was indicated by an asterisk (*) for comparisons of all groups with respect to the control (C) group; by a dagger (†) for comparisons with respect to the MTX administered group.

According to the electrophysiological measurement results obtained from the sciatic nerve, MTX treatment led to a reduced nerve conduction velocity and a decreased CMAP duration, while the treatment of AgM following MTX administration increased nerve conduction velocity and CMAP duration, bringing them closer to normal values.

Behavioral analyses

According to the results of the open field test, MTX treatment was found to significantly decrease the line crossing frequency compared to that of control (p<0.001), while AgM treatment after MTX administration significantly increased the line crossing frequency compared to the MTX group (p<0.001), bringing it closer to the control group.

Table 4. Results of the behavioral tests for all experimental groups.

Measurements	Control	MTX	AgM	MTX-AgM
Open Field (OF)				
Line crossing frequency	16.2 ± 0.95	6.5 ± 0.87***	13.5 ± 0.81†††	13.2 ± 0.91†††
Grooming frequency	1.7 ± 0.47	0.7 ± 0.42	2.2 ± 0.38	1.11 ± 0.34
Rearing Frequency	2.7 ± 0.78	2.6 ± 0.54	2.5 ± 0.31	2.1 ± 0.57
Rotarod				
Latency to fall (s)	60.00 (55.00-62.50)	50.00 (45.00-55.00)	60.00 (55.00 - 62.50)	62.50 (50.00 - 57.50)
Morris Water Maze (MWM)				
Platform escape latency (s)	16.7 ± 2.15	26.7 ± 2.84*	17.1 ± 2.09†	19.5 ± 2.63
Time in the quadrant (s)	25.6 ± 1.75	15.22 ± 1.99**	24.6 ± 2.16†	22.8 ± 1.05†

In the open field and rotarod tests, the data were represented as mean ± standard error of the mean. Differences in between variances were compared by One-way ANOVA test with Tukey's test applied as a post-hoc test. In the rotarod test, fall latency data were analyzed using the independent-samples Kruskal-Wallis test and data was expressed as median and interquartile ranges. A p value equal to or less than 0.05 was accepted as statistically significant (*p<0.05, **p<0.01, ***p<0.001). The degree of significance was indicated by an asterisk (*) for comparisons of all groups with respect to the control (C) group; by a dagger (†) for comparisons with respect to the MTX administered group.

However, grooming frequency and rearing frequency remained unchanged among the groups. These results indicated that MTX treatment causes a reduction in locomotor activity, whereas AgM administered after MTX increases locomotor activity (Table 4). MTX treatment adversely affected the rats' ability to learn and retain the location of the hidden platform (p<0.01); however, AgM treatment following MTX administration improved these abilities compared to the MTX group and brought the values closer to those of the control group (p<0.05) in the MWM test (Table 4). Rotarod test results revealed that MTX administration led to a slight decrease in the latency to fall from the apparatus and AgM treatment following MTX administration improved this parameter, however these changes were not statistically significant (Table 4).

Western blot analysis

The expression levels of Bcl-2, Bax and Parkin proteins, in comparison to those of β-actin, were evaluated to obtain information on the apoptotic activation and induction of mitophagy in the sciatic nerves (Figure 3). As seen in the figure, Bcl-2 protein expression was significantly reduced (p<0.05) in the only AgM administered group. The absence of statistically significant differences in Bcl-2 protein expression levels, which plays a role in the anti-apoptotic pathway and suppresses apoptotic pathway activation, in the MTX-treated groups suggests that applied MTX dose or duration was not able to suppress apoptosis.
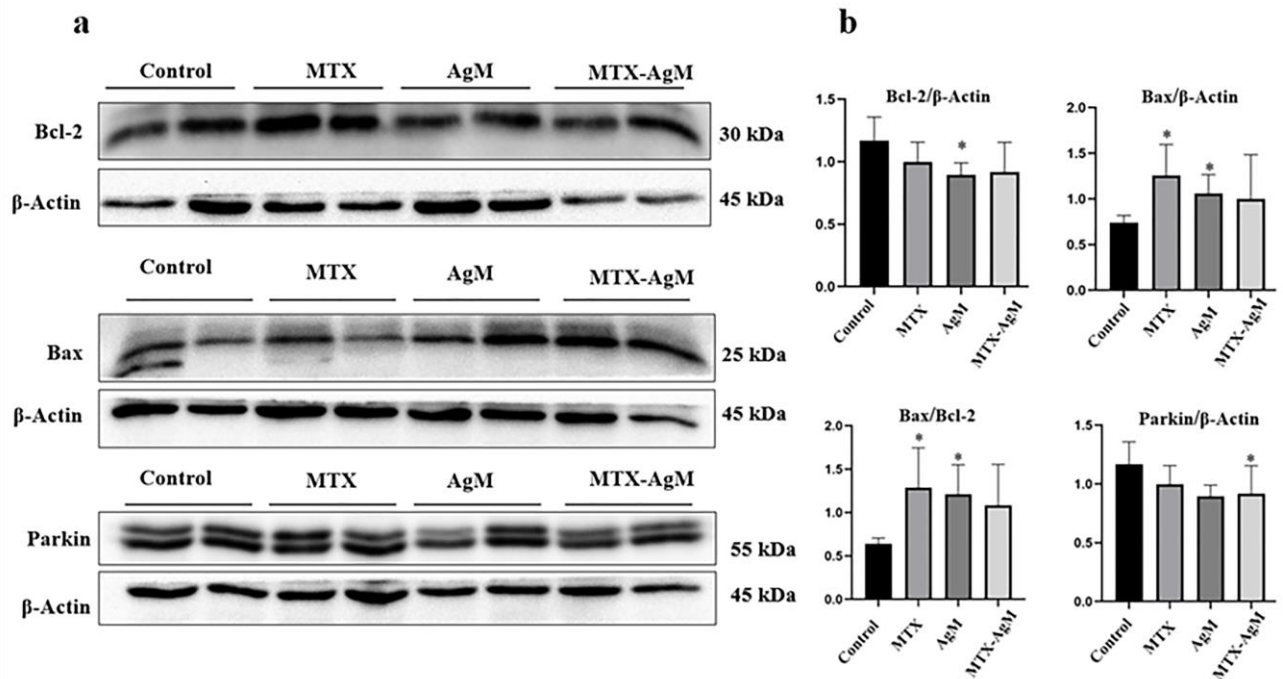
Figure 2. Results representing the alterations in protein expression levels. a) Representative Western blot images of anti-apoptotic Bcl-2, pro-apoptotic Bax, marker of mitophagy Parkin proteins and β-actin protein; b) the calculated protein band intensity results of the expression levels Bcl-2, Bax and Parkin proteins compared to that of β-actin and the Bax/Bcl-2 expression ratio. The represented Western blot images for each protein investigated were cropped from different blots, where same exposure was used for visualization. The samples were derived from the same experiment and the blots were processed in parallel. The data were represented as mean ± standard error of mean. Differences in between variances were compared by One-way ANOVA test with Tukey's test applied as a post-hoc test. A p value equal to or less than 0.05 was accepted as statistically significant (*p<0.05, **p<0.01, ***p<0.001). The degree of significance was indicated by an asterisk (*) for comparisons of all groups with respect to the control (C) group; by a dagger (†) for comparisons with respect to the MTX administered group.

Moreover, Bax/β-actin protein expression levels were observed to be significantly increased (p<0.05) in MTX and only AgM administration groups compared to the control. As Bax is involved in the pro-apoptotic pathway and its levels indicates the degree of apoptotic pathway activation, the observed increase in Bax expression may suggest that the dose and duration of MTX treatment used in this study was able to initiate the activation of the apoptotic pathway. The same effect is also seen in the AgM-only group (p<0.05). However, AgM treatment following MTX administration (MTX-AgM) only led to a slight decrease Bax protein expression levels. Similarly, Bax/Bcl-2 expression ratio was significantly increased in the MTX and AgM groups, while the Bax/Bcl-2 expression ratio was slightly decreased in the MTX-AgM group. When this ratio is evaluated, it may be suggested that MTX administration activates apoptosis and that AgM treatment following MTX administration might be effective in reducing the induced apoptosis. MTX administration resulted in a slight decrease in Parkin/β-actin expression levels, whereas AgM treatment following MTX

administration (MTX-AgM) led to a statistically significant decrease (p<0.05) in Parkin/β-actin expression compared to the control.

Histological analysis

Figure 4 demonstrates the representative images of luxol fast blue (LFB) (Figure 4a-4d), Masson's trichrome (MTC) (Figure 4e-4h) and hematoxylin-eosin (H&E) (Figure 4i-4l) histochemically stained, and GFAP immunohistochemically stained (Figure 4m-4p) sciatic nerve sections.
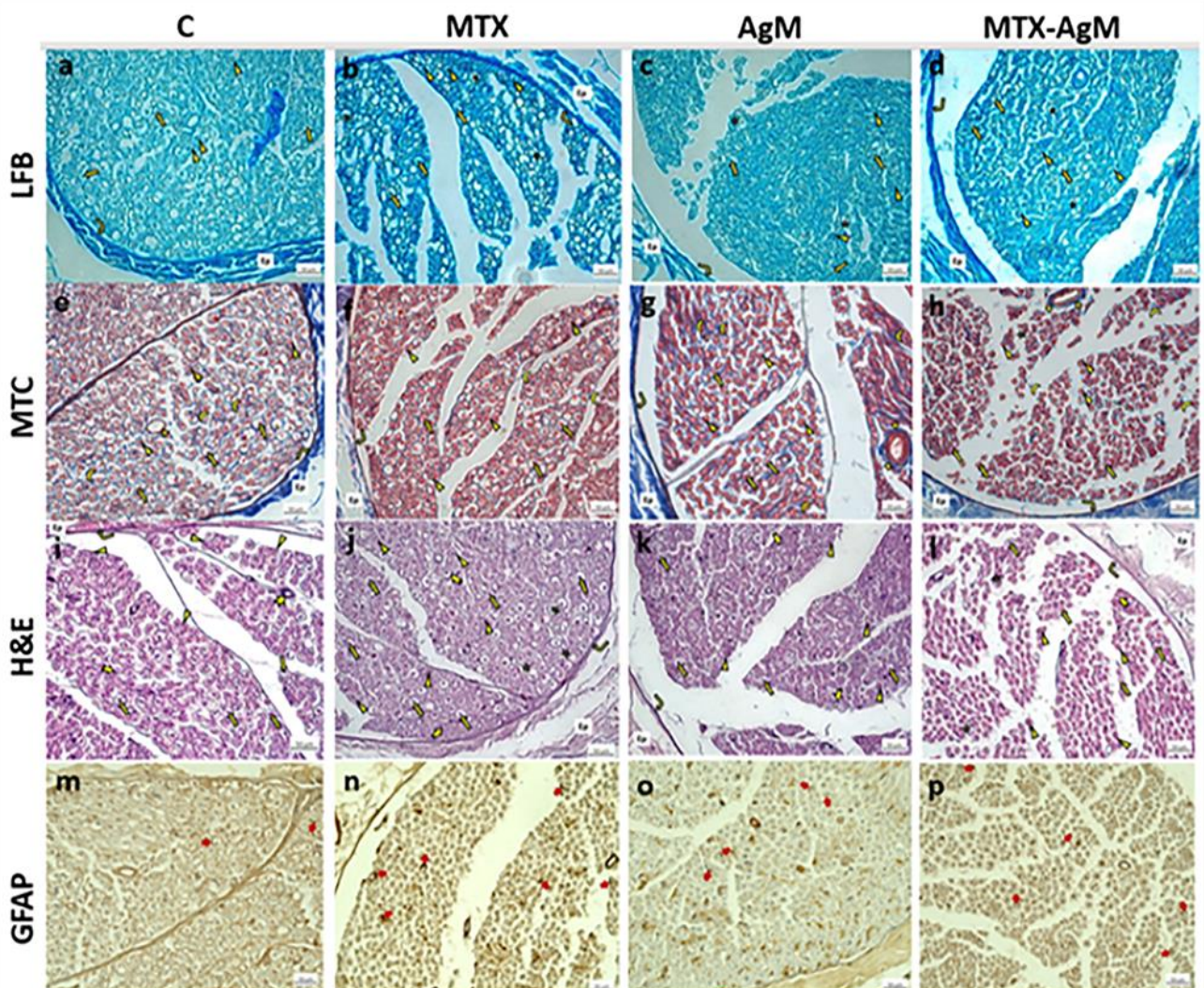

Figure 3. Representative images of the results of Luxol fast blue (LFB) (a, b, c, d), Masson's trichrome (MTC) (e, f, g, h), Hematoxylin–eosin (H&E) (i, j, k, l) and GFAP (m, n, o, p) stained sciatic nerve tissue sections belonging to the experimental groups. Notable features are indicated on the figure as follows: In the LFB staining, the following were identified: Epineurium (Ep), Perineurium (⟳), Axon (⬆), Myelin (△), Axonal Swelling (★); In the MTC staining, the following were identified: Epineurium (Ep), Perineurium (⟳), Axon (⬆), Myelin (△), Blood Vessels (⬠), Collagen Fibers (≫). In the H&E staining, the following were identified: Epineurium (Ep), Perineurium (⟳), Axon (⬆), Myelin (△), Blood Vessels (⬆), Schwann Cells (⬆), Axonal Swelling (★). In the GFAP immunostaining, the following were identified: GFAP positive schwann cells (➡). Magnification: 40X, Scale bar: 50 μm.

LFB staining enables the visualization of myelin and myelinated axons in nerve sections. Hematoxylin-eosin staining was used to visualize the general morphological structure of the sciatic nerve tissue and to distinguish between the nucleus and cytoplasm. Masson trichrome staining was used to visualize the structure of the connective tissue surrounding the nerve tissue as a sheath; and immunohistochemical staining with GFAP primary antibody was used to visualize the immunoreactivity of glial cells in the sciatic nerve tissue. Using the ImageJ-Win64 program, measurements of myelin sheath thickness, axon diameter and myelinated fiber diameter from LFB stained sections, and scoring of GFAP immunoreactivity in sciatic nerve Schwann cells were performed (Figure 5). According to the data obtained from histopathological analyses of the sciatic nerve, MTX treatment was found to decrease myelin thickness, axon and myelinated fiber diameter ($p<0.001$). Instead, AgM treatment following MTX administration was observed to increase axon diameter, myelin sheath thickness ($p<0.001$), and myelinated nerve fiber diameter ($p<0.05$) compared to the MTX group. In addition, the significant rise in the number of GFAP-positive Schwann cells ($p<0.001$) in the MTX group indicates nerve degeneration. AgM treatment following MTX administration (MTX-AgM) was found to reduce GFAP immunoreactivity compared to the MTX group ($p<0.001$). Interestingly, in the group with only AgM treatment, an increase in GFAP immunoreactivity was observed compared to the control group ($p<0.01$). Still, the reduction of GFAP immunoreactivity upon AgM treatment following MTX administration suggests the potential of AgM in the recovery from MTX-induced neurodegeneration (Figure 5).
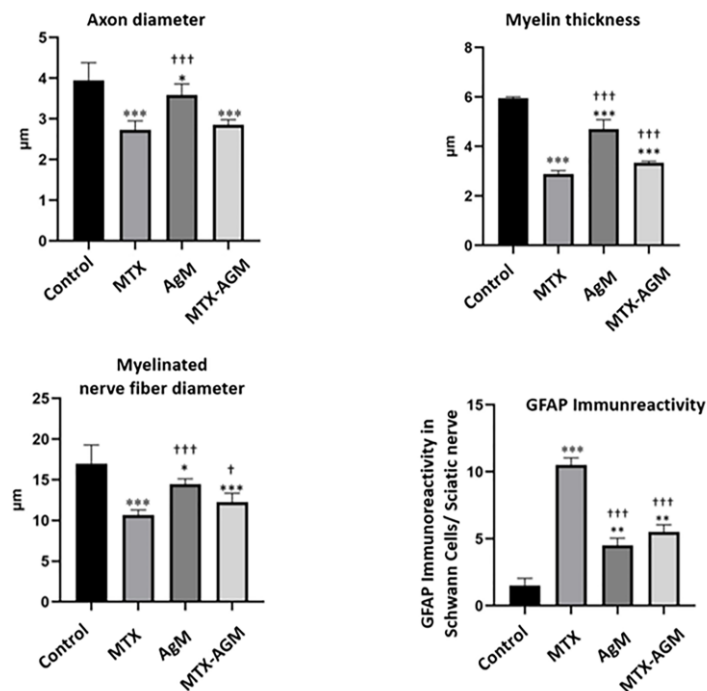

Figure 4. The results of the alterations in axon diameter, myelin sheath thickness, myelin fiber diameter, and GFAP positive immunoreactivity in Schwann cells in the experimental study groups. The data were represented as mean ± standard error of the mean. Differences in between variances were compared by One-way ANOVA test with Tukey's test applied as a post-hoc test. A p value equal to or less than 0.05 was accepted as statistically significant (*$p<0.05$, **$p<0.01$, ***$p<0.001$). The degree of significance was indicated by an asterisk (*) for comparisons of all groups with respect to the control (C) group; by a dagger (†) for comparisons with respect to the MTX administered group.

DISCUSSION

This study was conducted to evaluate the therapeutic potential of AgM in a MTX-induced peripheral neuropathy rat model. MTX, a chemotherapeutic agent, is being extensively utilized in the treatment of solid tumors and cancers observed in the nervous system at high acute doses, as well as in the treatment of some chronic autoimmune inflammatory diseases, for instance rheumatoid arthritis, at chronic low doses (15). The extensive utilization of MTX in the treatment of various diseases brings with it a wide range of side effects, for instance progressive hepatotoxicity and nephrotoxicity, cognitive impairments, peripheral neuropathy, varying degrees of axonopathy, and myelin damage, which also limits its use in therapy (16). Peripheral neuropathy, one of the frequent side effects of chemotherapeutic agents, significantly reduces the life quality of patients. As the dose and duration of the administered chemotherapeutic agent increase, the severity of the resulting neuropathy can vary.

AgM, an endogenous neuropeptide, is a well-known precursor polyamine in the synthesis of polyamines in plants and bacteria (17). AgM, which is known to possess a regulatory role in the nervous system, has a broad pharmacological effect spectrum, including anti-nociceptive and neuroprotective properties. It has been suggested that AgM could be a candidate for new therapeutic targets through better understanding of the underlying molecular mechanisms in relevant physiological and pathological processes (18). and has been used in numerous studies. However, this study is first to report the efficacy of AgM on MTX-induced peripheral neuropathy.

AgM was reported to produce antihyperalgesic and anti-allodynic outcomes in animal models of chronic neuropathic and inflammatory pain (19). In a rat model of neuropathy induced by intravenous cisplatin injection, a single dose of 100 mg/kg AgM was reported to not to lead to a significant effect on tail flick latencies whereas resulted in an improvement of nerve conduction velocities (20). In light of this information, it can be concluded that AgM provides effective treatment in nerve injuries, while the anti-nociceptive effect of AgM occurs only under chronic neuropathic conditions. Consistent with the findings in literature, in our study AgM treatment demonstrated a greater anti-nociceptive effect following MTX-administration, increased nerve conduction velocity, and AgM administration alone to healthy rats was found to have a lower allodynia perception. Future studies should further explore whether AgM induces degenerative changes in healthy subjects or shows therapeutic efficacy only in response to a damage mechanism. The results of this study demonstrated the effectiveness of a total 80 mg/kg AgM (i.p.) treatment in repairing nerve damage caused by MTX-induced neuropathy in rats, and our findings emphasize the importance of clarifying the mechanisms of action of AgM.

In addition, SFI was calculated to examine the effects of MTX and AgM administration on sciatic nerve function and to support the findings with electrophysiological results. MTX administration caused a decrease in SFI values, while AgM treatment following MTX administration resulted in an increase in SFI values, one

week after the cessation of AgM treatment. Additionally, AgM administration alone in healthy rats also caused a decrease in SFI values. Consistent with these findings, studies in the literature have shown that oral administration of 0.05 mg/kg MTX for 25 days in a rat rheumatoid arthritis model significantly decreased SFI values (20). The results of this study reveals that MTX administration at a dose of 37.5 mg/kg resulted in a significant reduction in sciatic nerve conduction and function, suggesting that MTX administration leads to peripheral nervous system degeneration. AgM treatment following MTX administration was observed to mitigate these adverse effects, leading to an improvement in sciatic nerve function and conduction.

One possible reason for the decreased nerve conduction and function is the loss of myelin sheath upon MTX administration. Histochemical staining of the sciatic nerve tissue with LFB revealed that MTX administration led to a significant reduction in axon diameter, myelin thickness, and the diameter of myelinated nerve fibers compared to the control group. The decrease in axon, myelin, and myelinated fiber diameters in the MTX group can be considered evidence of chemical neuropathy induced by MTX in the experimental animals. This reduction in axonal diameter in the MTX group explains the decrease in amplitude values in the electrophysiological measurement results of this study. Similarly, the reduction in myelin sheath thickness in the MTX group explains the slower nerve conduction velocity observed in the electrophysiological measurements of this study; additionally, the axonal and myelin damage in the MTX group supports the observed decline in nociceptive pain perception in this study. In addition, AgM treatment following MTX administration led to a slight increase in nerve conduction, together with a significant increase in myelin sheath thickness and myelinated fiber diameters. These findings are consistent with studies reporting that AgM application increases nerve conduction velocities and CMAP amplitudes. According to the GFAP immunohistochemical staining results in sciatic nerve tissue, an increase in GFAP expression was observed in the MTX group compared to the control group and compared to the AgM and MTX-AgM groups. This significant increase in GFAP expression in the MTX group is known to originate from Schwann glial cells in the peripheral nervous system (PSS), which become reactive as a result of systemic damage (21). GFAP expression was also increased in the only AgM administered group compared to the control group. However, the reduction in GFAP expression in the MTX-AgM group compared to the MTX group suggests that AgM application has a regenerative effect on MTX-induced nerve damage in the sciatic nerve, bringing it closer to the control group. The significant increase in GFAP expression in the AgM group compared to the control group and the significant decrease in the MTX-AgM group suggest that AgM may substantially improve the damage mechanism and may not show the same efficacy when administered to healthy rats, similar to the findings of others (22).

We have also examined some protein expression levels associated with apoptotic/anti-apoptotic and mitophagy mechanisms to explain how AgM demonstrates its effectiveness in reversing myelin damage and functional loss caused by MTX. The regulation of apoptosis mechanisms is managed by the Bcl-2/Bax gene family. The removal of damaged mitochondria through a process called mitophagy, which was reported to be

facilitated through PINK1 and Parkin related pathways, is critical for maintaining proper cellular function. Downregulation of the mitophagy leads to increased toxicity and ultimately neuronal death. Therefore, the regulation of both apoptotic and mitophagy pathways plays a crucial role in controlling neuronal dysfunction. According to our findings, MTX administration activated the pro-apoptotic pathway, resulting in an increase in Bax expression and a non-significant decrease in anti-apoptotic Bcl2 expression, together with a significant increase in Bax/Bcl-2 ratio. The increase in Bax expression may indicate that the MTX treatment dose and duration have triggered the activation of the apoptotic pathway. In the MTX-AgM group, however, AgM treatment was found to slightly reduce Bax protein expression levels and the Bax/Bcl-2 ratio. In the literature, AgM was reported to reduce the increased Bax protein expression induced by 15 μM cisplatin addition in the HEI-OC1 cell line, where only 8mM AgM addition onto HEI-OC1 cell line also resulted in a slight increase in the proportion of late apoptotic cells (23). Similarly, in the current study, AgM administration to healthy rats also resulted in an increase in the Bax/β-actin protein expression levels and Bax/Bcl-2 expression ratio and decreased Bcl-2 expression compared to the control group, suggesting that AgM alone might trigger the apoptotic pathway in healthy subjects, which should be explored in future studies. The Bax/Bcl-2 expression ratio is considered an important factor in determining the degree of apoptotic activation in the literature (24,25). Based on this ratio, it can be suggested that MTX treatment may have activated apoptosis, and AgM administered following MTX may be effective in reducing the induced apoptosis. Regarding Parkin protein expression levels, MTX administration led to a non-significant decrease compared to the control group, and the MTX-AgM treatment did not alter this situation but caused a statistically significant decrease compared to the control group. The Bax/Bcl-2 ratio showed a significant increase in both MTX and AgM groups, while Parkin levels exhibited a non-significant decrease compared to the control group. This finding indicates that the 37.5 mg/kg dose of MTX used in the experiment may tend to suppress the mitophagy pathway and that the administered dose of AgM may not be sufficient to reverse this effect. These results should be validated by future studies, and the effects of different doses of MTX or AgM should be investigated.

In literature, the administration of a combination of MTX (5 mg/kg) with other chemotherapeutic agents to a breast cancer mouse model was observed to prolong the escape latency to the platform in the water maze test but did not create a significant difference in the total number of squares traveled in the open field test (26,27). In another study, the combined administration of cyclophosphamide (40 mg/kg) and MTX (37.5 mg/kg) did not affect the fall latencies in the rotarod balance test (2). Our data indicate that MTX administration adversely affects the rats' memory and learning abilities, does not create a significant difference in grooming and rearing frequency, but causes a decrease in the total number of squares traveled, indicating a negative impact on locomotor activity. In this context, similar to findings in the literature, it can be said that the 37.5 mg/kg MTX used in our study induces nerve degeneration in the subjects. However, AgM treatment following MTX administration demonstrated a positive effect on learning and memory abilities and increased locomotor

activity. Additionally, the positive effect of AgM on cognitive abilities in behavioral tests is noteworthy and warrants future investigations.

AgM is a polyamine that is highly conserved in nature being found in bacteria, plants, invertebrates and vertebrates. It is present endogenously in brain and various organs of the body, such as the stomach, intestine, aorta and spleen, and generally found in a heterogeneous distribution throughout the tissues (28). Therefore; in experimental studies, the observed outcomes may vary depending on the organ studied and the dose of exogenous AgM used, where short and long-term administration of exogenous AgM is generally regarded as safe and non-toxic (29). Apart from its role to play in the excretion of Na+ ions, insulin and glucose metabolism in the periphery, AgM has been reported to be involved in a number of neurobiological processes exhibiting antinociceptive, anticonvulsant and antidepressant activity and is especially important in central neurotransmission (30). However; mechanistic studies have been focused on the effects of AgM through its NMDA antagonism, NOS inhibition and imidazoline or α2-adrenergic receptor interactions (28) and any other potential receptors or pathways of AgM action is yet to be resolved. AgM was reported to exert no significant alterations in locomotion, behavior and motor performance in naïve animals (28, 31), as supported by the findings of this study, where AgM administration to healthy rats did not result in a significant alteration in nociceptive latencies, locomotor activity and behavior of the rats. On the contrary, AgM administration following MTX resulted in an improvement in nociceptive latencies, locomotor activity and behavior of the rats. However, to the best of our knowledge, this study is the first to report the AgM related alterations in sciatic functional index, sciatic motor conduction and histopathological alterations, such as myelin thickness, axon and myelinated fiber diameter or GFAP immunoreactivity. Our results indicated that AgM administration following MTX improved MTX-induced alterations in SFI and increased myelin thickness and myelinated fiber diameter and decreased GFAP immunoreactivity. However, AgM administration to healthy rats resulted in a significant decrease in SFI, myelin thickness, axon and myelinated fiber diameter together with an increase in GFAP immunoreactivity. This discrepancy needs to be confirmed together with the elucidation of other possible targets of action of AgM in future studies and the outcomes of different doses of AgM or MTX administration should also be explored.

CONCLUSION

MTX induces neuropathy in rats, as indicated by the evidence of axonal damage associated with a reduction in axon diameter and a decrease in amplitude of CMAPs, myelin damage linked to a reduction in myelin sheath thickness and a decrease in nerve conduction velocity; an increase in apoptotic pathway activation and a decrease in the activation of the pathway for the elimination of damaged mitochondria, increased reactivity in glial cells, delayed responses to thermal stimuli, deterioration in learning and memory abilities, decreased locomotor activity, and a reduction in sciatic functional index values. Additionally, AgM

treatment following MTX administration has the potential to ameliorate the damage caused by MTX in sciatic nerves. However, AgM administration to naive rats showed a similar damage profile to the MTX-induced damage in some of the parameters studied compared to the control group, suggesting that AgM may has a therapeutic potential for ameliorating damage in existing degenerative conditions. The mechanisms and pathways underlying this property of AgM should be examined in more detail in future studies. Since this study used a single dose of AgM and MTX, the data obtained are somewhat limited, and different dosage studies should be conducted. This study only focused on the expression levels of one apoptotic/anti-apoptotic and mitophagy pathways, and the sample size of the study was rather small to point out the molecular mechanisms of AgM and MTX. Future studies should be conducted to confirm the mechanism of action of the drugs with larger sample sizes and explore protein expression levels in other pathways to better elucidate the mechanism of action. Additionally, the link between AgM treatment as well as MTX administration with inflammation should be assessed in detail in future studies**.**

Authorship contributions

Conception – HFY, OBG; Design – HFY, OBG; Supervision – OBG; Surgical and Medical Practices – HFY; Data collection and/or processing – HFY; Analysis and/or interpretation – HFY, OBG; Literature search – HFY, OBG; Writing – HFY, OBG; Critical review – OBG. All authors have read and approved the final version of the manuscript.

Data availibity statement

The datasets generated in the current study are available from the corresponding author on request.

Declaration of competing interest

The authors declare no competing interests.

Ethics

The Adnan Menderes University Experimental Animal Ethics Committee granted approval for this study (approval number: 64583101/2020/074).

Funding

This study was supported by Aydın Adnan Menderes University Scientific Research Projects Coordinatorship through the grant number TPF-21004.

REFERENCES

1. Zhao R, Diop-Bove N, Visentin M, Goldman ID. Mechanisms of membrane transport of folates into cells and across epithelia. Annu Rev Nutr. 2011; 31:177-201.

2. Kerckhove N, Collin A, Condé S, Chaleteix C, Pezet D, Balayssac D. Long-Term Effects, Pathophysiological Mechanisms, and Risk Factors of Chemotherapy-Induced Peripheral Neuropathies: A Comprehensive Literature Review. Front Pharmacol. 2022; 13:828387. doi: 10.3389/fphar.2022.828387.

3. Was H, Borkowska A, Bagues A, Tu L, Liu JYH, Lu Z, Rudd JA, Nurgali K, Abalo R. Mechanisms of Chemotherapy-Induced Neurotoxicity. Front Pharmacol. 2022; 13:750507. doi: 10.3389/fphar.2022.750507.

4. Raasch W, Schäfer U, Chun J, Dominiak P. Biological significance of agmatine, an endogenous ligand at imidazoline binding sites. Br J Pharmacol. 2001; 133(6):755-80.

5. Donertas B, Cengelli Unel C, Aydin S, Ulupinar E, Ozatik O, Kaygisiz B, et al. Agmatine co-treatment attenuates allodynia and structural abnormalities in cisplatin-induced neuropathy in rats. Fundam Clin Pharmacol. 2018; 32(3):288-296.

6. Sezer A, Güçlü B, Kazancı B, Çakır M, Coban MK. Neuroprotective effects of agmatine in experimental peripheral nerve injury in rats: a prospective randomized and placebo-controlled trial. J Surg Res. 2014; 187(1):227-234.

7. Fairbanks CA, Schreiber KL, Brewer KL, et al. Agmatine reverses pain induced by inflammation, neuropathy, and spinal cord injury. Proc Natl Acad Sci U S A. 2000; 97(19):10584-9.

8. Winocur G, Vardy J, Binns MA, Kerr L, Tannock I. The effects of the anti-cancer drugs, methotrexate and 5-fluorouracil, on cognitive function in mice. Pharmacol Biochem Behav. 2006; 85(1):66-75.

9. Sirvanci-Yalabik M, Sehirli AO, Utkan T, Aricioglu F. Agmatine, a metabolite of arginine, improves learning and memory in streptozotocin-induced Alzheimer's disease model in rats. Klin Psikofarmakol Bul. 2016; 26(4):342-354.

10. Varejão AS, Meek MF, Ferreira AJ, Patrício JA, Cabrita AM. Functional evaluation of peripheral nerve regeneration in the rat: walking track analysis. J Neurosci Methods. 2001; 108(1):1-9.

11. Jahromi Z, Mohammadghasemi F, Moharrami Kasmaie F, Zaminy A. Cinnamaldehyde enhanced functional recovery after sciatic nerve crush injury in rats. Cells Tissues Organs. 2020; 209(1):43-53.

12. Li XM, Su F, Ji MH, Zhang GF, Qiu LL, Jia M, et al. Disruption of hippocampal neuregulin 1–ErbB4 signaling contributes to the hippocampus-dependent cognitive impairment induced by isoflurane in aged mice. Anesthesiology. 2014; 121(1):79-88.

13. Mizoguchi K, Yuzurihara M, Ishige A, Sasaki H, Tabira T. Chronic stress impairs rotarod performance in rats: implications for depressive state. Pharmacol Biochem Behav. 2002; 71(1-2):79-84.

14. Sharma S, Rakoczy S, Brown-Borg H. Assessment of spatial memory in mice. Life Sci. 2010; 87(17-18):521-536.

15. Pivovarov K, Zipursky JS. Low-dose methotrexate toxicity. CMAJ. 2019; 191(15): E423. doi: 10.1503/cmaj.181054.

16. Rollins N, Winick N, Bash R, Booth T. Acute methotrexate neurotoxicity: findings on diffusion-weighted imaging and correlation with clinical outcome. AJNR Am J Neuroradiol. 2004; 25(10):1688-1695.

17. Gilad GM, Salame K, Rabey JM, Gilad VH. Agmatine treatment is neuroprotective in rodent brain injury models. Life Sci. 1995; 58(2): PL 41-6. doi: 10.1016/0024-3205(95)02274-0.

18. Gümrü S, Şahin C, Arıcıoğlu F. Yeni bir nörotransmitter/nöromodülatör olarak agmatine genel bir bakış. Clin Exp Health Sci. 2014; 3(5), doi.org/10.5455/musbed.20130412103633.

19. Yeşilyurt Ö, Uzbay IT. Agmatine potentiates the analgesic effect of morphine by an α2-adrenoceptor-mediated mechanism in mice. Neuropsychopharmacology. 2001; 25(1):98-103.

20. Shahnaz M, Biswas P, Akhter M, Rafiq K, Ali T. Effects of Spirulina platensis on neuropathic pain in Wistar rats. J Bangladesh Soc Physiologist. 2021; 16(1):1-10.

21. Schmidt-Kastner R, Wietasch K, Weigel H, Eysel UT. Immunohistochemical staining for glial fibrillary acidic protein (GFAP) after deafferentation or ischemic infarction in rat visual system: features of reactive and damaged astrocytes. Int J Dev Neurosci. 1993; 11(2):157-174.

22. Peterson CD. Alleviation of chronic neuropathic pain by agmatine requires the GluN2B subunit of the NMDA receptor [dissertation]. Minneapolis (MN): University of Minnesota; 2017.

23. Park E, Lee SH, Jung HH, Im GJ. Protective effect of agmatine against cisplatin-induced cellular apoptosis in an auditory cell line. J Int Adv Otol. 2022; 18(3):257.

24. Ouyang YB, Giffard RG. Cellular neuroprotective mechanisms in cerebral ischemia: Bcl-2 family proteins and protection of mitochondrial function. Cell Calcium. 2004; 36(3-4):303-311.

25. Wei L, Cui L, Snider BJ, Rivkin M, Steven SY, Lee CS, et al. Transplantation of embryonic stem cells overexpressing Bcl-2 promotes functional recovery after transient cerebral ischemia. Neurobiol Dis. 2005; 19(1-2):183-193.

26. John J, Kinra M, Ranadive N, Keni R, Nayak PG, Jagdale RN, et al. Neuroprotective effect of Mulmina Mango against chemotherapy-induced cognitive decline in mouse model of mammary carcinoma. Sci Rep. 2022; 12(1):3072. doi: 10.1038/s41598-022-06862-9.

27. Iarkov A, Appunn D, Echeverria V. Post-treatment with cotinine improved memory and decreased depressive-like behavior after chemotherapy in rats. Cancer Chemother Pharmacol. 2016; 78:1033-1039.

28. Uzbay TI. The pharmacological importance of agmatine in the brain. Neurosci Biobehav Rev. 2012; 36(1):502-519.

29. Gilad GM, Gilad VH. Long-term (5 years), high daily dosage of dietary agmatine—evidence of safety: a case report. J Med Food. 2014; 17(11):1256-1259.

30. Reis DJ, Regunathan S. Is agmatine a novel neurotransmitter in brain?. Trends Pharmacol Sci. 2000; 21(5):187-193.

31. Dhokne MD, Dixit MP, Kale MB, Aglawe MM, Umekar MJ, Taksande BG. Agmatine as a novel treatment option for neuropathies: experimental evidences. INNOSC Theranostics Pharmacol Sci. 2023; 5(2):1-10.